Hf, W and Zr nucleosynthetic inventory of chondrites

Inaugural-Dissertation
zur
Erlangung des Doktorgrades
der Mathematisch-Naturwissenschaftlichen Fakultät
der Universität zu Köln

vorgelegt von

Bo-Magnus Elfers

aus Steinfurt

Köln, 2016

Gutachter:	Prof. Dr. Carsten Münker
	Dr. Dominik Hezel
Tag der mündlichen Prüfung:	20.01.2017

Keep your eyes on the stars, and your feet on the ground.

Theodore Roosevelt

CONTENTS

Abstract

Key questions in cosmochemistry are: How was the solar system formed, what was its initial state and composition, what were its initial components and which processes forged its present state. The solar system formed about 4.57×10^9 years ago (i.e., 4.57 Ga) from a gravitationally collapsing molecular cloud. Conserving angular momentum, the infalling cloud material formed a circumstellar disk, the solar nebula, from which most of the Sun's mass accreted within a few hundred thousand years. In these early stages the young Sun is very active. Bipolar jets stream from the poles and rapid accretion events lead to radiation outbursts. However, with time the infall of cloud material onto the disk ceases and eventually stopped. Most of the dust and gas left in the disk after the infall ceased also accreted onto the Sun or was blown out by stellar radiation. Some of this disk material however accreted to form small bodies and later even planets. The most primitive, i.e. unprocessed, fraction of these bodies are referred to as chondrite parent bodies. Chondrites, which are meteorite samples of such bodies, are essentially space sediments composed of mechanical mixtures of materials with different origins. The chondrite parent bodies formed by accretion of solid particles within the young solar nebula. They are very old (>4.5 Ga) and formed at the beginning of the solar system. Chondrites sample unmelted and in the case of primitive specimen even only weakly metamorphosed regions of their parent bodies, and thus the components of the latter mostly sustained their pristine isotopic compositions. As consequence, chondrites can be seen as time capsules from the early solar system that sometimes even provide insights into processes which took place before the solar system formed. A very simple method to look at the isotopic fingerprints of the different components of chondrites is to sequentially leach them with acids of increasing strength until full samples dissolution is achieved. Sequential leaching separates different components of chondrites according to their acid resistances. Likewise, presolar grains which are present in the most primitive chondrites were first identified. Presolar grains are referred to as “presolar” because their formation predates that of the solar system. Such grains were identified via their isotope signatures, which differ significantly from that of solar system material. Presolar grains usually preserve the nucleosynthetic isotope fingerprint of their parent stars and thus provide direct information about the nucleosynthetic processes that took place within their parent stars. Thus, presolar grains provide the means to investigate stellar nuclide production in the laboratory.

All elements heavier than H and He are thought to be dominantly produced by stars other than the sun, because as a small main sequence star, the sun is only fusing H to He. Thus, elements heavier than He present in the solar system must have been inherited from the interstellar matter from which the sun and the solar nebula was formed. Elements lighter than iron are produced via nuclear fusion reactions, whereas elements heavier than iron are predominantly produced by neutron capture reactions on pre-existing "seed" nuclei. There are at last three environments in which such neutron capture reactions take place: asymptotic giant branch (AGB) stars, core collapse supernovae and neutron star merger. In an asymptotic giant branch star, only nuclides along the realm of stable nuclides on the chart of nuclides (i.e., the "valley of stability") are produced because the neutron capture rate is low relative to the decay rate of unstable nuclides. This is referred to as the s-process (slow neutron capture process). In contrast, neutron densities during core collapse supernovae or neutron merger are much higher, allowing capture of neutrons by unstable nuclides at rates that are high relative to their decay rate. This is referred to as the r-process (rapid neutron capture process). Proton-rich or neutron poor "p-process" isotopes, in contrast, are not produced by the s- or r-process. These nuclides are thought to be produced by a complex chain of reactions including proton capture, neutron capture, and photodisintegration, possibly at similar stellar sites as the r-process.

Here, isotopic traces of the different stellar environments in which the material of our solar system had formed are investigated. The focus in **chapter II** is on trying to address observed nucleosynthetic Hf and W isotope variations between leachates and residues of eight different meteorites to variations in the abundance of s,- r-, or p-process Hf and W. To do so, a three step leaching protocol was developed for chondritic meteorites. This protocol was sufficiently selective to yield distinctive isotope anomalies that identified the observed Hf and W isotope variations to be caused by variable distributions of s-process carrier phases. However, since only three leaching steps were performed, potential r- and/or p-process variations may have escaped detection. Moreover, due to an insufficiently selective mineral dissolution during the leaching steps, constraining the nature of nucleosynthetic s-process carrier phases was made difficult. Mass balance calculations indicate that the main s-process W carrier is mainstream SiC. In contrast to that, s-process Hf seems to be carried dominantly by other phases, potentially presolar silicates or oxides. In addition, the comparison of the different magnitudes of the Hf and W isotope variations between the different leachates of the different meteorites revealed that the main s-process W carrier was selectively destroyed in

especially Kainsaz and Allende. This selective destruction was most likely implemented either within the solar nebula, on parent body or in both environments likely by oxidation processes.

The focus of **chapter III** lies on investigating, as to whether r- or p-process variations are resolvable using an improved and more selective procedure and in identifying the carrier phases of the different nucleosynthetic components. To achieve this goal, a five step leaching scheme was now developed and applied to the chondrites Murchison, Kainsaz and Allende. These three meteorites yielded the most significant Hf and W isotope variations in leach fractions of **chapter II**. In addition, concentrations of elements in addition to Hf and W, including Mg, Al, Ca, Ti, Cr, Fe, Co, Ni, and Zr were analyzed in the different leach fractions. The results indicate that, although more leaching steps were performed, still no resolvable r- and/or p-process variations could be detected, further supporting the model that all observed Hf and W isotope variations are solely caused by s-process components. Moreover, based on the element concentration data, oxide minerals could be identified as the most likely s-process Hf carrier phases. In contrast, mass balance calculations identify mainstream SiC as the main s-process carrier phase for W. The comparison of the magnitudes of the Hf and W isotope varaitions between the different leachates and residues of Murchison, Kainsaz and Allende, supports the observations of **chapter II** that SiC was selectively destroyed in CV and CO chondrites. Both, the homogenization of r-and p-process phases as wells as the selective SiC destruction happened either within the solar nebula prior to parent body accretion or on the parent body itself and was likely accompanied by oxidation processes.

Chapter IV focuses on the Zr isotope signatures of the leachates and residues examined in chapter III. Similar to Hf and W, Zr can also be produced by slow and rapid neutron captures processes. However, in contrast to Hf and W, significant isotope anomalies were detected at the bulk rock scale for Zr in previous studies, whereas none were found for Hf and W. This observation indicates that not all Zr, Hf, and W carrier phases can be identical and that some synthesis of s- and/or r-process Zr may have happened separate from that of Hf and W. To closer evaluate the nucleosynthetic decoupling of Zr from Hf (and W) the same leachates as in **chapter III** were investigated with respect to their Zr isotope inventories. Results show that there are significant Zr isotope variations among the different leachates and residues of Murchison, Kainsaz, and Allende. These Zr isotope variations correlate very well with the Hf isotope signatures but disagree with the astrophysical models that are used to constrain the origin of the Hf and W isotope variations among leachates and residues of

Murchison, Kainsaz, and Allende in **chapter II** and **III.** However, newer models of s-process Zr nucleosynthesis in AGB stars that account more closely for the initial mass of the star provide a good fit between results for low-mass AGB stars and the leachate and residue Zr isotope data, and rule higher-mass AGB stars as the source of the presolar carriers out. This result is fully compatible with the observed Hf and W isotope patterns and thus uniquely identifies the stellar production environment of the last s-process material to be added to the proto-solar nebula. In contrast to Hf and W, bulk rock anomalies were observed for Zr. This difference may result from a nebula-wide heterogeneous distribution of a non-s-process enriched Zr phase that does not carry significant amounts of r-process Hf and W. At least part of this non-s-process Zr seems to reside in Calcium-Aluminum-rich inclusions (CAIs) which are the oldest solid objects that formed within the solar system.

Kurzzusammenfassung

Schlüsselfragen der Kosmochemie sind: Wie wurde das Sonnensystem gebildet, was war sein Urzustand und seine ursprüngliche Zusammensetzung und welche Prozesse trugen dazu bei, den heutigen Zustand des Sonnensystems zu erzeugen. Das Sonnensystem wurde vor ca. 4.57×10^9 Jahren (4.57 Ga) in Folge des gravitativen Kollapses einer Molekülwolke im Weltall gebildet. Hierbei bildete das einfallende Material unter Drehimpulserhaltung eine die Sonne umschließende Scheibe, den Solaren Nebel, von dem der überwiegende Teil die Sonne selbst innerhalb von wenigen hunderttausend Jahren akkretierte.

Während dieser Frühphase war die Sonne besonders aktiv. Hierbei sind vor allem bipolare Masseauswürfe an den Polen der Sonne, sowie massive Strahlungsausbrüche in Folge von gesteigerter Akkretion von Material auf die Sonne zu nennen. Im Laufe der Zeit nahm der Einfall von Material auf die Sonne immer mehr ab, um schließlich ganz zum Erliegen zu kommen. Der überwiegende Teil des verbliebenen Gases und Staubs wurde anschließend ebenfalls auf die Sonne akkretiert oder durch Strahlung weggeblasen. Ein kleiner Teil des verbliebenen Gases und Staubs konnte sich diesen Prozessen entziehen und ballte sich zu kleinen Körpern zusammen, die wiederum später Planeten bildeten. Die primitivsten, das heißt am wenigsten sekundär prozessierten dieser Körper, werden heute allgemein als Chondritmutterkörper bezeichnet. Chondrite, also Meteorite, die aus diesen Mutterkörpern stammen, können hierbei am besten mit Sedimentgestein vergleichen werden, da Chondrite im Wesentlichen eine mechanische Mischung von verschiedensten Komponenten des frühen Sonnensystems darstellen. Die Mutterkörper dieser Chondrite haben

sich dabei im Wesentlichen als Folge der Akkretion dieser Komponenten gebildet. Diese geschah bereits sehr früh, vor ca. 4.5×10^9 Jahren, im Sonnensystem. Die primitivsten Chondrite stellen dabei die Bereiche ihrer Mutterkörper dar, die ungeschmolzen und nur schwach metamorph überprägt wurden. Daher haben die Komponenten dieser Meteoriten im Wesentlichen ihre ursprüngliche Isotopensignatur noch erhalten. Somit können Chondrite als Zeitkapseln bezeichnet werden, die frühe Prozess im Sonnensystem und manchmal sogar aus der Zeit davor erschließen. Eine sehr einfache Methode sich die isotopischen Fingerabdrücke der verschiedenen Komponenten der Chondrite anzusehen, ist dabei, sie sequentiell mit Säuren zunehmender Stärke zu lösen. Das Prinzip der Komponentseparation basiert dabei auf den unterschiedlichen Säurebeständigkeiten der einzelnen Komponenten in Chondriten. So konnte mit Hilfe dieses Verfahrens zum Beispiel dargelegt werden, dass einige sehr primitive Chondrite nicht nur solares Material sondern auch „präsolares“ Material enthalten. Dieses Material zeichnet sich im Wesentlichen durch Isotopensignaturen aus, die sich sehr stark von denen unterscheiden, die die übrigen Materialien des Sonnensystems zeigen. Präsolare Körner sind hierbei von besonderem Interesse, da sie die Isotopensignatur ihres Muttersterns um den sie kondensierten wie ein Fingerabdruck speichern. Somit erlauben sie die Untersuchung von Nukleosynthese und stellaren Prozessen im Labor.

Generell gelten alle Elemente des Sonnensystems, deren Masse die von H and He überschreiten, als nicht von der Sonne gebildet, da die Sonne als kleiner Hauptsequenzstern lediglich H zu He fusioniert. Elemente deren Masse unterhalb der des Eisens liegt werden durch Kernverschmelzung gebildet, alle schwereren Elemente im Wesentlichen durch Neutroneneinfangsreaktionen durch bereits existierende Nuklide. Im Wesentlichen werden drei stellare Umgebungen unterschieden, an denen Elementsynthese durch Neutroneneinfangsprozesse abläuft: „asymptotic giant branch“ (AGB) Sterne, Kern-Kollaps Supernovae und die Kollision von Neutronensternen. In AGB Sternen ist die Neutroneneinfangrate dabei eher klein, sodass nur Nuklide gebildet werden, die dem sogenannten Tal der Stabilität in der Nuklidkarte folgen, das heißt, die Neutroneneinfangsrate ist gering im Vergleich zur Rate mit der instabile Nuklide zu stabileren zerfallen. Dieser Prozess wird auch als „slow neutron capture“ oder S-Prozess bezeichnet. Im Gegensatz dazu steht der R-Prozess für „rapid-neutron capture“. Dieser Prozess läuft im Wesentlichen bei höheren Neutronendichten ab während z.B. Kernkollaps Supernovae oder der Kollision von Neutronensternen. Hierbei sind die Neutronendichten so hoch, das auch instabile Nuklide Neutronen einfangen können bevor sie zerfallen. Weiterhin existieren sogenannte „P-Prozess“

Nuklide. Hierbei handelt es sich um Nuklide, die weder durch den S- noch durch den R-Prozess gebildet werden. Es wird angenommen, dass diese Nuklide infolge einer komplexen Kette von Protoneneinfangs- sowie Neutroneneinfangs und Photodisintegrationsreaktionen entstehen. Diese finden möglicherweise in denselben stellaren Umgebungen ab wie der R-Prozess.

In dieser Arbeit werden nun die Spuren der zuvor beschriebenen verschiedenen stellarer Produktionszweige näher beleuchtet. Der Fokus in **Kapitel II** liegt im Wesentlichen darauf, beobachteten nukleosynthetischen Hf und W Isotopenvariation zwischen den einzelnen sequentiell aufgelösten Mineralfraktionen dem S- R- und/oder P-Prozess zuzuschreiben. Hierfür wurde ein drei schrittiges Protokoll zum sequentiellen Auflösen von acht Meteoriten entwickelt. Dieses Protokoll erlaubte es die beobachteten Hf und W Isotopensignaturen eindeutig der Variation von S-Prozess angereicherten Phasen zuzuordnen. Da jedoch nur drei sequentielle Schritte vorgenommen wurden, könnte es erstens ggf. sein, dass vorhandene R-und/oder P-Prozess Variationen der Detektion entgangen sind und zweitens, war es so schwierig die genauen Träger der jeweiligen S-Prozess Variationen näher zu bestimmen. Massenbilanzrechnungen weisen darauf hin, dass es sich bei der initialen S-Prozess W Trägerphase um mainstream Siliziumkarbid (SiC) handelt, während S-Prozess Hf von einer oder mehreren anderen Trägerphasen getragen werden muss. Hierbei handelt es sich am wahrscheinlichsten um Silikate oder Oxide. Zusätzlich zeigt der Vergleich der Magnituden der Hf und W Isotopenvariationen der verschiedenen Leachate und Residuen, dass der S-Prozess W Träger vor allem in Kainsaz und Allende selektiv zerstört worden sein muss. Diese selektive Zerstörung wurde sehr wahrscheinlich im solaren Nebel, auf dem Mutterkörper oder im solaren Nebel und auf dem Mutterkörper in Folge von wahrscheinlich Oxidationsprozessen implementiert.

Der Fokus in **Kapitel III** liegt darauf in **Kapitel II** potentiell maskierte R- oder P-Prozess Anomalien aufzulösen und die Trägerphasen der verschiedenen nukleosynthetischen Prozesse besser zu bestimmen. Um dies zu erreichen wurde ein fünf schrittiges sequentielles Auflösungsverfahren entwickelt und an Murchison, Kainsaz und Allende angewendet. Diese drei Meteorite zeigten **in Kapitel II** dabei die größten Hf und W Isotopenvariationen und wurden daher als Proben ausgewählt. Zusätzlich wurden noch die Hf, W, Mg, Al, Ca, Ti, Cr, Fe, Co, Ni, und Zr Konzentrationen in den einzelnen Leachschritten gemessen um weitere Informationen über die einzelnen Phasen zu gewinnen, die in den verschiedenen Leachschritten gelöst werden. Die Resultate zeigen, dass obwohl mehr Leachschritte

unternommen wurden, keine R- oder P-Prozess Variationen aufgedeckt werden konnten. Die Isotopenvariationen die aufgedeckt wurden, konnten allein dem S-Prozess zugeordnet werden. Mit Hilfe der Elementkonzentrationsmessungen konnte zudem aufgedeckt werden, dass es sich bei den S-Prozess Hf Trägern am wahrscheinlichsten um Oxide handelt. Dagegen zeigen Massenbilanzen ähnlich wie in **Kapitel II**, dass die primäre S-Prozess W Phase mainstream SiC ist. Ähnlich zu den Beobachtungen aus **Kapitel II**, zeigt der Vergleich der Hf und W Isotopenvariationen zwischen den Leachaten und den Residuen von Murchison, Kainsaz und Allende, dass SiC in CV und CO selektiv zerstört worden ist. Beides, sowohl die Homogenisierung als auch die selektive Zerstörung des SiC geschah sehr wahrscheinlich im solaren Nebel bevor die einzelnen Mutterkörper sich bildeten oder auf dem Mutterkörper selbst, wahrscheinlich in Kombination mit Oxidationsprozessen.

Der Fokus in **Kapitel IV** liegt auf dem Zr Isotopenmessungen der Leachate und Residuen der Proben aus **Kapitel III**. Genau wie die Isotope von Hf und W werden auch die Isotope von Zr in Folge von Neutroneneinfangsreaktionen (S- und R-Prozess) gebildet. Interessanterweise und im Gegensatz zu Hf und W, konnten für Zr Isotope ebenfalls Gesamtgesteinsvariationen festgestellt werden. Diese Beobachtungen suggerieren, dass nicht alles Zr, Hf und W von denselben Trägern getragen werden kann und somit muss zumindest ein kleiner Teil der Zr Isotopensynthese in anderen stellaren Umgebungen geschehen sein, als die des Hf oder W. Um diese Entkopplung näher zu beleuchten, wurden dieselben Leachate und Residuen untersucht, welche bereits in **Kapitel III** auf ihre Hf und W Isotopensignaturen untersucht wurden. Die Ergebnisse zeigen, dass ebenfalls signifikante Zr Isotopenvariationen zwischen den einzelnen Leachaten und Residuen von Murchison, Kainsaz und Allende existieren. Diese Variationen korrelieren vor allem mit Hf Isotopenvariationen, aber korrelieren nicht mit denselben astrophysikalischen Modellen, die für die Synthese der Hf und W Isotope genutzt wurden. Neuere astrophysikalische Modelle für die Zr Isotopensysnthese, die stärkere Gewichtung auf die initialen Massen der verschiedenen AGB Sterne legen, zeigen dagegen, dass die beobachteten Zr Isotopenvariationen sehr gut mit der Variation einer Phase übereinstimmen, welche um einen niedrig massigen AGB Stern kondensiert ist. Diese Resultate stimmen gleichzeitig sehr gut mit den Beobachtungen für Hf und W Isotopenvariationen in den Leachaten und Residuen überein und identifizieren somit niedrig massige AGB Sterne eindeutig als eine Quelle, die Material zur Bildung des Sonnensystems beigetragen hat. Der Unterschied, dass für Zr Gesamtgesteinsvariationen zu beobachten sind und für Hf und W dagegen nicht, liegt wahrscheinlich an der heterogenen Verteilung eines

„nicht S-Prozess Zr“ Trägers im solaren Nebel welcher keine signifikanten Mengen an Hf und W trägt. Zumindest ein Teil dieses „nicht S-Prozess“ Zr wird dabei wahrscheinlich von CAIs getragen, welche die ältesten Objekte im Sonnensystem sind.

Chapter I

Introduction

I.1 Origin of elements:

The universe formed ca. 13.7 billion years ago by expansion from a hot and dense energy state (see Hawking, 1988 or Wienberg, 1993 for summaries of the main features) (Seife, 2003) (Ga). This event, referred to as big bang also involved production of first stable nuclides (Alpher, Bethe and Gamow, 1948). This process is called primordial nucleosynthesis and mainly led to the production of H (~75%) and He (~25%), and traces of Li. However, after the universe continued expanding and cooling, nuclide abundances became frozen and no more fusion reactions took place, thus elements heavier than He must have been produced by other processes. This claim was first made by Hoyle (1946; 1954) and first empirical evidence was given by Merril (1952). He showed that short lived ($\sim 4\times10^6$) Technetium (Tc) was present within the envelopes of some cool giant stars and concluded that Tc had been produced by these stars, and had evidently been transported to their surfaces. In 1957, Burbidge, Burbidge, Fowler, and Hoyle and Cameron provided the first comprehensive reviews on stellar nucleosynthesis. These studies recognized that elements not produced by the Big Bang were synthesized in tandem with the evolution of stars from birth to death. They showed that elements heavier than He but lighter than Fe are produced by the fusion reactions whereas elements heavier than Fe like Zr, Hf or W are produced via a complex interplay of neutron capture processes on lighter precursor nuclides and β^- decay reactions, where a neutron is converted to a proton, an electron and an antineutrino. Main fusion reactions are the fusion of Helium during Hydrogen burning, the fusion of three α-particles (^{4}He) to ^{12}C during Helium burning, the fusion of ^{12}C to excited ^{24}Mg during Carbon burning, the fusion of ^{20}Ne with ^{4}He to ^{24}Mg during Neon burning and the fusion of ^{16}O to excited ^{32}S during oxygen burning. The final fusion step occurs during the Silicon burning phase where ^{28}Si, the main product of the Neon burning stage, is beginning to fuse with lighter particles to form nuclides with higher masses up to iron. It should be noted that all the fusion reactions are exothermic, so that energy is released. However, at the end of the evolution of a massive star, the star can gain no energy anymore form fusion, because the nuclear fusion of elements heavier than Fe is an endothermic reaction. At this point, Fe in the core disintegrates into protons, neutrons, and α-particles by absorbing gamma rays, leading to the collapse of the stellar core. As a result of the core collapse, a shock is generated which blows away the outer layers of the stars, a so called supernova event.

In contrast to fusion, elements of higher mass than iron like Zr, Hf and W are produced via a complex interplay of neutron capture processes, β^- decay reactions (conversation of a neutron

to a proton, an electron and an antineutrino), proton capture and photodisintegration processes. The neutron capture can occur in two ways: slow neutron capture, the so called s-process or rapid neutron capture, the r-process. In first scenario, neutron capture reactions continue until an unstable nucleus is reached that β^-decays. This slow neutron capture process dominantly occurs in asymptotic giant branch stars, as a result of the neutrons release during the fusion of ^{13}C and ^{4}He and ^{22}Ne and ^{4}He. In contrast, the r-process mainly occurs during the neutron rich conditions of core collapse supernova of massive stars or the merger of two neutron stars. During these events neutron capture rates are sufficiently high, so that a neutron can be captured by an unstable nucleus before it decays, resulting in the production of even heavier nuclei. This process may continue until a nucleus is formed that decays faster than that neutron capture can occur. In a plot of atomic number versus number of neutrons, the s-process follows a zigzag type pathway to which nuclei produced by the r-process plot on the far right hand side, as illustrated by Figs. 1 a, b , c. However, as obvious from ^{174}Hf and ^{180}W (see fig. 1 b, c), some nuclides plot on the left-hand, neutron poor side, isolated from the s-process path, and, hence, cannot have formed via neutron capture reactions. These nuclides are called p-nuclides or proton rich nuclides. The nuclides were first interpreted to result from proton capture reaction with seed nuclei (Burbridge et al. 1957), however with ongoing research it became obvious that actual proton capture reaction only play a minor role in the synthesis of these nuclides (e.g., Arnould & Goriely, 2003; Rauscher et al., 2013). These workers pointed out that, the p-process nuclides are more likely synthesized by a chain of photodisintegration processes of heavier s- and r-process nuclei in explosive O/Ne-shell burning during a core-collapse supernova.

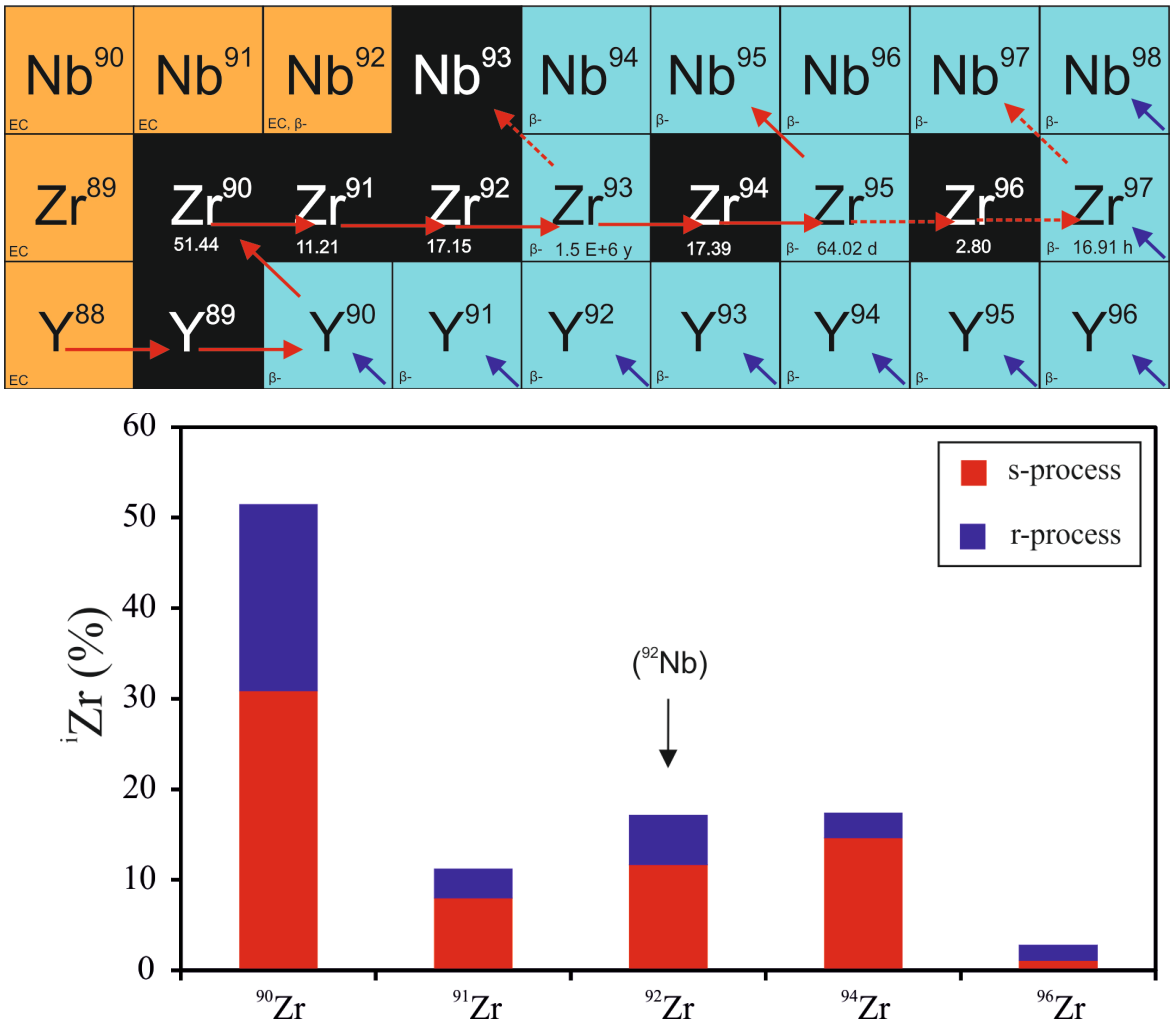

Fig. 1a: The Zr region of the chart of the nuclides (upper panel) and the nucleosynthetic contributions to the Zr isotope inventory (lower panel). Stable isotopes and their solar abundances are in black boxes, short-lived isotopes and their half-lives are in blue (β^- unstable) and orange (electron capture). The red arrows indicate the main path of s-process nucleosynthesis, dashed arrows minor branches. Blue arrows mark the decay path of nuclides produced during the r-process. ^{90,91,92,94,96}Zirconium are produced via s- and r-process. ^{92}Zirconium also gains contribution from ^{92}Nb decay (e.g., Münker et al. 2000)

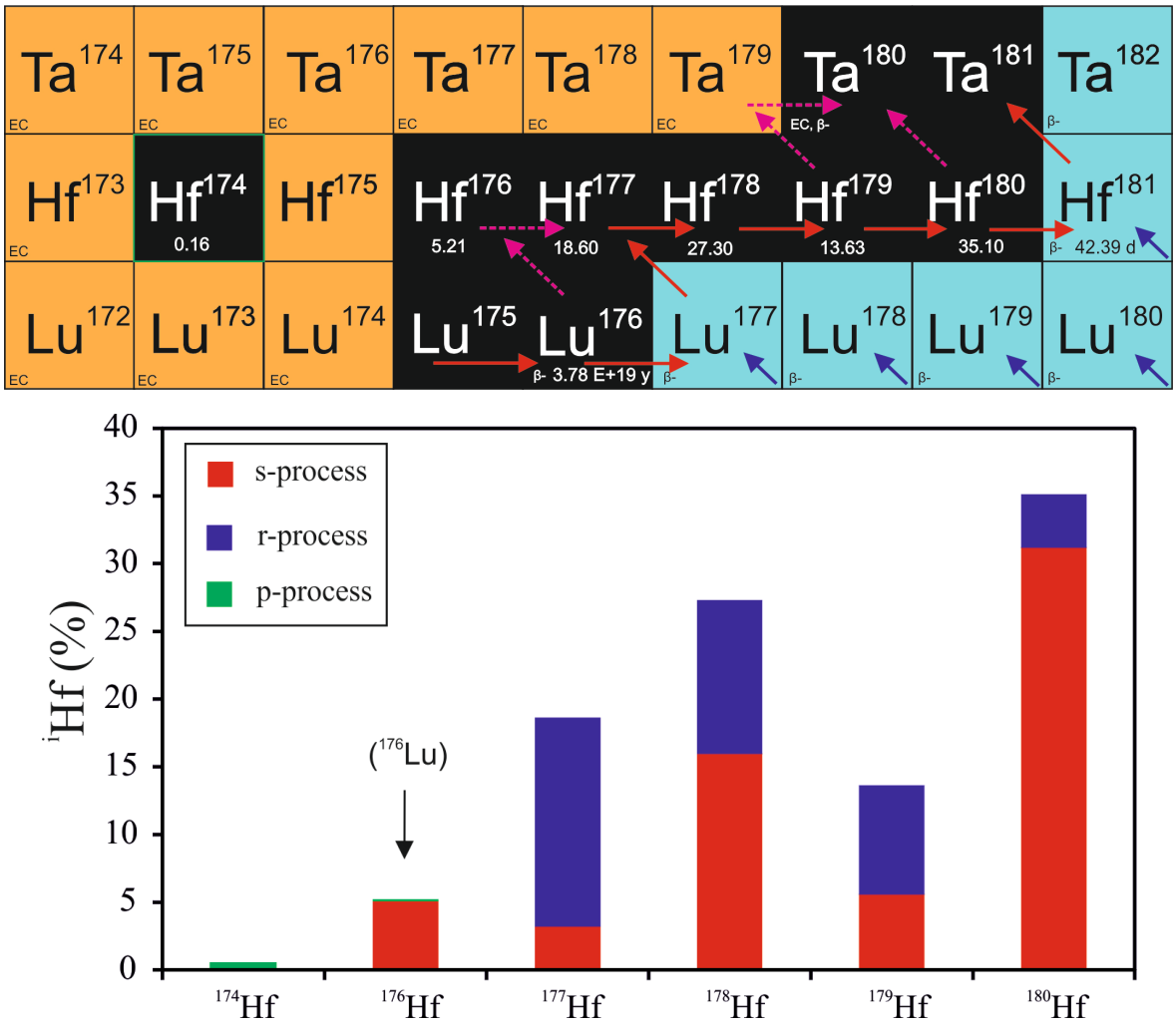

Fig. 1b: The Hf region of the chart of the nuclides (upper panel) and the nucleosynthetic contributions to the Hf isotope inventory (lower panel). Stable isotopes and their solar abundances are in black boxes, short-lived isotopes and their half-lives are in blue (β^- unstable) and orange (electron capture). The red arrows indicate the main path of s-process nucleosynthesis, dashed arrows minor branches. Blue arrows mark the decay path of nuclides produced in the r-process. ^{174}Hafnium is produced via the p-process (green), ^{177,178,179,180}Hf are produced via the s- and r-process. ^{176}Hafnium is produced via s-process branching (purple arrows), due to the partial excitation of ^{176}Lu to a short-lived nuclear isomer (Wisshak et al. 2006).^{176}Hf also gains contribution from ^{176}Lu decay (e.g., Bouvier et al. 2008).

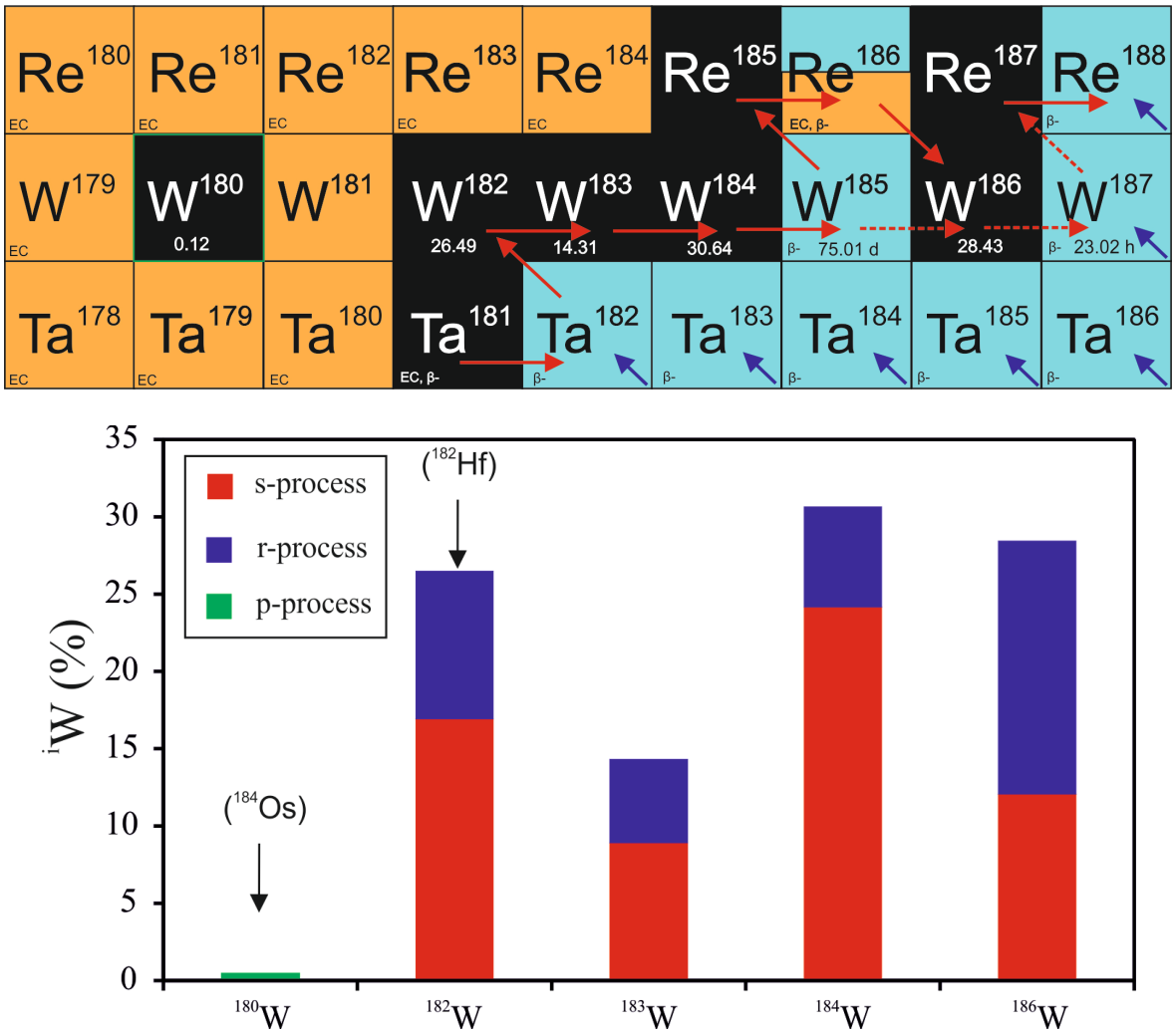

Fig. 1c: The W region of the chart of the nuclides (upper panel) and the nucleosynthetic contributions to the W isotope inventory (lower panel). Stable isotopes and their solar abundances are in black boxes, short-lived isotopes and their half-lives are in blue (β^- unstable) and orange (electron capture). The red arrows indicate the main path of s-process nucleosynthesis, dashed arrows minor branches. Blue arrows mark the decay path of nuclides produced in the r-process. ^{180}Tungsten is produced via the p-process (green), ^{182,183,184,186}W are produced via the s- and r-process. ^{180}Tungsten also gains contribution from ^{184}Os decay (Peters et al., 2014) and ^{182}W also gains contribution from ^{182}W decay (e.g., Kleine et al. 2002).

I.2 Presolar carrier phases in meteorites

1.2.1 Presolar grains

Presolar grains are interstellar dust grains that existed before the formation of the solar system. These grains are remnants from ancient stars and are ingredients that made up the solar system. Thus, they carry the nucleosynthetic fingerprints of their mother stars. Presolar grains can be usually found in the matrix of primitive meteorites where they generally escaped parent body processing. Presolar grains can make up to 0.1% of the mass of the

individual meteorite, however the mass of the presolar grains is usually less. (e.g., Nguyen and Messenger 2011; Zinner 2014).

Presolar grains have been first directly identified in 1987 by Lewis et al. They analyzed the rare gas isotopic compositions of the residues of stepwise acid leached primitive chondrites. They discovered that the fraction showing an anomalous Xe isotope composition is composed of acid insoluble, presolar nanodiamonds. This was the first direct evidence for a component that predates the formation of the solar system. Subsequently, many more presolar grains were found. At least five big groups of presolar grains have been identified till today: nano-diamonds, silicon carbide, graphite, oxides, and silicates.

As described above, nanodiamonds are the first type of presolar grains that have been discovered. Nanodiamonds are by far the most abundant presolar grain phases. They can make up to 0.1% of the absolute mass of chondrites. Nanodiamonds are small (~2nm). This makes direct analyses of nanodiamonds so far impossible. However, the exact origin of nandiamonds is still under debate. Whereas some studies claim that nanodiamonds are most likely formed within the solar system (Dai et al., 2002) other authors claim that nanodimamonds are more likely formed by a supernova shock-wave transformation of pre-formed organics in the interstellar (Stroud et al., 2011).

Siliconcarbide is strongly acid resistant, so that the separation of SiC from other meteorite components can be achieved by a stepwise acid leaching procedure. SiC does not form by nebular processes, and, thus, SiC grains observed in chondrites are all presumed to be presolar in origin. Typical SiC grains occur at μm scale sizes. Therefore, it is possible to perform direct isotope analyses by using, i.e., secondary ion mass spectrometry (SIMS). Therefore, SiC is the most studied presolar grain phase. Comprehensive analyses of Si, C, and N isotope compositions in presolar SiC grains have revealed that presolar grains can be divided into several groups of different nucleosynthetic origins. By far the most abundant SiC grains (>90%) are thought to condense from the envelopes of AGB stars and are referred as mainstream SiC grains. These grains show C, N and Si isotope compositions that are consistent with those of AGB stars, as being inferred from, e.g., infrared spectra or from nucleosynthetic theories (e.g., Lambert et al. 1986; Zinner et al. 1989; Alexander 1993; Hoppe et al. 1994; Speck et al. 1997; Nittler and Alexander 2003). These grains are also known to contain to significant amounts of heavy elements like Ba or W (Avila et al., 2012,

Avila et al. 2013). A minority of SiC grains show isotopic signatures of which the origin is still under debate, including core collapse supernovae, novae, post AGB stars or carbon stars (e.g., Amari et al. 2001a,b; Hoppe et al., 2000; Pelin 2006).

Presolar graphite is usually only present in the least altered meteorites (Huss and Lewis, 1995). Presolar graphite is much less chemical resistant than SiC. The separation of presolar graphite is much more difficult than the separation of SiC since presolar graphite shares many chemical and physical properties with other compounds of chondrites. Graphite grains are ususlly much larger than SiC grains, ranging from typically > 1μm up to 20μm in size (Amari et al. 1990). Presolar graphite is usually separated in two groups based on their density. High density graphite is thought to have condensed within the outflows of several stars, including, AGB stars, core collapse supernova and carbon stars (e.g., Amari et al. 2014; Nicolussi et al. 1998). Low density graphite in contrast is thought to most likely have condensed from the ejecta of a core collapse supernovae.

Presolar silicates are special among the presolar phases. Although astronomical observations suggested the presence of silicates among oxygen rich evolved stars (Waters et al., 1996; Demyk et al., 2000), they were the last major type of presolar grain to be discovered. This is because of they are more suscept to destruction, if compared to e.g., SiC. Thus, presolar silicates are only found in very primitive meteorites that virtually escaped aqueous and thermal alteration. Moreover, unlike SiC and similar as graphite, silicates cannot be isolated by acid dissolution techniques because they dissolve together with silicates formed in the solar system, which clearly dominate primitive meteorites. However, with the advent of NanoSIMS, and its unprecedented spatial resolution and high sensitivity, it became possible to detect presolar silicates. Presolar silicates were first identified as interplanetary dust particle on the basis of their anomalous oxygen isotopic compositions (Messenger et al., 2003) and, shortly thereafter, were first found in carbonaceous chondrites (Mostefaoui and Hoppe, 2004; Nguyen and Zinner, 2004; Nagashima et al., 2004). Presolar silicates can be as abundant as ~200 ppm in primitive meteorites. So far over ~700 presolar silicates have been identified, including olivines, pyroxenes and SiO_2. Mean sizes range from 0.1–1 μm. Nucleosynthetic sources for silicates are highly variable, ranging from different stages of AGB star evolution (e.g., Huss et al., 1994; Nittler et al., 1997; Gail et al. 2009) to supernovae environments (e.g., Messenger et al., 2005; Nittler et al., 2008; Nguyen and Messenger, 2014).

Presolar oxides were first identified via ion probe studies on individual grains (e.g., Huss et al. 1994, Hutcheon et al. 1994). The first presolar oxide phase to be discovered was corundum. Presolar oxides identified other than corundum are spinel ($MgAl_2O_4$), hibonite ($CaAl1_2O_{19}$), TiO_2, FeO, and $FeCr_2O_4$ (e.g., Nittler and Alexander, 1999; Nguyen et al. 2003; Zega et al. 2014). The grain size usually varies between 0.1 to 3 μm. The abundance in primitive meteorites can reach 100 ppm. Similar to presolar silicates and unlike SiC, oxides can also be formed within the solar system, thus the only way to identify presolar oxides, is by direct isotope measurements via SIMS. Similarly to silicates, various nucleosynthetic sources ranging from different stages of AGB evolutions to supernovae environments have been postulated for oxides. Unfortunately till to date, no isotope data are available for trace elements heavier than iron in presolar oxide and silicate grains.

I.1.2.2 Presolar grains as probes of early solar system processes

Presolar grains have survived dynamical processes in the early solar nebula, such as evaporation, condensation, mixing and collision of small bodies. Hence, they can be used to infer more information about the processes that took place on meteorite parent bodies or in the solar nebula. As described above, the solar system inherited a complex mixture of different types of presolar grains that not only differ in their compositions but also in their chemical and thermal stabilities. There are components being quite resistant to high temperatures like diamond or corundum (Al_2O_3). There are also components that are relatively easily destroyed already at low temperatures like i.e., graphite. On the other side there are also components that are sensitive to changes to the state of oxygen fugacity (fO_2). For instance, SiC survives to a higher metamorphic grade in reduced enstatite chondrites than in more oxidized ordinary or carbonaceous chondrites (e.g., Huss and Lewis, 1995, Huss et al., 1997) As a result, due to the different ranges of chemical and thermal stabilities, the relative abundance of the different types of presolar grains in different types of meteorites can provide direct information about information about the processes and environments that affected meteorites and their precursors materials.

For instance, Huss and Lewis (1995) demonstrated that the abundances of presolar grains when normalized to the content of fine-grained matrix, where the presolar grains reside in, are strongly correlated with the metamorphic grade (Fig.2). The abundances of the

different presolar grains drop significantly with increasing metamorphic grade. Thereby, not only the total abundances of the different presolar grains drop but also the relative abundances between the different presolar grains types change significantly depending on their thermal resistance. Thermally resistant phases as, for instance, diamond or SiC are less destroyed as thermally labile phases as, e.g., graphite (Fig. 2).

In addition to metamorphic effects in the meteorite parent body, the abundance of presolar grains also seems to be influenced by intra-solar nebula processing. Huss et al. (2003) showed that the relative presolar grain abundances of the least altered meteorites of the different meteorite groups correlate with volatile element depletion patterns (Fig.3). Thus, the presolar grain assemblages seem to be influenced by both parent body and intra- nebula processing before parent body alteration took place. Collectively, the assemblages and the relative abundances of the different presolar grain phases can give direct information about the processes which took place within the early solar system.

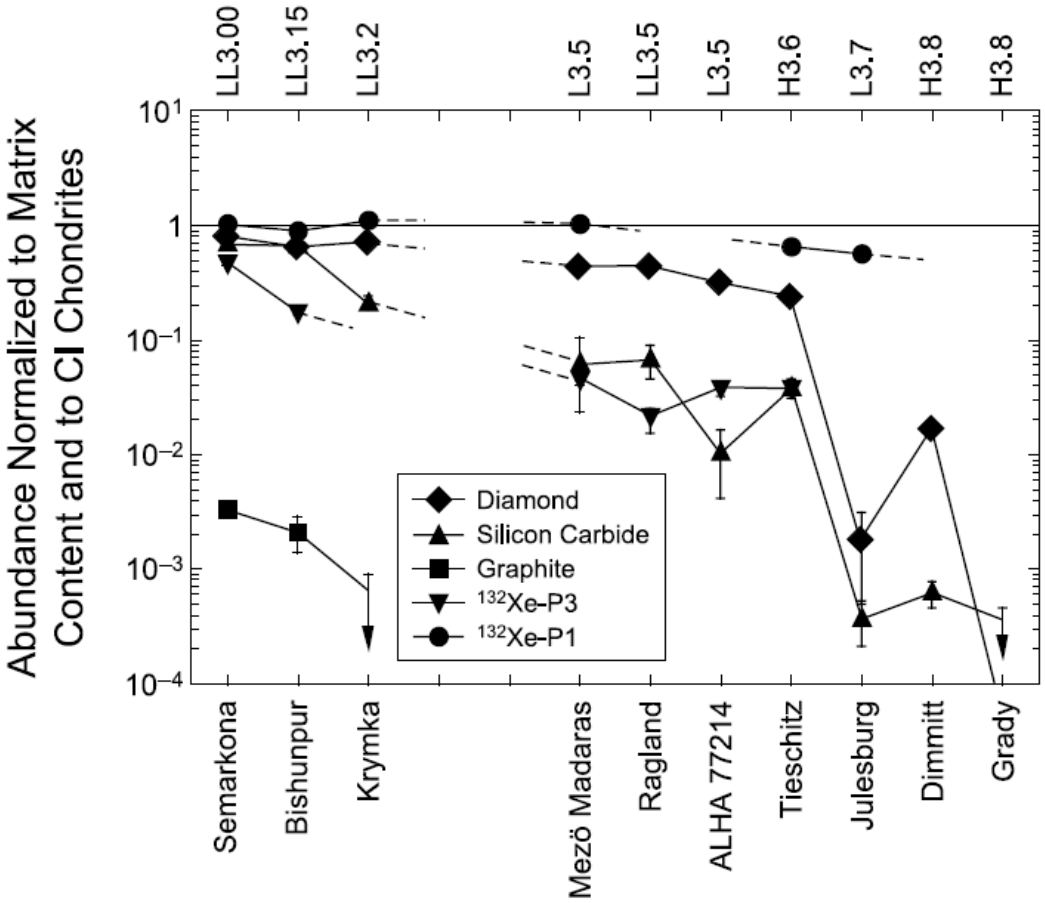

Fig. 2:Abundance of different presolar grains from as a function of metamorphic grade, illustrated for ordinary chondrites. Taken from Huss et al. (2006).

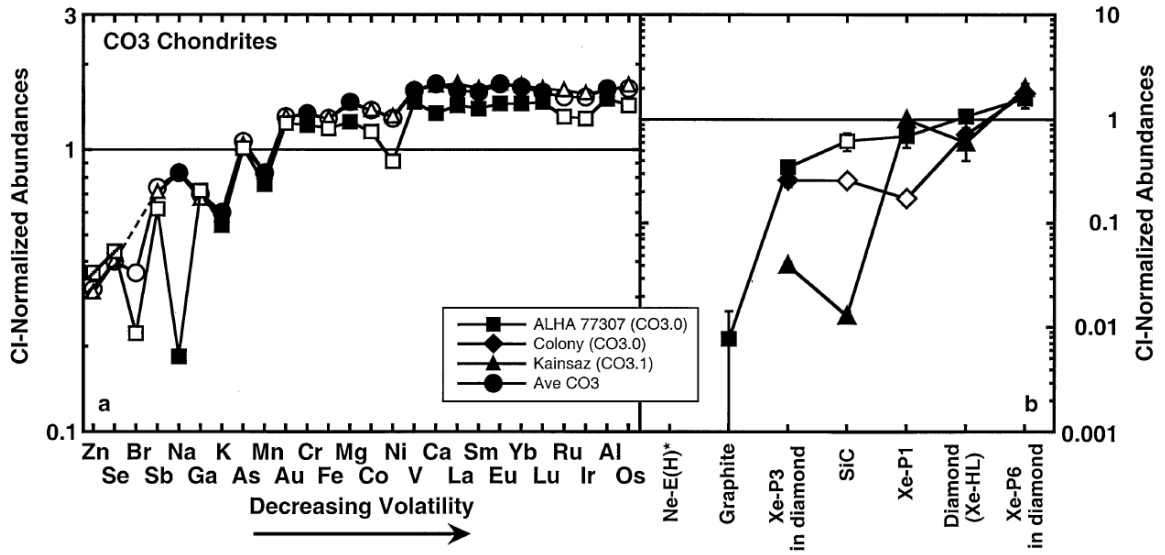

Fig.3: Relative abundances of different presolar grains as a function of volatile depletion illustrated for CO chondrites. Taken from Huss et al. (2003).

I.3 Chondrites

The solar system formed about 4.57 Ga (Amelin et al., 2010; Bouvier and Wadhwa, 2010) as a result of the gravitational collapse of a molecular cloud. Due to conservation of angular momentum, the infalling cloud material formed a circumstellar disk, the solar nebula, from which most of the Sun's mass accreted within a few hundred thousand years. In these early stages the young Sun is very active. Bipolar jets stream from the poles and rapid accretion events lead to radiation outbursts. However, with time the infall of cloud material onto the disk ceases and stopped at some point. Most of the dust and gas left in the disk after the infall ceased also accreted onto the Sun or was blown out by stellar radiation. Some of this disk material however accreted to form small bodies and later even planets (e.g., Pfalzner et al. 2015 for detailed review). The most primitive, i.e. unprocessed, fraction of these bodies are referred to as chondrite parent bodies. Chondrites, which are meteorite samples of such bodies, provide the best clues to the origin of the solar system. They are among the oldest known rocks, except for presolar grains their components formed during the birth of the solar system and their abundances of non-volatile elements are close to those in the solar photosphere. Chondrites are broadly ultramafic in composition, consisting largely of iron, magnesium, silicon, and oxygen. Chondrites derive their name from their texture: spherical, sub-spherical and sometimes ellipsoidal structures called chondrules. These range in size from about 0.1 to 4 mm diameter, with a few reaching centimeter sizes. Their abundances within a

given chondrite can vary significantly from only a few percent of the total volume of the meteorite to as much as 70%. Most chondrules are rich in the silicate minerals olivine and pyroxene (e.g., Scott and Krot, 2013). The other major components of chondrites are Ca-Al-rich inclusions, amoeboid olivine aggregates (AOAs), Fe-Ni metal alloys, sulfides and the opaque matrix (e.g., Brearley and Jones 1998; Scott and Krot 2005; Krot and Hutcheon, 2006). About 82% of all meteorite falls are chondrites (Norton 2002). Based on their bulk chemical compositions, chondrites are usually subdivided into three classes: carbonaceous (C), ordinary (O), and enstatite (E) chondrites. Carbonaceous chondrites obtained their names, because their matrices usually contain some amounts of carbonates and complex organic compounds (Cronin et al. 1988). The group of carbonaceous chondrites is traditionally considered to be a large group, reflecting not only chemical characteristics, but also differences in the oxidation states and also petrography. In fact, the carbonaceous chondrites not only comprise a group of essentially unfractionated element patterns and a high abundance of presolar grains (CI) but also comprise groups of highly volatile element depleted, refractory element enriched patterns and low proportions of presolar grains (CV and CO chondrites). Carbonaceous chondrites make up ca. 4% of all chondrites. Ordinary chondrites are by far the most abundant type of meteorites (~80% of all meteorites found). They are subdivided by based on their iron concentration into H, high iron, L, low iron and LL, with even lower iron contents than L chondrites. In LL chondrites Fe ususally only occurs as ferrous iron in silicates (Krot et al. 2005; Norton 2002). The third group, enstatite chondrites, usually tend to be enriched in enstatite from which they were named (60–80 vol. %; Krot et al. 2009; Norton 2002). Enstatite chondrites are strongly reduced, thus Fe is mainly occurring as metal. Enstatite chondrites are also subdivided by their iron content into high iron and low iron enstatite chondrites.

Furthermore, chondrites are further subdivided into various petrologic types based on the degree to which the chondrite has been aqueously and thermally altered. Originally based on the classification of Van Schmus and Wood, (1967) and subsequently revised and expanded (e.g., Sears and Dodd, 1988; Brearley and Jone, 1998; Weisberg et al. 2006), individual groups of chondrites are presently subdivided into 7 additional subgroups, each of which being characterized by certain chemical and visible caused of aqueous and thermal alteration (Table 1). Chondrites of petrologic type 3 are the most primitive chondrite samples. They do not show any signs of aqueous or thermal alteration. They kept their pristine mineralogy, thus no matrix mineral recrystallization took place, and chondrules with sharp

boundaries are very well visible. In contrast to that, i.e., chondrites characterized as petrologic grade 1 show a fine grained opaque matrix and no chondrules whereas the matrix of thermally altered meteorites of petrologic grade 4 to 7 is totally recrystallized, with chondrules only being visible as relicts. Chondrites of petrologic type 3 are usually further subdivided into groups 3.0 to 3.9 based on the thermoluminescence characteristics of the chondrule mesostasis (the very fine-grained minerals or quenched glass between larger crystals) (Sears et al., 1980), the CaO vs FeO concentrations in olivine chondrules (Scott et al., 1994), and further subtle changes in the composition of minerals (Grossman and Brearley, 2005), and the structure of organic materials (Bonal et al., 2006).

Table 1: Criteria for classifying chondrites according to their petrologic type (taken from Weisberg et al., 2006)

Criterion	1	2	3	4	5	6	7
Homogeneity of olivine compositions	—	>5% mean deviations		≤5%	Homogeneous		
Structural state of low-Ca pyroxene	—	Predominantly monoclinic		>20% monoclinic	≤20% monoclinic	Orthorhombic	
Feldspar	—	Minor primary grains		Secondary <2-μm grains	Secondary 2–50-μm grains	Secondary >50-μm grains	
Chondrule glass	Altered or absent	Mostly altered, some preserved	Clear, isotropic	Devitrified	Absent		
Metal: Maximum Ni (wt%)	—	<20 taenite minor or absent	>20 kamacite and taenite in exsolution relationship				
Sulfides: Mean Ni (wt%)	—	>0.5	<0.5				
Matrix	Fine grained opaque	Mostly fine-grained opaque	Opaque to transparent	Transparent, recrystallized			
Chondrule-matrix integration	No chondrules	Sharp chondrule boundaries		Some chondrules can be discerned, fewer sharp edges		Chondrules poorly delineated	Primary textures destroyed
Carbon (wt%)	3–5	0.8–2.6	0.2–1	<0.2			
Water (wt%)	18–22	2–16	0.3–3	<1.5			

Chapter II

S –process variability in early solar system materials – evidence from ^{174}Hf and ^{180}W in sequentially leached primitive chondrites

II.1 Introduction

Isotope analyses of bulk rock samples from Earth, Mars and different classes of meteorites provide valuable information about the possible isotopic variability of the materials that make up our solar system. Many isotope anomalies observed in extraterrestrial materials cannot be explained by mass-(in)dependent isotope fractionation, radioactive decay or cosmogenic effects, and they clearly result from incomplete mixing or heterogeneous distribution of nuclides from different sites of stellar nucleosynthesis (e.g., McCulloch and Wasserburg, 1978; Rotaru et al., 1992; Podosek et al., 1997; Dauphas and Schauble, 2016). Whereas systematic nucleosynthetic isotope anomalies are present for mid-mass range elements such as Ti, Cr and Mo among bulk solar system samples (e.g. Trinquier et al. 2009; Trinquier et al., 2007; Burkhardt et al. 2012a), heavy elements such as Hf, W, and Os from different solar system bodies tend to display uniform isotope compositions (Yokoyama et al. 2007; Sprung et al. 2010; Walker, 2012 Burkhardt and Schönbächler 2015).

Because presolar carrier phases in primitive chondrites, i.e., type 1 to 3, have not been completely homogenized by thermal metamorphism or aqueous alteration (e.g., Huss et al., 2003; Davidson et al. 2014; Leitner et al., 2016), nucleosynthetic isotope anomalies relative to terrestrial compositions can be revealed by progressive acid dissolution (e.g. Rotaru et al., 1992; Dauphas et al., 2002; Hidaka et al. 2003; Schönbächler et al. 2005), also including heavier elements (Reisberg et al. 2009; Yokoyama et al. 2010; Qin et al. 2011; Burkhardt et al. 2012b). In addition, nucleosynthetic isotope anomalies have also been directly measured in individual carrier phases, i.e., presolar grains (e.g., Lewis et al., 1987; Anders and Zinner, 1993; Ávila et al., 2012). Because of their strongly non-solar isotopic patterns, for instance in O, C, H and S (e.g., Boato, 1954; Clayton et al., 1973; Nittler et al. 2005; Hoppe and Zinner, 2012), these grains have been identified as condensates from distinct stellar environments. Therefore, presolar grains that survived the formation of the solar system now act as carriers of inherited isotope anomalies in chondrites. Isotope measurements on chemically separated phases (leachates and residues) from type 1 to 3 chondrites can thus (i) help to identify the nucleosynthetic processes and the stellar environment from which the pre-solar inventory in chondrites is derived and (ii) provide information about the variable conditions and processes within the solar nebula and perhaps about the preceding molecular cloud stage.

Hafnium and W isotope patterns are excellent tools to study the nucleosynthetic inventory of the solar system. The isotopes of both elements hold contributions from all nucleosynthetic

endmembers (Burbidge et al., 1957), namely the s-, r- and so called p-process. The isotope ^{174}Hf exlusively formed by the p-process. Likewise, ^{180}W is essentially a p-process nuclide, but contains a minor, 4.5 to 5.1% s-process contribution (Arlandini et al. 1999; Bisterzo et al. 2011; Bisterzo et al. 2014). All other Hf and W isotopes are formed by variable s- and r-process contributions. Exact r- and s-process contributions slightly vary between the different models for stellar nucleosynthesis.

The s-process nuclides between Sr and Bi are synthesized within asymptotic giant branch (AGB) stars. Several astrophysical settings have been suggested for the production of r-process nuclides, most of which are related to type II core collapse supernova and neutron star mergers (Burbidge et al., 1957; Lattimer et al., 1977; Wallerstein et al., 1997; Rosswog et al., 1999). Heavy p-process isotopes such as ^{174}Hf and ^{180}W are thought to be produced by photodisintegration during type II core collapse supernovae (Rauscher et al., 2013). In conjunction with the more abundant s- and r-isotopes of Hf and W, both ^{174}Hf and ^{180}W are of particular interest, because they can help discriminating between s- or r-process variations.

Sequential leaching experiments using primitive meteorites provide an established approach to study the presence of variable amounts of isotopically anomalous carrier phases (e.g., Rotaru et al., 1992; Dauphas et al., 2002; Hidaka et al., 2003; Schönbächler et al., 2005; Reisberg et al., 2009). First sequential leaching experiments for W (Burkhardt et al., 2012b) revealed significant non-radiogenic variations in ^{182}W and ^{183}W abundances. These variations were attributed to the presence of one or more carriers of s-process W (most likely presolar mainstream SiC and a secondary formed sulfide or silicate phase) that were mixed with r-process-rich components. Measurements of sequentially leached samples also revealed significant variations in Hf isotope patterns (Qin et al., 2011) that again were explained by variable contributions from s- and r-process Hf. However, all of these studies did not include analyses of the rare p-process isotopes ^{174}Hf (0.16 %) and ^{180}W (0.12 %). Both of these rare isotopes are formed by a complex chain of photodisintegration reactions of seed s- and r-process nuclides and β-decay reactions in supernovae. These reactions are thought to occur exclusively during core collapse supernovae (e.g., Arnould & Goriely, 2003; Rauscher et al., 2013). However, data for heavy p-process nuclides in leachate experiments are rare, as precise analyses are challenging due to their low isotope abundances. First studies on ^{174}Hf and ^{180}W for bulk rock samples, however, did not reveal any significant nucleosynthetic variations

compared to terrestrial standards, indicating a homogenous distribution of ^{174}Hf and ^{180}W within the solar nebula (Peters et al., 2014; Peters et al., 2016).

Here we report for the first time combined Hf and W isotope analyses on the same chondrite leach and residue fractions, also including the rare isotopes ^{174}Hf and ^{180}W. The aim of this study is to examine possible p-, s- and r-process isotope variations in heavy elements and to understand their origin. We also evaluate the effects of cosmic ray exposure which has previously been shown to significantly affect Hf and W isotope compositions in extraterrestrial samples (e.g., Sprung et al., 2010; Kruijer et al. 2013).

II.2 Methods

Between 0.5 and 1.5 g of eight meteorite samples (Murchison (CM2), MET 01070 (CM1 Kainsaz (CO3), Allende (CV3), Leoville (CV3), EET 96026 (C4/5), Indarch (EH4) and Tafassasset (primitive achondrite) and two terrestrial samples, one historic basalt from La Palma (LP 8), and one Archean gneiss from the ancient gneiss complex of southern Africa (AGC 351) were powdered and sequentially leached in reagents of increasing acid strength. Additional bulk rock analyses were carried out for Allende CV3, NWA 3118 CV3 and El Hammami H5. The terrestrial samples, that do not contain nucleosynthetic anomalies per definition, were included to test for analytical artifacts related to sample preparation procedures. The following two leaching procedures were carried out:

Recipe A (used for Kainsaz and MET 01070): Powders were first treated with 30 ml 6 M HCl at 120°C on a hotplate for 24 h and then split into leachate (‘leachate 1’) and residue. This residue was further leached in 30 ml 3:1 16 M HNO_3 - 29 M HF at 80°C for 24 h and again split into leachate (‘leachate 2’) and residue. The final residue was then pressure digested in 10 ml 1:1 16 M HNO_3 - 29 M HF at 180°C using Parr acid digestions bombs for 4 days. The leaching recipe was later modified slightly with the aim to achieve a more evenly distribution of Hf and W between the various fractions and thus to allow for reasonable precise measurements of ratios involving the minor p-process isotopes. Likewise, weak acid leaching steps were not carried out as they would not yield sufficient Hf and W for precise measurements, in particular for low abundance isotopes.

Recipe B (used for the remaining meteorites and the terrestrial samples): Sample powders were first treated with 30 ml 6 M HCl - 0.06 M HF at 80°C for 24 h and split into leachate ('leachate 1') and residue. The residue was further leached in 30 ml 20:1 16 M HNO_3 - 29 M HF and split into 'leachate 2' and residue. This residue was again digested using Parr bombs as described above.

One ml perchloric acid was added to all leachate 2 fractions and the final residue to oxidize residual organic materials and to re-dissolve secondary fluoride precipitates. All sample cuts were re-dissolved and dried down in 16 M HNO_3 three times to oxidize potentially remaining organic material and remove remaining fluorides and perchlorate. After re-dissolution and dry down in 6M HCl for the conversion of most cations into chlorides, all sample fractions were equilibrated in 6 M HCl - 0.06 M HF. From these solutions, 1% aliquots were taken for element concentration measurements by sector-field ICP-MS (Thermo Fisher Element 2) using calibration and measurement procedures similar to those described in Funk et al. (in revision). After evaporation to dryness, all sample splits were taken up in 1 M HCl – 0.1 M HF and refluxed at 120°C overnight.

Tungsten and Hf were separated from the sample matrix using Biorad cation exchange resin AG50W-X8, Biorad anion resin AG1-X8, Eichrom TEVA resin, and Eichrom Ln-Spec resin (Patchett and Tatsumoto 1980; Münker et al., 2001; Peters et al., 2015; Bast et al., 2015). The final Hf and W cuts generally had Yb/Hf, W/Hf, Ta/Hf, Hf/W, Ta/W, and Os/W $<1\times10^{-4}$. This is important as Peters et al. (2015) and Schulz et al. (2013) have shown that ultrapure analyte cuts are required for sufficiently accurate measurements of ^{174}Hf and ^{180}W. These requirements result from the low abundances of ^{174}Hf and ^{180}W and the large abundance of interfering ^{174}Yb and ^{180}Hf, respectively. Between chemical separation steps and after the final W and Hf elution, all samples were re-dissolved and dried down in 16 M HNO_3 – 10%vol H_2O_2 multiple times to remove possible organic residues. Oxidizing organic material is a critical step for W measurements because organic material can cause significant interferences on W isotopes (e.g., Kleine et al., 2002; Holst et al., 2015).

Total chemical yields from ion exchange separation were typically >60% for Hf and W. It is noteworthy that for some leach fractions the yields were < 10% Hf or W, rendering the sample split useless. These low yields might result from the formation of insoluble HFSE oxides (Yokoyama et al., 1999) or organic complexes as suggested by Willbold et al. (2011)

and Holst et al. (2015) who argued that insoluble organic complexes might form in organic-rich samples, leading to the retention of W in the Teflon lab ware.

Isotope analyses were performed in the joint Köln/Bonn clean lab facilities using a Thermo Fisher Neptune Multicollector ICP-MS, equipped with an Aridus membrane desolvator and an ESI SC2 autosampler. Two Faraday collectors were connected to amplifiers with$10^{12}\Omega$ resistors in their feedback loop, in order to improve the signal to noise ratio for the low abundance isotopes ^{174}Hf and ^{180}W and the interference monitors ^{172}Yb and ^{177}Hf, respectively (Peters et al., 2015). Hafnium isotope measurements were performed in static mode collecting the ion beams of masses 172 (^{172}Yb), 174 (^{174}Yb, ^{174}Hf), 175 (^{175}Lu), 176 (^{176}Yb, ^{176}Lu, ^{176}Hf), 177 (^{177}Hf), 178 (^{178}Hf), 179 (^{179}Hf) and 180 (^{180}W, ^{180}Ta, ^{180}Hf) with Faraday cups. The exponential law (Russel et al. 1978) was used for instrumental mass bias correction relative to a ^{179}Hf/^{177}Hf of 0.7325 and, in an alternative normalization procedure, relative to ^{180}Hf/^{177}Hf using a reference ratio of 1.8868. Tungsten isotope measurements were also performed in static mode by simultaneous collection of the ion beams of masses 177 (^{177}Hf), 178 (^{178}Hf), 180 (^{180}W, ^{180}Hf, ^{180}Ta), 181 (^{181}Ta), 182 (^{182}W), 183 (^{183}W), 184 (^{184}W, ^{184}Os), 186 (^{186}W, ^{186}Os) and 188 (^{188}Os) with Faradays cups. Measured values for ^{180}W/^{184}W, ^{182}W/^{184}W and ^{183}W/^{184}W were again corrected using the exponential law and normalization to ^{186}W/^{184}W = 0.9277. Additionally, ^{180}W/^{183}W, ^{182}W/^{183}W and ^{184}W/^{183}W were normalized to ^{186}W/^{183}W = 1.9859. In all cases, samples were bracketed by standard measurements and are reported using the ε notation, which gives the deviation of the measured ratios from the terrestrial standard value (Münster AMES Hf and NIST 3613 W) in parts per 10,000. Sample and standard intensities were matched to within 10% to avoid possible intensity-related analytical bias. We aimed at ion beam intensities of ~100 mV for the minor isotopes ^{174}Hf and ^{180}W to ensure sufficient precision. External reproducibility (2 rsd) of about ±66 ppm could be achieved for ^{174}Hf/^{177}Hf, ^{174}Hf/^{178}Hf and of about ±10 ppm for ^{180}Hf/^{177}Hf, ^{179}Hf/^{178}Hf, respectively. For W isotope analyses typical external reproducibility of ±88 ppm could be achieved for ^{180}W/^{183}W, ^{180}W/^{184}W, and of ca. ±8 ppm for ^{183}W/^{184}W and ^{184}W/^{183}W, respectively. For both, W and Hf analyses, the external reproducibility declined with decreasing analyte concentrations. Total blanks were <1 ng Hf and W for all autoclave-digested residues and <50 pg for all leachates.

II.3 Results

II.3.1 Concentration measurements

The results of the concentration analyses of leachates and residues are displayed in Fig. 1 a and b, and Hf and W abundances for the individual leach fractions are given in Tables 1 and 2. For both leaching procedures, most of the Hf was in leachates 1 (40 to 59%) and leachates 2 (20 to 53%). Smaller amounts of Hf were usually observed in residues (5 to 37%). For W, the elemental pattern is quite similar: most W is recovered in leachates 1 (44 to 63%) and leachates 2 (21 to 46%). Smaller fractions (10 to 28%) of W are present in residues. Variations in Hf and W contributions among the leachates band residues are mainly due to the different mineralogical inventories of different chondrites, possibly because chondrites are made up by different percentages of components such as matrix and chondrules. They are furthermore characterized by their different mineral contents, i. e., variable abundances of silicate, metal and sulfides. While olivine and enstatite are abundant in type 3 or higher carbonaceous or enstatite chondrites, respectively, phyllosilicates dominate in type 1 and 2 chondrites (e.g., Van Schmus and Wood, 1967).

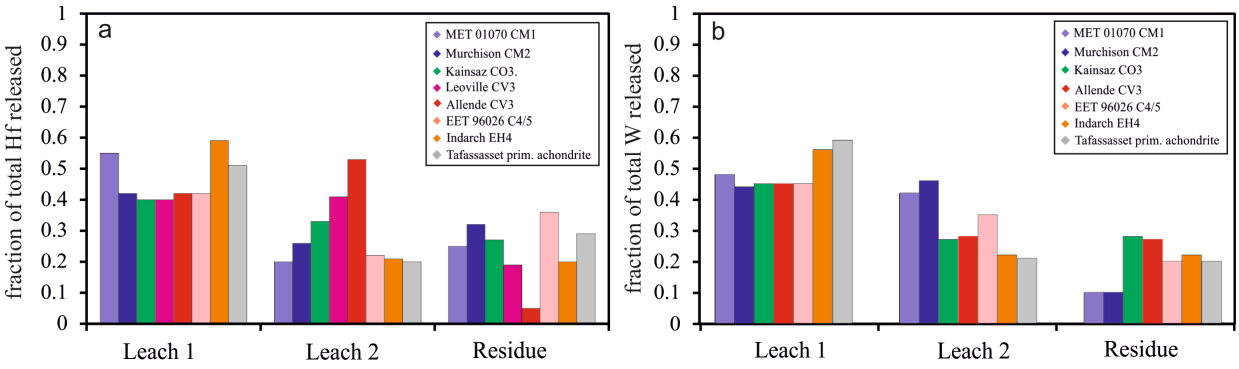

Figure 1 a, b: Release of Hf and W during to sequential leaching. The overall release pattern is broadly similar for all chondrites. Slight differences are due the variable mineralogical inventory of different meteorites. The data for the different meteorites are given in color as illustrated in the legend.

II.3.2 Isotope compositions

Results from Hf and W isotope analyses are given in Tables 1 and 2 and Figs. 2 to 3. All data are expressed in the ε notation relative to AMES Hf or NIST 3613 W standard. For ε^{180}Hf (normalized to ^{179}Hf/^{177}Hf), clearly resolvable isotope anomalies from –2.96±0.13 ε to

4.08±0.17 ε are observed for leachates 1 and residues of Allende CV3, Leoville CV3, Kainsaz CO3, Murchison CM2, and MET 01070 CM1. Leachates 2 are only anomalous for Kainsaz and MET 01070. Isotope anomalies in ε^{174}Hf vary between -1.76±0.66 ε of leachate 1 of Murchison and 3.95±2.98 ε of the leachate 2 of MET 01070. In addition to the non-radiogenic Hf isotopes, a significant spread in radiogenic ε^{176}Hf is observed within the sample set ranging from +14.80 ε in EET96026 residue to +36.05 ε in EET 96026 leachate 1. Note that the Hf isotope values for leachate 1 of Leoville, the leachate 2 of EET 96026, and the residues of Kainsaz and MET 01070 have been inferred using the assumption that all of these meteorites lack bulk rock anomalies in non-radiogenic Hf. These findings are consistent with the analyzed bulk rock chondrite data of this study and literature data by Sprung et al. (2010), Akram et al. (2013), and Peters et al. (2017).

Table 1. Hafnium isotope and release data

Sample	Hf released (%)	$\varepsilon^{174}Hf^{b}$	$\varepsilon^{176}Hf^{b}$	$\varepsilon^{178}Hf^{b}$	$\varepsilon^{180}Hf^{b}$	$\varepsilon^{174}Hf^{b}$	$\varepsilon^{176}Hf^{b}$	$\varepsilon^{177}Hf^{b}$	$\varepsilon^{179}Hf^{b}$
		mass bias correction relative to $^{179}Hf/^{177}Hf$				mass bias correction relative to $^{180}Hf/^{177}Hf$			
MET 01070[a]		0.00		0.00	0.00	0.00		0.00	0.00
leachate 1	55	-0.32 ± 1.45	17.98 ± 0.15	-1.40 ± 0.11	-1.31 ± 0.15	-0.97 ± 1.48	17.90 ± 0.14	0.92 ± 0.11	1.83 ± 0.15
leachate 2	20	3.95 ± 2.98	32.70 ± 0.26	3.55 ± 0.10	4.08 ± 0.17	4.40± 3.03	32.35 ± 0.36	-2.17 ± 0.11	-4.90 ± 0.14
Residue[a]	25	-2.49 ± 4.15		0.22 ± 0.72	-0.40 ± 0.80	1.42 ± 4.22		-0.28 ± 0.50	-0.08 ± 0.97
Murchison		-0.41± 0.57	22.26±0.49	-0.13±0.14	0.02±0.19	-0.35 ± 0.62	22.24 ± 0.62	0.14 ± 0.11	0.10 ± 0.23
leachate 1	42	-1.76 ± 0.66	16.41 ± 0.11	-1.78 ± 0.09	-1.85 ± 0.10	-2.52 ± 0.66	16.27 ± 0.09	1.20 ± 0.09	2.38 ± 0.09
leachate 2	26	-0.10 ±1.66	22.24 ± 0.15	0.04 ± 0.11	0.13 ± 0.14	-0.16 ± 1.76	22.57 ± 0.14	-0.02 ± 0.11	-0.08 ± 0.14
Residue	32	1.12 ± 0.71	29.96 ± 0.11	1.92 ± 0.08	2.39 ± 0.08	2.35 ± 0.71	29.81 ± 0.11	-1.13 ± 0.09	-2.76 ± 0.09
Kainsaz[a]		0.00		0.00	0.00	0.00		0.00	0.00
leachate 1	40	-1.51 ± 1.50	16.76 ± 0.25	-2.52 ± 0.10	-2.96 ± 0.13	-2.86 ± 1.46	16.51 ± 0.19	1.50 ± 0.08	3.51 ± 0.13
leachate 2	33	1.13 ± 1.13	31.56 ± 0.16	1.42 ± 0.07	1.43 ± 0.10	2.10 ± 1.41	31.09 ± 0.15	-0.95 ± 0.09	-1.86 ± 0.09
residue[a]	27	0.87 ± 2.65		2.01 ± 0.71	2.65 ± 0.85	1.69 ± 2.89		-1.06 ± 0.44	-2.94 ± 0.99
Leoville[a]		0.00		0.00	0.00	0.00		0.00	0.00
leachate 1[a]	40	-1.04 ± 1.11		-0.40 ± 0.13	-0.49 ± 0.19	-1.35 ± 1.12		0.21 ± 0.11	0.56 ± 0.18
leachate 2	41	0.42 ± 0.69	27.97 ± 0.11	0.00 ± 0.08	0.00 ± 0.11	0.39 ± 0.70	27.91 ± 0.11	-0.01 ± 0.08	0.02 ± 0.12
Residue	19	1.29 ± 1.73	27.98 ± 0.25	0.84 ± 0.09	1.04 ± 0.19	1.99 ± 1.69	27.89 ± 0.25	-0.43 ± 0.11	-1.23 ± 0.19
Allende		-0.30 ± 0.54	23.26 ± 0.11	0.09 ± 0.07	0.08 ± 0.08	-0.54 ± 0.53	23.19 ± 0.11	-0.05 ± 0.07	-0.11 ± 0.08
leachate 1	42	-0.07 ± 0.93	22.41 ± 0.12	-0.21 ± 0.09	-0.36 ± 0.09	-0.85 ± 0.86	22.32 ± 0.11	0.09 ± 0.10	0.32 ± 0.09
leachate 2	53	-0.65 ± 0.66	23.39 ± 0.11	0.10 ± 0.08	0.14 ± 0.11	-0.64 ± 0.67	23.33 ± 0.09	-0.02 ± 0.09	-0.14 ± 0.09
Residue	5	1.46 ± 2.50	29.02 ± 0.30	2.52 ± 0.15	3.08 ± 0.21	3.22 ± 2.49	29.04 ± 0.31	-1.48 ± 0.17	-3.53 ± 0.20
EET 96026[a]		0.00		0.00	0.00	0.00		0.00	0.00
leachate 1	41	1.03 ± 2.20	36.05 ± 0.17	-0.05 ± 0.09	-0.18 ± 0.17	0.02 ± 2.20	36.04 ± 0.18	0.03 ± 0.07	0.14 ± 0.14
leachate 2	22	-0.95 ± 4.62		-0.13 ± .0.23	0.29 ± 0.38	0.01 ± 4.66		0.06 ± 0.21	-0.01 ± 0.32
Residue	37	-0.59 ± 0.98	14.80 ± 0.14	0.13 ± 0.08	0.03 ± 0.09	-0.11 ± 1.00	14.71 ± 0.14	-0.07 ± 0.09	-0.15 ± 0.09
Indarch									
leachate 1	59	0.49 ± 0.90	24.22 ± 0.11	-0.12 ± 0.08	0.08 ± 0.11	0.87 ±1.00	24.43 ± 0.12	0.16 ± 0.09	0.09 ± 0.08
leachate 2	21								
Residue	20								
Tafassasset									
leachate 1	51	-1.18 ± 2.53	19.96 ± 0.25	0.18 ± 0.10	0.11 ± 0.20	-1.09 ± 2.46	19.82 ± 0.20	-0.15 ± 0.10	-0.21 ± 0.13
leachate 2	20								
Residue	29								
La Palma basalt 8[d]		0.41 ± 1.37	28.07 ± 0.06	-0.02 ± 0.06	-0.09 ± 0.08	0.53 ± 0.86	28.04 ± 0.07	-0.01 ± 0.06	0.02 ± 0.07
leachate 1	30	0.67 ± 0.66	28.24 ± 0.11	-0.02 ±0.09	-0.07 ± 0.10	0.44 ± 0.67	28.14 ± 0.09	-0.04 ± 0.09	-0.07 ± 0.09
leachate 2	43	0.81 ± 3.16	27.90 ± 0.24	-0.08 ± 0.14	-0.24 ± 0.22	2.47 ± 3.54	27.92 ± 0.22	0.04 ± 0.12	0.19 ± 0.19
Residue	27	-0.52 ± 0.66	27.97 ± 0.11	0.01 ± 0.09	-0.03 ± 0.11	-0.50 ± 0.66	28.00 ± 0.09	-0.01 ± 0.09	0.01 ± 0.09
AGC 351[d]		-	-				-		
leachate 1		-1.57 ± 2.36	0.13 ± 0.18	0.11 ± 0.11	0.17 ± 0.14	0.56 ± 2.42	0.20 ± 0.20	-0.03 ± 0.07	-0.15 ± 0.10
leachate 2		0.46 ± 2.03	28.16 ± 0.20	0.06 ± 0.09	0.13 ± 0.12	0.20 ± 2.09	28.24 ± 0.18	0.01 ± 0.08	-0.09 ± 0.11
Residue		-0.12 ± 0.71	-39.31 ± 0.08	0.00 ± 0.08	0.03 ± 0.11	-0.06 ± 0.77	-39.25 ± 0.13	0.03 ± 0.08	-0.01 ± 0.09
Bulk Samples									
NWA 3118		-0.38 ± 0.68	23.17 ± 0.11	-0.03 ± 0.08	-0.06 ± 0.11	-0.42 ± 0.73	23.18 ± 0.10	0.02 ± 0.09	0.05 ± 0.10
Allende		-0.48 ± 0.66	23.19 ± 0.11	0.05 ± 0.09	0.01 ± 0.11	-0.46 ± 0.66	23.19 ± 0.10	-0.05 ± 0.09	-0.08 ± 0.09
El Hammami		0.78 ± 0.67	15.33 ± 0.10	0.19 ± 0.085	-0.25 ± 0.11	0.08 ± 0.67	14.97 ± 0.11	-0.28 ± 0.08	-0.11 ± 0.10

[a.] Data refer to samples with calculated data inferred from mass balance calculations assuming terrestrial compositions in $\varepsilon^{174}Hf$ (0.00), $\varepsilon^{177}Hf$ (0.00), $\varepsilon^{179}Hf$ (0.00) and $\varepsilon^{180}Hf$ (0.00), respectively. Uncertainties are given by the error propagated 2SD of the individual variables (concentration, isotope signature) using Monte Carlo Simulation (Sprung et al. 2013).

[b.] Uncertainties on the isotope ratios are given as the 2SD of repeated measurements of the bracketing standards matched to the individual samples. Uncertainties on calculated bulk rocks are given by the error propagated 2SD of the individual variables (concentration, isotope signature) using Monte Carlo Simulation (Sprung et al. 2013).

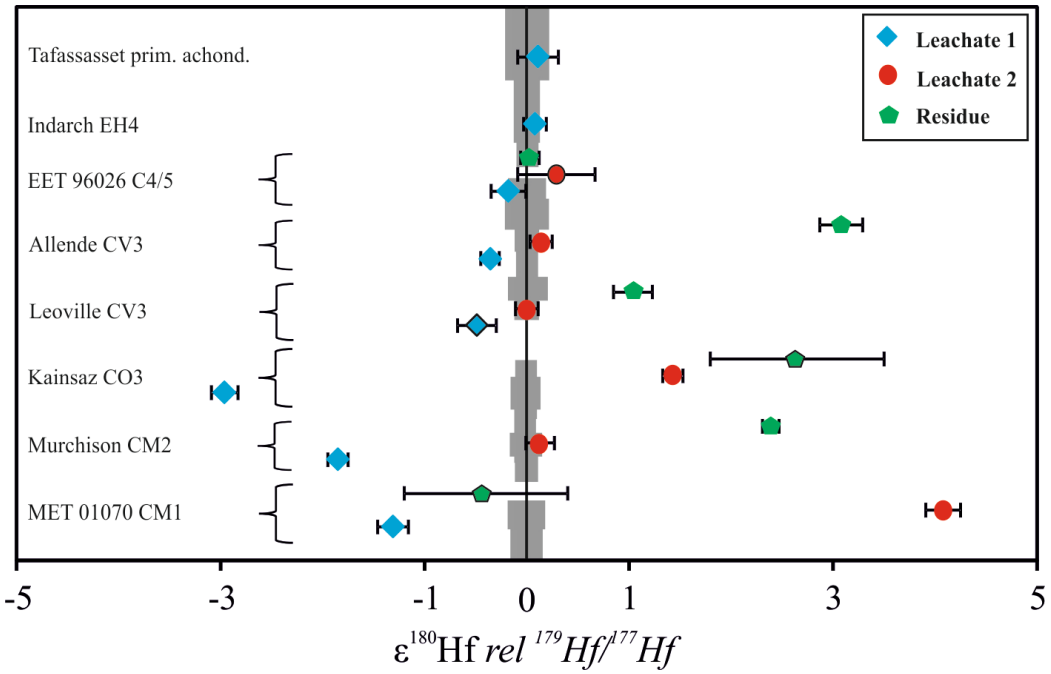

Figure 2a: ε^{180}Hf for all meteorite samples mass bias corrected to ^{179}Hf/^{177}Hf. All isotope ratios are reported relative to the Hf AMES standard. The grey bars represent 2S.D. of the repeated accompanying measurements of the Hf AMES standard. Analytical precisions heavily depend on the amount of Hf measured. Reported uncertainties for samples are the external reproducibility (2 S.D.) of the repeated measurement of the bracketing standard measured the same day. Calculated isotope compositions are marked by a black frame.

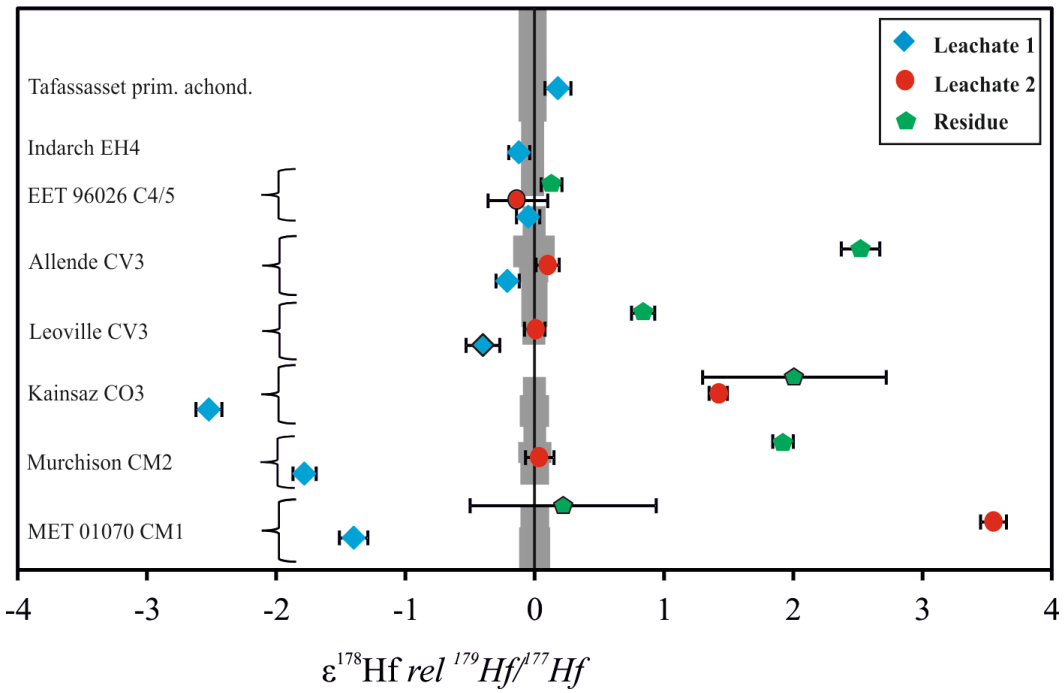

Figure 2b: ε^{178}Hf for all meteorite samples mass bias corrected to ^{179}Hf/^{177}Hf. All isotope ratios are reported relative to the Hf AMES standard. The grey bars represent 2S.D. of the repeated accompanying measurements of the Hf AMES standard. Analytical precisions heavily depend on the amount of Hf measured. Reported uncertainties for samples are the external reproducibility (2 S.D.) of the repeated measurement of the bracketing standard measured the same day. Calculated isotope compositions are marked by a black frame.

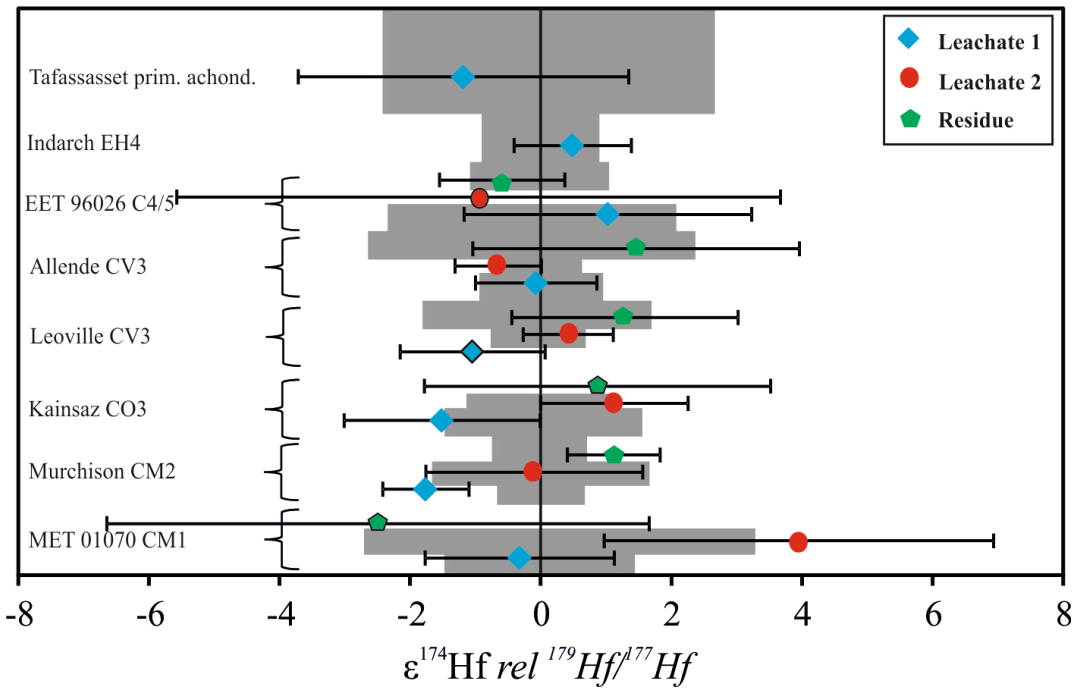

Figure 2c: ε^{174}Hf for all meteorite samples mass bias corrected to ^{179}Hf/^{177}Hf. All isotope ratios are reported relative to the Hf AMES standard. The grey bars represent 2S.D. of the repeated accompanying measurements of the Hf AMES standard. Analytical precisions heavily depend on the amount of Hf measured. Reported uncertainties for samples are the external reproducibility (2 S.D.) of the repeated measurement of the bracketing standard measured the same day. Calculated isotope compositions are marked by a black frame.

For ε^{183}W, large isotope anomalies are only observed for leach fractions of the MET 01070 CM1 and Murchison CM chondrites (2.58±0.16 to -8.18±0.36). Unlike for Hf, much smaller variations are observed for ε^{183}W in the Allende CV3 and Kainsaz CO3 chondrites (0.33±0.09 to -0.34±0.08). All other leaching fractions show terrestrial W isotope compositions within uncertainty. The results for ε^{180}W (normalized to ^{186}W/^{184}W) range from +8.4 to -33.5 ε with large anomalies being again restricted to the Murchison and MET 01070 leachates 1 and residues. Much smaller variations are observed for leachates 1 and 2 and the residues of Allende and Kainsaz (2.01±1.34 to -1.59±0.88). In addition to the non-radiogenic W isotopes, partly radiogenic ε^{182}W ranges from -13.8 ε in the Murchison residue to +1.5 ε in the MET 01070 leachate 1. Note that the non-radiogenic W isotope values for the residues of, MET 01070, Kainsaz, Indarch and Tafassasset have been inferred using the assumption that all of these meteorites lack bulk rock anomalies for those W isotopes which is consistent with bulk rock W isotope data in this study and by, e.g., Kleine et al. (2004) and Becker et al. (2015).

Table 2. Tungsten isotope and release data

Sample	W released (%)	$\varepsilon^{180}W^b$	$\varepsilon^{182}W^b$	$\varepsilon^{183}W^b$		$\varepsilon^{180}W^b$	$\varepsilon^{182}W^b$	$\varepsilon^{184}W^b$
		mass bias correction relative to $^{186}W/^{184}W$				mass bias correction relative to $^{186}W/^{184}W$		
MET 01070[a]					0.00			0.00
leachate 1	48		7.10 ± 2.98	1.52 ± 0.15	2.36 ± 0.14	1.91 ± 3.01	-1.70 ± 0.15	-1.57 ± 0.14
leachate 2	42		-2.50 ± 3.07	-2.84 ± 0.17	-0.83 ± 0.15	-1.01 ± 2.13	-1.74 ± 0.16	0.54 ± 0.14
residue[a]	10				-7.58 ± 2.38			5.09 ± 1.61
Murchison			-0.47 ± 1.89	-1.77 ± 0.33	0.11 ± 0.24	0.41 ± 1.67	-1.77 ± 0.09	-0.07 ± 0.17
leachate 1	44		8.48 ± 3.48	1.37 ± 0.17	2.58 ± 0.16	5.22 ± 3.54	-1.96 ± 0.14	-1.79 ± 0.14
leachate 2	46		-2.01 ± 0.88	-2.21 ± 0.10	-0.50 ±0.08	-0.47 ± 0.87	-1.29 ± 0.09	0.33 ± 0.08
Residue	10		-33.52 ± 5.54	-13.84 ± 0.52	-8.18 ± 0.36	-17.12 ± 5.54	-3.14 ± 0.25	5.40 ± 0.28
Kainsaz[a]					0.00			0.00
leachate 1	45		2.01 ± 1.34	-2.14 ± 0.10	0.33 ± 0.09	1.29 ± 1.32	-2.46 ± 0.09	-0.22 ± 0.08
leachate 2	27		0.34 ± 2.20	-1.62 ± 0.13	-0.22 ± 0.12	0.16 ± 2.23	-1.31 ± 0.12	0.15 ± 0.11
residue[a]	28				-0.33 ± 0.21	-		0.21 ± 0.18
Allende			0.14 ± 0.66	-1.79 ± 0.07	0.01 ± 0.06	0.04 ± 0.63	-1.85 ± 0.06	0.00 ± 0.05
leachate 1	45		1.30 ± 1.10	-1.85 ± 0.11	0.29 ± 0.09	0.26 ± 1.05	-2.29 ± 0.09	-0.18 ± 0.08
leachate 2	28		-0.14 ± 1.23	-1.42 ± 0.10	-0.12 ± 0.09	0.61 ± 1.22	-1.30 ± 0.10	0.09 ± 0.08
Residue	27		-1.59 ± 0.88	-2.08 ± 0.10	-0.34 ± 0.08	-0.92 ± 0.87	-1.69 ± 0.09	0.22 ± 0.08
EET 96026			1.40±2.55	-1.85 ± 0.13	0.11 ± 0.11	0.98 ± 2.60	-2.01 ± 0.12	-0.11 ± 0.11
leachate 1	45		3.01 ± 4.34	-2.31 ± 0.22	0.13 ± 0.20	2.61 ± 4.45	-2.54 ± 0.20	-0.12 ± 0.19
leachate 2	35		-0.72 ± 1.16	-1.78 ± 0.09	0.00 ± 0.09	-0.91 ± 1.17	-1.75 ± 0.09	-0.01 ± 0.08
Residue	20		1.52 ± 8.01	-0.92 ± 0.30	0.27 ± 0.29	0.63 ± 8.03	-1.27 ± 0.28	-0.25 ± 0.28
Indarch[a]					0.00			0.00
leachate 1	56		3.23 ± 4.68	-1.84 ± 0.22	0.18 ± 0.21	2.90 ± 3.65	-1.98 ± 0.20	-0.12 ± 0.20
leachate 2	22		-3.01 ± 3.95	-1.97 ± 0.20	-0.13 ± 0.19	-0.61 ± 3.90	-2.13 ± 0.19	0.10 ± 0.17
Residue	22				-0.33 ± 0.57			0.20 ± 0.46
Tafassasset[a]					0.00			0.00
leachate 1	63		1.21 ± 2.69	-1.99 ± 0.16	-0.12 ± 0.15	1.42 ± 2.65	-1.81± 0.15	0.08 ± 0.14
leachate 2	21		-1.74 ± 2.95	-1.89 ± 0.16	0.07 ± 0.15	-1.92 ± 2.90	-2.03 ± 0.15	-0.05 ± 0.14
Residue	16				0.38 ± 0.65			-0.25 ± 0.60
La Palma basalt 8			0.38±0.56	-0.06 ± 0.06	-0.04 ± 0.04	0.18 ± 0.57	0.06 ± 0.04	0.03 ±0 .05
leachate 1	38		-0.14 ± 0.88	-0.10 ± 0. 10	-0.08 ± 0. 08	-0.50 ± 0. 87	0.10 ± 0. 09	0.06 ± 0. 08
leachate 2	32		1.00 ± 1.15	-0.05 ± 0.09	0.00 ± 0.07	0.72 ± 1.18	0.00 ± 0.08	0.00 ± 0.07
Residue	30		0.39 ± 0.88	-0.07 ± 0.10	-0.03 ± 0.08	0.45 ± 0. 87	0.07 ± 0.09	0.03 ± 0.08
AGC 351[d]								-
leachate 1			0.69 ± 0.88	0.01 ± 0.10	0.03 ± 0. 08	0.63 ± 0.87	-0.10 ± 0.09	-0.05 ± 0.08
leachate 2			0.63 ± 0.88	0.13 ± 0.10	0.15 ± 0.08	0.59 ± 0.87	-0.10 ± 0.09	-0.14 ± 0.08
Residue			-1.80 ± 1.91	-0.05 ± 0.14	-0.08 ± 0.13	-1.73 ± 2.04	0.07 ± 0.15	0.06 ± 0.09
bulk samples:								
NWA 3118			1.05 ± 1.10	-1.91 ± 0.10	0.07 ± 0.09	0.74 ± 1.06	-1.97 ± 0.11	-0.06 ± 0.08
Allende			1.78 ± 2.10	-1.74 ± 0.14	0.09 ± 0.13	1.49 ± 2.11	-1.86 ± 0.14	-0.06 ± 0.12
El Hammami			1.54 ± 0.91	-2.34 ± 0.10	0.02 ± 0.09	1.15 ± 0.95	-2.35 ± 0.11	0.00 ± 0.09

[a] Data refer to samples with calculated data inferred from mass balance calculations assuming terrestrial compositions in $\varepsilon^{183}W$ (0.00) and $\varepsilon^{184}W$ (0.00), respectively. Uncertainties are given by the error propagated 2SD of the individual variables (concentration, isotope signature) using Monte Carlo Simulation (Sprung et al. 2013).

[b.] Uncertainties on the isotope ratios are given as the 2SD of repeated measurements of the bracketing standards matched to the individual samples. Uncertainties on calculated bulk rocks are given by the error propagated 2SD of the individual variables (concentration, isotope signature) using Monte Carlo Simulation (Sprung et al. 2013).

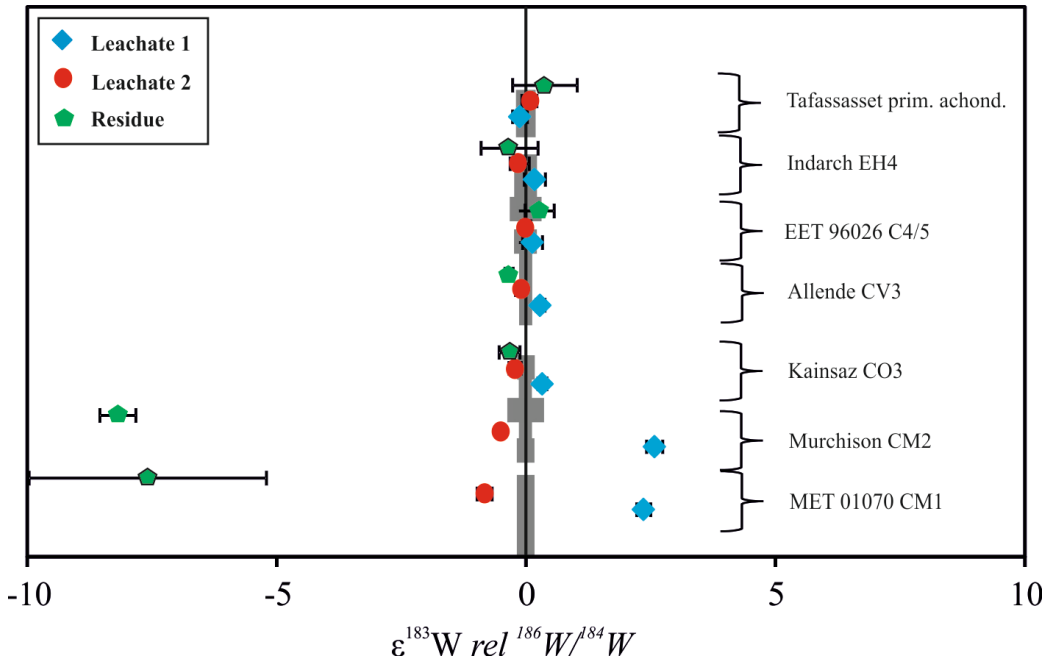

Figure 3 a: $\varepsilon^{183}W$ for all meteorite samples, mass bias corrected to $^{186}W/^{184}W$. All isotope ratios are reported relative to the NIST 3613 W standard. The grey bars represent 2S.D. of the repeated accompanying measurements of the NIST 3613 W standard. Analytical precisions heavily depend on the amount of W measured Reported uncertainties for samples are the external reproducibility (2 S.D.) of the repeated measurement of the bracketing standard measured the same day. Calculated isotope compositions are marked by a black frame.

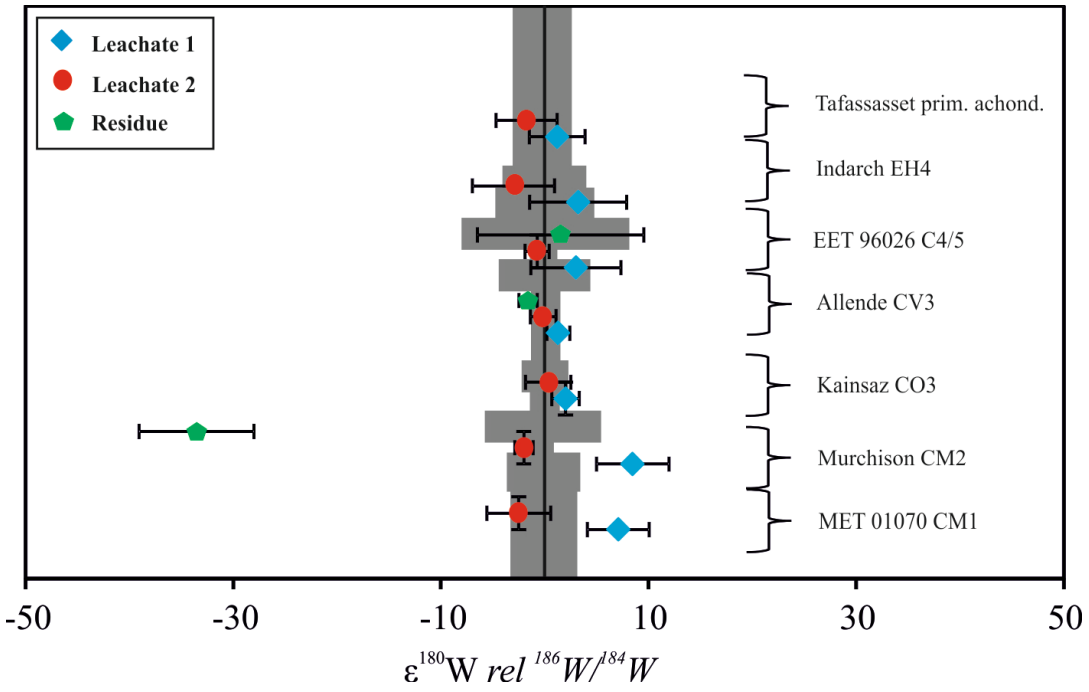

Figure 3 b: $\varepsilon^{180}W$ for all meteorite samples, mass bias corrected to $^{186}W/^{184}W$. All isotope ratios are reported relative to the NIST 3613 W standard. The grey bars represent 2S.D. of the repeated accompanying measurements of the NIST 3613 W standard. Analytical precisions heavily depend on the amount of W measured. Reported uncertainties for samples are the external reproducibility (2 S.D.) of the repeated measurement of the bracketing standard measured the same day. Calculated isotope compositions are marked by a black frame.

Both terrestrial samples (LP 8 and AGC 351) show terrestrial Hf and W isotopic signatures within analytical uncertainty for all leaching fractions. This result demonstrates the reliability of the applied leaching and ion exchange procedures and renders analytical artefacts unlikely. This view is also corroborated by analyses of bulk rock samples of NWA 3118 and Allende that do not show any resolvable anomalies for Hf or W isotopes other than radiogenic effects in ^{176}Hf and ^{182}W, and possibly ^{180}W (El Hammami) (e.g., Sprung et al. 2010; Peters et al. 2014; Becker et al. 2015; Peters et al. 2016).

II.4 Discussion

II.4.1 Comparison with previous Hf and W isotope data for leaching fractions

A major difference between sequential leaching experiments and bulk rock analyses is that leaching experiments allow identification of isotopically anomalous meteorite components even if the bulk meteorite does not display isotope anomalies. In this regard, our data for the major Hf and W isotopes are consistent with the results of Qin et al. (2011), in that first leachates generally tend to show deficits in ε^{178}Hf and ε^{180}Hf, whereas the residues (or subsequent leaching steps) usually show excesses in these isotopes. The same observation is made for ε^{174}Hf which was analyzed for the first time in our study. Leachates 1 show negative ε^{174}Hf, whereas the residues show positive ε^{174}Hf. In addition to this qualitative agreement, also the relative magnitude of coupled anomalies in ε^{178}Hf and ε^{180}Hf found by Qin et al. (2011) corresponds to those reported in this study, with Qin et al.'s data defining a slope of 0.91±0.17 and our data defining a slope of 0.87±0.05 in ε^{178}Hf vs. ε^{180}Hf space.

In our W isotope dataset, the first leachate steps typically show elevated ε^{180}W and ε^{183}W. In contrast, second leachates and especially residues tend to show depletions in ε^{180}W and ε^{183}W. Our ε^{183}W data agree well with those of Burkhardt and Schönbächler (2015), who also found positive ε^{183}W generllay in the first leaching steps and generally negative ε^{183}W in later leaching steps. A regression through the data of Burkhardt and Schönbächler (2015) yields a slope of 1.41±0.05 (^{182}W vs ^{183}W) with an ^{182}W intercept of 2.29±0.47. These results agree with our results that define a slope of 1.37±0.24 and a ε^{182}W intercept of -1.81±0.23.

The consistency of Hf and W results for the major isotopes between our and previous studies implies that the slightly different leaching protocols applied lead to a broadly similar

selective dissolution of carrier phases. Our calculated whole rock isotope compositions from mass balance considerations (Table 1) are in good agreement with previous results for bulk rocks (e.g., Kleine et al. 2004; Bouvier et al. 2008; Sprung et al. 2010, Akram et al. 2013; Peters et al. 2014; Peters et al. 2016), indicating that all anomalous carrier phases have been sampled and that nearly complete sample dissolution has been achieved in our leaching experiments.

II.4.2 Cosmogenic effects

Several studies have shown that the stable isotope compositions of meteorites can be affected by secondary neutron capture effects (e.g., Eugster et al., 1970). These effects can significantly shift the pristine isotope compositions and lead to misinterpretations if not recognized as secondary effects. Significant neutron capture has been reported for several elements, e.g., Sm and Gd (Eugster et al., 1970; Lugmair and Marti, 1971; Russ III et al., 1971; Hidaka et al. 2000), but also including Hf and W, especially for meteorites with high exposure ages (e.g., Sprung et al. 2010; Kruijer et al. 2013).

The majority of our samples are chondrites that have low exposure ages of less than 120 Ma (Eugster, 2003) and, thus, they are assumed to show only insignificant cosmic ray effects. In addition, we compare our data to the model developed for neutron capture of Hf by Sprung et al. (2010) to evaluate if our ε^{174}Hf, ε^{178}Hf, and ε^{180}Hf data are compromised by neutron capture effects. Neutron capture causes particularly significant burn-out of ^{177}Hf and ^{178}Hf leading to a distinct negative slope in ε^{178}Hf vs. ε^{180}Hf space that is approximately perpendicular to the coupled offset in both isotope signatures that would relate to s- or r-process Hf isotope anomalies (Sprung et al., 2010; Figure 4). However, all samples except El Hammami (H5) plot within uncertainty along a regression line with a positive slope of 0.87±0.05. The MSWD is 4.3, indicating that the observed samples are insignificantly affected by neutron capture. In contrast, El Hammami is showing negatively correlated ε^{180}Hf and ε^{178}Hf signatures, resulting in an offset from the regression line that is fully compatible with the predicted neutron capture line of Sprung et al. (2010; 2013). Note that Sprung et al. (2010) lacked the resolution to clearly identify neutron capture induced Hf isotope shifts in El Hammami, but their data are compatible with our new observations at improved precision. Our data are furthermore in agreement with Peters et al. (2016) who showed that minor

cosmogenic shifts in ε^{180}Hf and ε^{178}Hf are present in some chondrites. These considerations demonstrate that neutron capture effects are easily identified and recognized using Hf isotope analyses and that only one of our samples, El Hammami, is significantly affected by secondary neutron capture reactions.

Importantly, Hf isotopes can also be used to evaluate neutron capture effects on W isotopes because Hf and the relevant Ta (^{181}Ta (n,γ) ^{182}Ta (β^-, $e^- + \nu_e$) ^{182}W) and W isotopes are most sensitive to neutron capture at the same, epithermal neutron energy (e.g. https://www-nds.iaea.org/exfor/endf.htm; Kruijer et al., 2015). Since no sample except El Hammami is showing resolvable neutron capture effects in Hf isotopes, similar effect can be regarded insignificant for all W isotope ratios as well. El Hammami shows no resolvable variation in ε^{183}W, and its ε^{182}W of -2.34±0.10 is indistinguishable from the ^{182}W composition of other H chondrites (Kleine et al. 2007). Possibly, the small positive ε^{180}W anomaly (1.54±0.91) of El Hammami might be the result of ^{184}Os-decay to ^{180}W (Peters et al., 2014).

For Indarch and Tafassasset leachate 2, Hf isotope ratios were not obtained due to the low concentrations of Hf in the respective fractions, thus Hf isotope data are not available for the evaluation of neutron capture effects. Nonetheless, for those fractions neutron capture effects can likely be neglected, because neither meteorite has previously been reported to possess differently pre-irradiated constituents (Yokoyama et al. 2011; Breton et al. 2015).

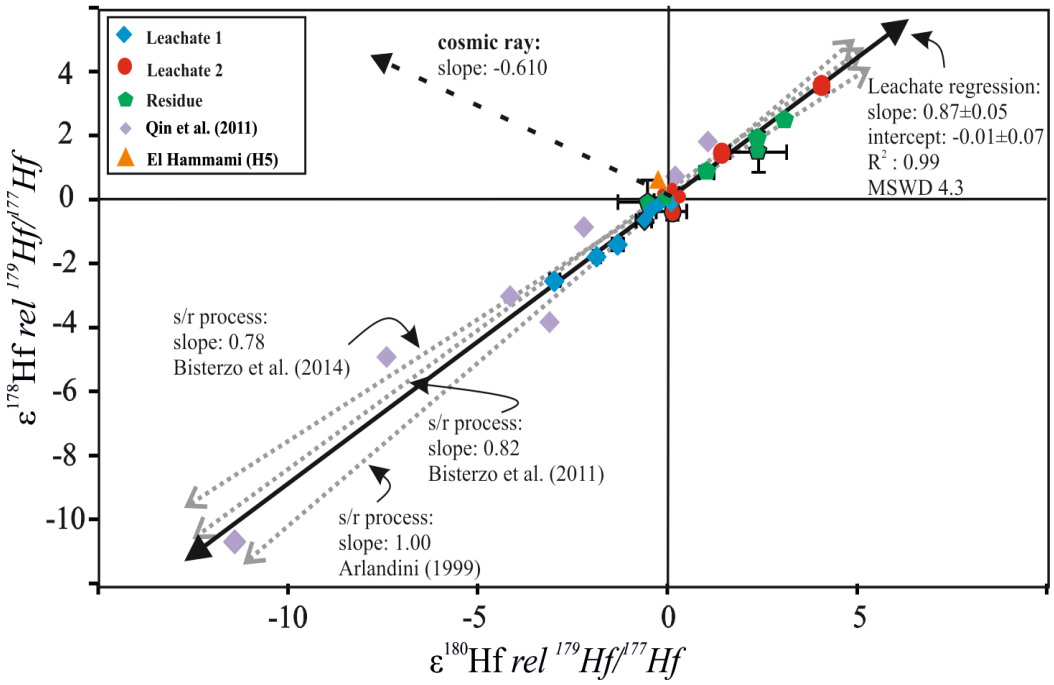

Figure 4: Plot of ε^{178}Hf vs. ε^{180}Hf data normalized to ^{179}Hf/^{177}Hf for the sequentially leached meteorite samples of this study and Qin et al. (2011) compared with stellar models of Arlandini et al. (1999), Bisterzo et al. (2011) and Bisterzo et al. (2014) (stippled grey lines) and the cosmogenic neutron capture trend line of Sprung et al. (2010). All samples follow s/r-process variations, except El Hammami bulk rock (H5) (orange triangle). El Hammami is affected by cosmogenic effects showing coupled deficits in ε^{180}Hf and enrichments in ε^{178}Hf. Inferred data of MET 01070 residue, Kainsaz residue, Leoville leachate 1 and EET 96026 leachate 2 are shown (black edges) but not included for calculation of the regression using IsoPlot 4.13.

II.4.3 Nucleosynthetic isotope variations

As discussed above, Hf and W isotopes are well suited for discriminating between s- and r, and p-process variations in meteoritic materials. Available astrophysical production models predict slightly different contributions of the s- and r-process to the Hf and W isotope inventories. Suggested s-process contributions to the Hf isotope inventory vary between 53 and 61%, depending on which stellar model is used for calculations of the s-process production rates (Arlandini et al., 1999, Bisterzo et al., 2011; Bisterzo et al., 2014). In the same studies, s-process contribution estimates range from 56 to 65 % for W. Note that slight adjustments to published r-residuals are required for modeling because of the common use of now revised 'natural terrestrial' isotope compositions in the astrophysical literature, i.e., the use of terrestrial isotope compositions from Anders & Grevesse (1989) rather than the more recent recommended estimates of terrestrial isotope compositions by the IUPAC (Berglund & Wieser, 2011) or those commonly used in geo- and cosmochemistry (e.g., Völkening et al. 1991; Vervoort & Blichert-Toft, 1999).

II.4.3.1 Hafnium isotopes

Hafnium isotope signatures are strongly correlated with a slope of 0.87±0.05 in ε^{178}Hf vs. ε^{180}Hf space (normalized to ^{179}Hf/^{177}Hf) and an MSWD of 4.3 (Fig. 4). Modelled slopes for s- or r-process induced isotope anomalies range from +1.00 (Arlandini et al. 1999), over +0.82 (Bisterzo et al. 2011), to +0.78 (Bisterzo et al., 2014) (Fig. 4). We thus conclude that the observed Hf isotope variations result from variable contributions of s- or r-process carrier phase(s) to the different leachates and residues. However, to distinguish whether the variations in leachates and residues result from acid resistant s-process carrier phases or from the preferential dissolution of r-process carrier phases, it is pivotal to consider the p-process isotope ^{174}Hf. When combined, our ε^{174}Hf and ε^{180}Hf data (relative to ^{179}Hf/^{177}Hf) define a slope of 0.65±0.18 with an MSWD of 1.2 (Fig. 5a). According to different models for stellar nucleosynthesis, variation in s-process contributions are predicted to produce slopes of +0.32 (Arlandini et al., 1999), +0.53 (Bisterzo et al. (2011) and +0.52 (Bisterzo et al. 2014). The slopes predicted for variable r-process contributions would be +3.71 (Arlandini et al., 1999), +3.30 (Bisterzo et al. 2011) and +3.27 (Bisterzo et al. 2014). Hence, our data clearly show that the contributions from s-process nuclide carriers are variable, whereas the proportion between p- and r-process components remained constant.

Applying the ^{180}Hf/^{177}Hf normalization scheme, ε^{174}Hf and ε^{179}Hf define a slope of -0.92±0.15 with an MSWD of 1.2 (Figure 5b). Note, that the difference in s-process contribution to ^{180}Hf and ^{177}Hf (~88% vs ~17%, respectively) is much more than for ^{179}Hf and ^{177}Hf (~40% vs. ~18%, respectively) that are commonly used for normalization. Thus, correlated ^{174}Hf-^{179}Hf anomalies within the ^{180}Hf/^{177}Hf normalization scheme provide a more sensitive test for potential s-or r-process variations than data from the classical ^{179}Hf/^{177}Hf normalization scheme. When normalizing to ^{180}Hf/^{177}Hf, variable s-process contributions yield a slope of about -0.99 (Bisterzo et al. 2014) to -0.51 (Arlandini et al., 1999). In contrast, variable contributions from r-process Hf would produce a slope from -3.47 (Bisterzo et al. 2014) to -3.06 (Arlandini et al., 1999). Again, this approach reveals variable contributions of s-process carriers to the Hf inventory of our different leachates and residues with r- and p-process carrier phases being of minor importance. Alternatively, the observed variations could have been caused by coupled r- and p-process carrier varaitions. However, this appears to be unlikely since (i) r- and p-process carrier must have been dissolved within always the same proportions during leaching which appears to be unlikely and (ii) r- and p-process carrier phases appear to be very rare (Savina et al. 2004).

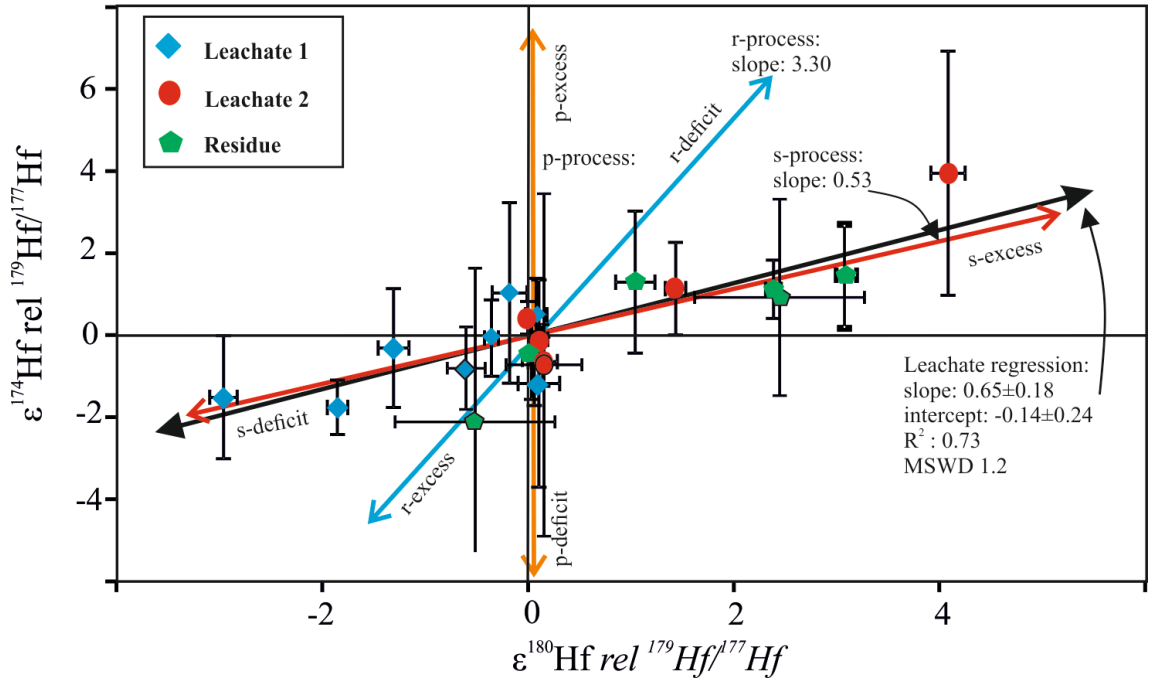

Figure 5 a: Plot of ε^{174}Hf vs. ε^{180}Hf normalized to ^{179}Hf/^{177}Hf for sequentially leached meteorite samples compared with the stellar model of Bisterzo et al. (2011). Variations are clearly controlled by an s-process component. Inferred data of MET 01070 residue, Kainsaz residue, Leoville leachate 1 and EET 96026 leachate 2 are shown but not included for calculation of the regression by using IsoPlot 4.13.

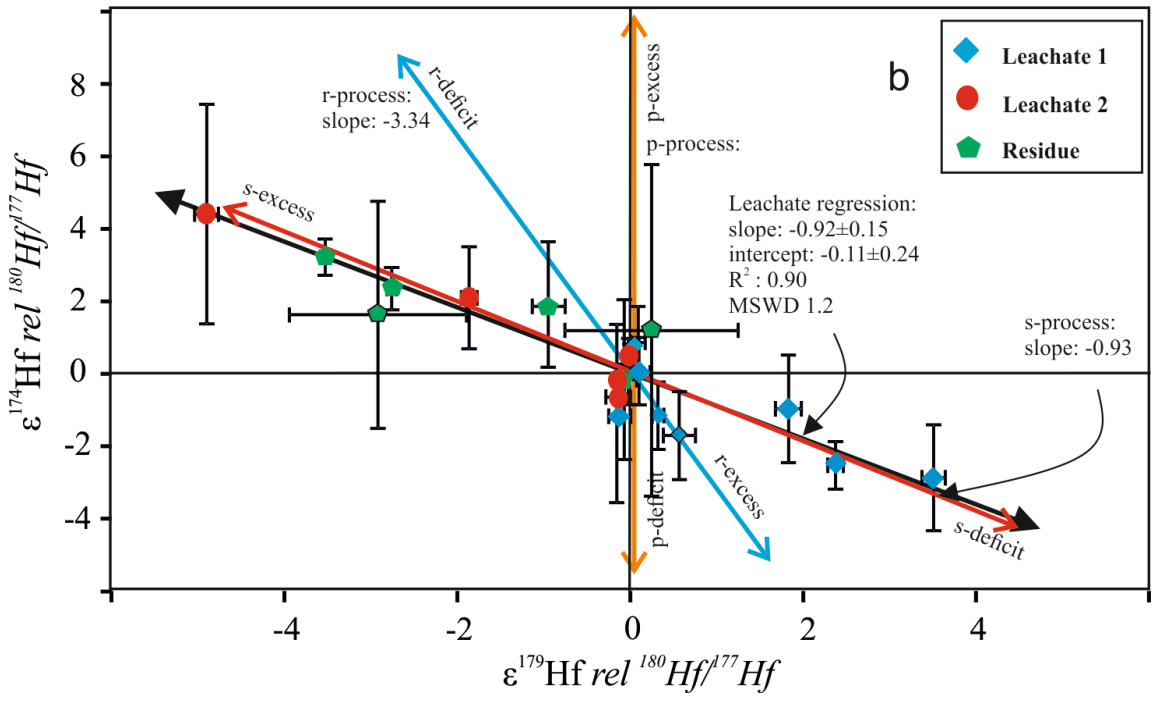

Figure 5 b: Plot of ε^{174}Hf vs. ε^{180}Hf normalized to ^{179}Hf/^{177}Hf for sequentially leached meteorite samples compared with the stellar model of Bisterzo et al. (2011). Variations are clearly controlled by an s-process component. Inferred data of MET 01070 residue, Kainsaz residue, Leoville leachate 1 and EET 96026 leachate 2 are shown but not included for calculation of the regression by using IsoPlot 4.13.

II.4.3.2 Tungsten isotopes

As described above, the W isotope data of our different leachates and residues also exhibit a strong linear co-variation. In $\varepsilon^{182}W$ vs. $\varepsilon^{183}W$ space our data define a slope of 1.37±0.24 (MSWD = 17) with an intercept at $\varepsilon^{182}W = -1.81\pm0.23$ (Fig. 6). The high MSWD most likely results from scatter introduced by in-situ decay of ^{182}Hf at variable Hf/W of phases that were dissolved in different leaching steps. To quantify the exact contribution of radiogenic ^{182}W in the presence of nucleosynthetic anomalies is far from being trivial. Sequential leaching might lead to Hf/W fractionation because of incongruent dissolution or selective precipitation, primarily of Hf (e.g., Blichert-Toft, 2001). Thus, measured Hf/W of leachates or residues might be erroneous. It is the time-integrated Hf/W, however, that is the factor controlling radiogenic $\varepsilon^{182}W$. As a consequence, reliable corrections for in-situ ^{182}Hf decay of leachates are missing. Likewise, Burkhardt et al. (2012b) attempted to correct for radiogenic ^{182}W contributions, but ended up using the uncorrected regression line as a best fit. Notably, our regression line with a slope of 1.37±0.24 agrees well with the theoretical s- or r-process variation slope of 1.48 predicted by the model of Bisterzo et al. (2014), as well as with the empirical slope of 1.41±0.05 deduced by Burkhardt and Schönbächler (2015). We therefore conclude that the observed slope in $\varepsilon^{182}W$ vs $\varepsilon^{183}W$ space is primarily controlled by s- or r-process variations and that scatter introduced by ^{182}Hf decay is only minor.

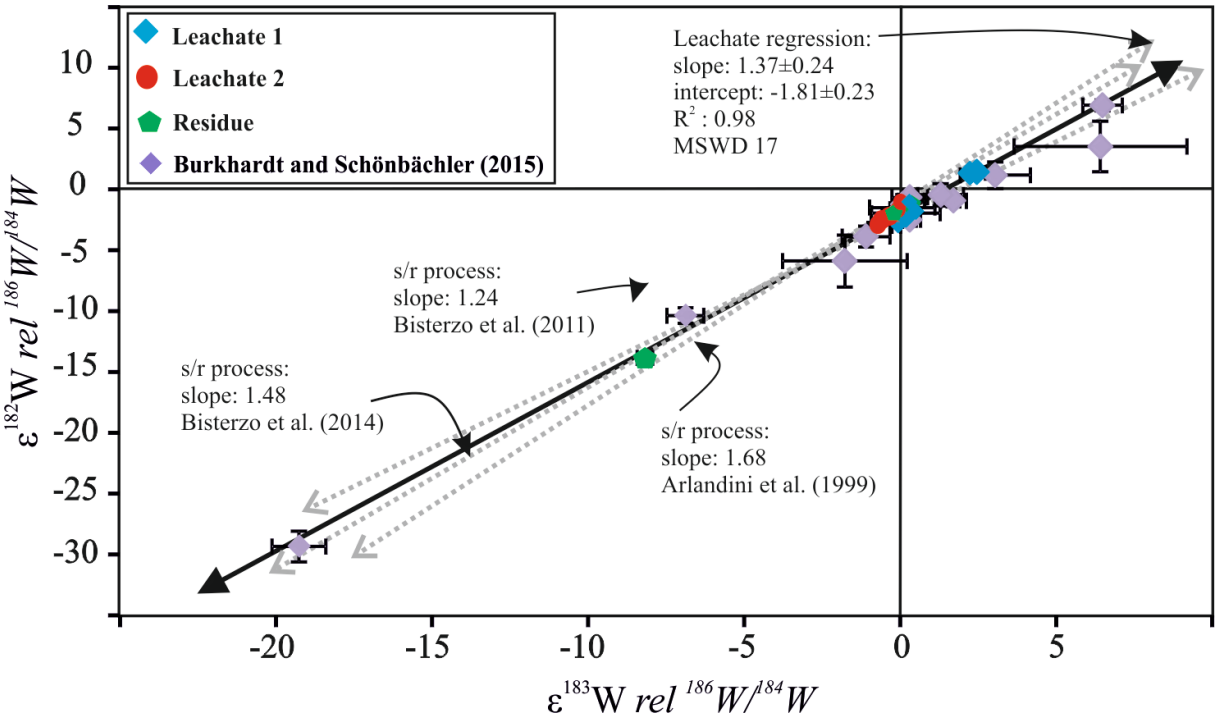

Figure 6: Plot of $\varepsilon^{182}W$ vs. $\varepsilon^{183}W$ data normalized to $^{186}W/^{184}W$ for the sequentially leached meteorite samples of this study and from Burkhardt and Schönbächler (2015), together with trends for stellar models of Arlandini et al. (1999), Bisterzo et al. (2011) and Bisterzo et al. (2014) (stippled grey lines). Samples only follow s/r-process variations. Inferred data of MET 01070 residue, Kainsaz residue, Indarch residue and Tafassasset residue are not included. The regression line is calculated by using IsoPlot 4.13.

To discriminate between s- or r-process contributions in our dataset, ^{180}W data are required. Tungsten-180 is an almost pure p-process isotope with a minor s-process contribution between 4.5 and 5.1% (Arlandini et al. 1999; Bisterzo et al. 2011; Bisterzo et al. 2014). Our ^{180}W data form distinct slopes of 3.82±0.50 and -2.62±0.74 in $\varepsilon^{180}W$ vs. $\varepsilon^{183}W$ and $\varepsilon^{180}W$ vs. $\varepsilon^{184}W$ space, respectively (Fig. 7 a, b). This is in agreement with variable contributions of s-process W after Bisterzo et al. (2014), yielding slopes of 4.25 and -3.35, respectively. In contrast, and inconsistent with our data, r-process contribution variations would yield slopes of 1.51 and 0.76 in $\varepsilon^{180}W$ vs. $\varepsilon^{183}W$ and $\varepsilon^{180}W$ vs. ^{184}W space, respectively.

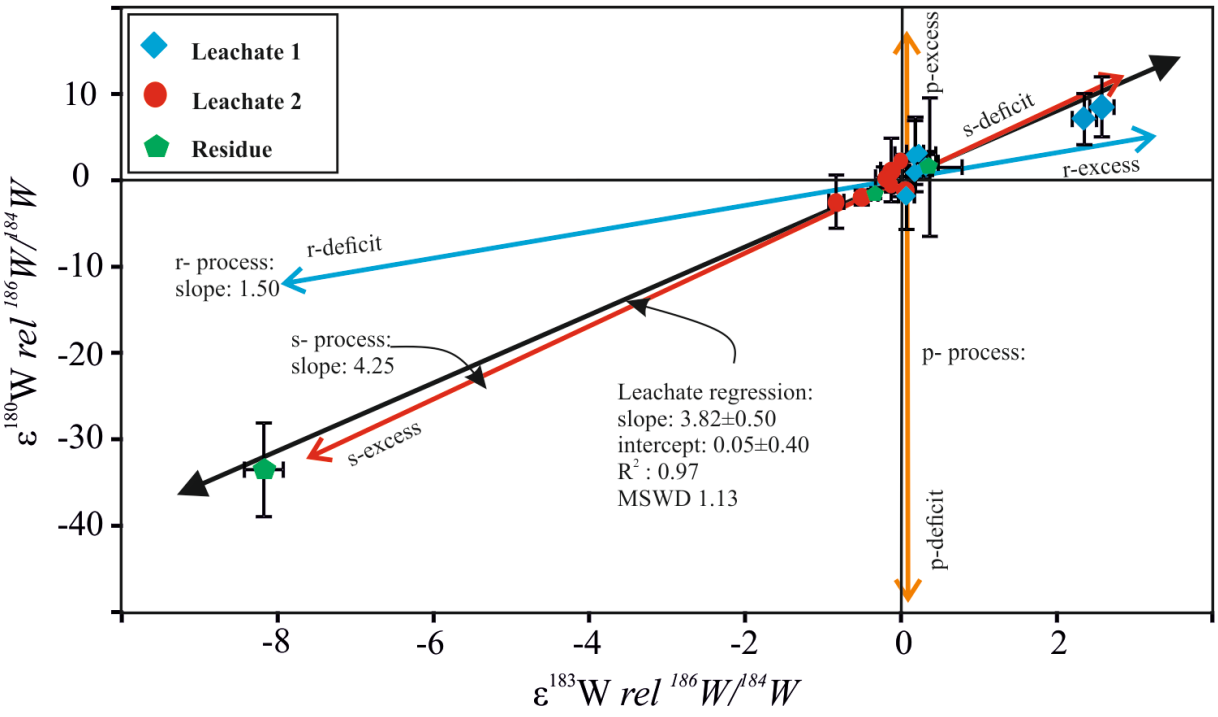

Figure 7 a: $\varepsilon^{180}W$ vs. $\varepsilon^{183}W$ normalized to $^{186}W/^{184}W$ data for the sequentially leached meteorite samples compared with the stellar model of Bisterzo et al. (2014). Variations can be best described by variability of s-process components. Inferred data of MET 01070 residue, Kainsaz residue, Indarch residue and Tafassasset residue are not included. The regression line is calculated by using IsoPlot 4.13.

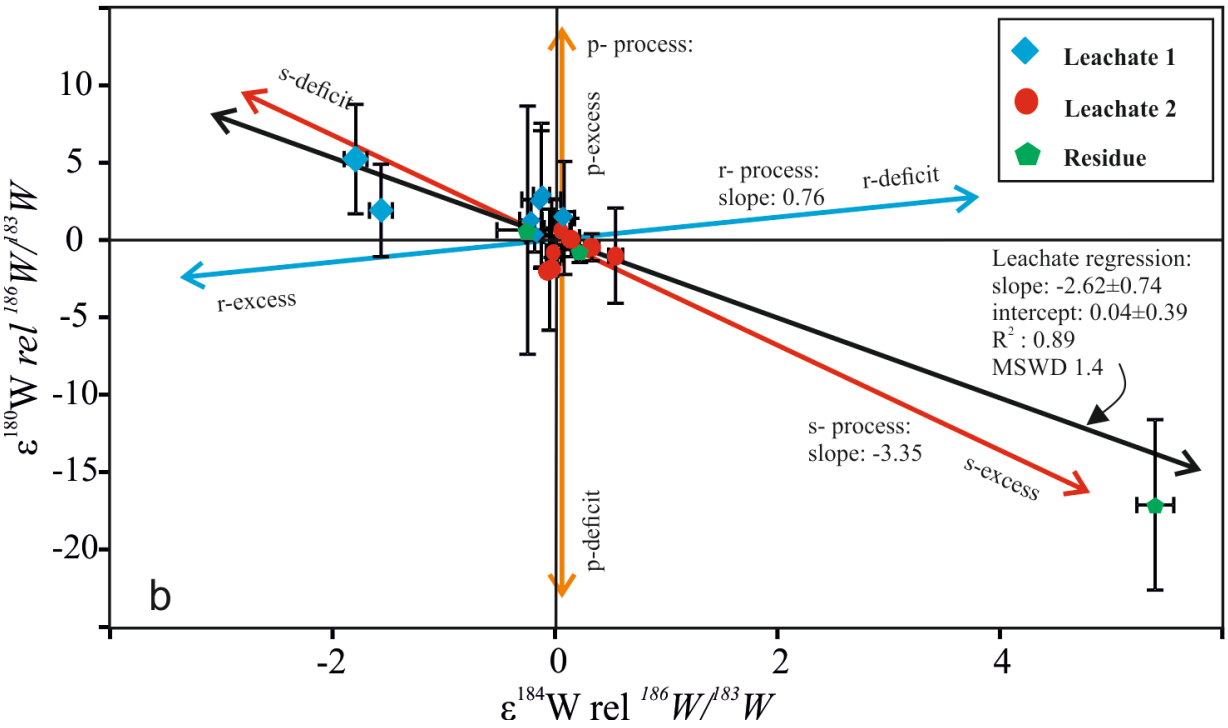

Figure 7 b: $\varepsilon^{180}W$ vs. $\varepsilon^{184}W$ normalized to $^{186}W/^{183}W$ data for the sequentially leached meteorite samples compared with the stellar model of Bisterzo et al. (2014). Variations can be best described by variability of s-process components. Inferred data of MET 01070 residue, Kainsaz residue, Indarch residue and Tafassasset residue are not included. The regression line is calculated by using IsoPlot 4.13.

Similar to the case made for ^{182}W, radiogenic ^{180}W from the very long-lived decay of ^{184}Os has to be considered for the interpretation of $\varepsilon^{180}W$ vs. $\varepsilon^{183}W$ and $\varepsilon^{180}W$ vs. $\varepsilon^{184}W$ relationships (Peters et al. 2014). Potential high Os/W phases in chondrites are ultra-refractory metal grains as described by Berg et al. (2009). Such metal has Os/W of up to 13 and would have accumulated an radiogenic ingrowth in ^{180}W of around 6 ε-units since the formation of the solar system. Most probably, however, such acid resistant metal grains will remain in the residue associated with SiC (Berg et al., 2009). Consequently, even if significant for the total W budget of the meteorite, radiogenic ingrowth from ^{184}Os decay in ultra-refractory metal grains would always create slopes that are shallower than those predicted by the astrophysical models. The good agreement of our well-defined correlation lines with the astrophysically predicted slopes leads us to the conclusion that ^{184}Os decay can be regarded negligible at the given analytical uncertainty. Collectively, the observed correlated anomalies of W isotopes between different leachates and residues can clearly be assigned to enrichments and depletions in s-nuclide W carrier phases while r- or p-process carrier phases were of minor abundance.

II.4.4 Constraints on s-process carrier phases

Qin et al. (2011) and Burkhardt and Schönbächler (2015) suggested that the observed variation among Hf and W isotopes in fractions of meteorites produced by sequential leaching is due to variable proportions of s- and r-process carriers in the different fractions. By additionally using ^{174}Hf and ^{180}W, our data document for the first time the lack of variations in p- or r-process contributions to the Hf and W isotope inventory (at our current analytical resolution). Rather, all isotope anomalies in leachates and residues can be accounted for by variable contributions from s-process carriers. Burkhardt and Schönbächler, (2015) identified s-process enriched mainstream SiC as one putative s-process carrier phase since the W isotope compositions of mainstream SiC grains plot within uncertainty of the regression within their $\varepsilon^{182}W$ vs $\varepsilon^{183}W$ space. This observation is supported by the data obtained in this study (Fig. 8). Moreover, based on mass balance calculations Burkhardt and Schönbächler (2015) showed that mainstream SiC seems to be the dominant refractory phase for Murchison, whereas the abundance of mainstream SiC is too low to explain s-process anomalies for Allende, even if a 50 times solar W abundance enrichment is considered for mainstream SiC.

However, a more valid assumption would be probably < 10 times the solar W/Si ratio (Ávila et al. 2012). Our own mass balance calculations, using the bulk chondrite abundance of presolar SiC from Huss et al. (2003) (Murchison = 13.5ppm, Kainsaz = 0.06ppm, Allende = 0.01ppm and a mainstream SiC fraction of 90% of the total SiC (e.g., Hynes and Gyngard, 2009), confirms the suggestion of Burkhardt and Schönbächler (2015). The anomalies for Murchison can be well explained by the presence of mainstream SiC with a W/Si enrichment factor of only 7.8, while Kainsaz and especially Allende would require unreasonable high W/Si enrichment factors in SiC of 80 or more, also if it is assumed that all SiC grains are s-process enriched instead of mainstream grains only. Certainly, better data for W abundances in SiC and better estimates for SiC abundances in Kainsaz and Allende are required, but it appears most likely that in Allende and Kainsaz refractory s-process W bearing phases other than mainstream SiC are significant, while for Murchison mainstream SiC may well be a significant if not the dominant s-process W carrier. To explain the W isotope anomalies in Murchison entirely by mainstream SiC, about 55% s-process W from mainstream SiC is required in leachate 2 with the remaining 45% mainstream SiC in the residue. This distribution could in part be controlled by grain size effects, with small mainstream SiC grains being preferentially dissolved in leachate 2 while the interiors of larger grains were finally attacked during digestion of the residue. Alternatively, we may deal with two significant s-process W bearing phases with the less chemically resistant phase being dissolved in leachates 2 and the other in the residue of Murchison (and MET 01070).

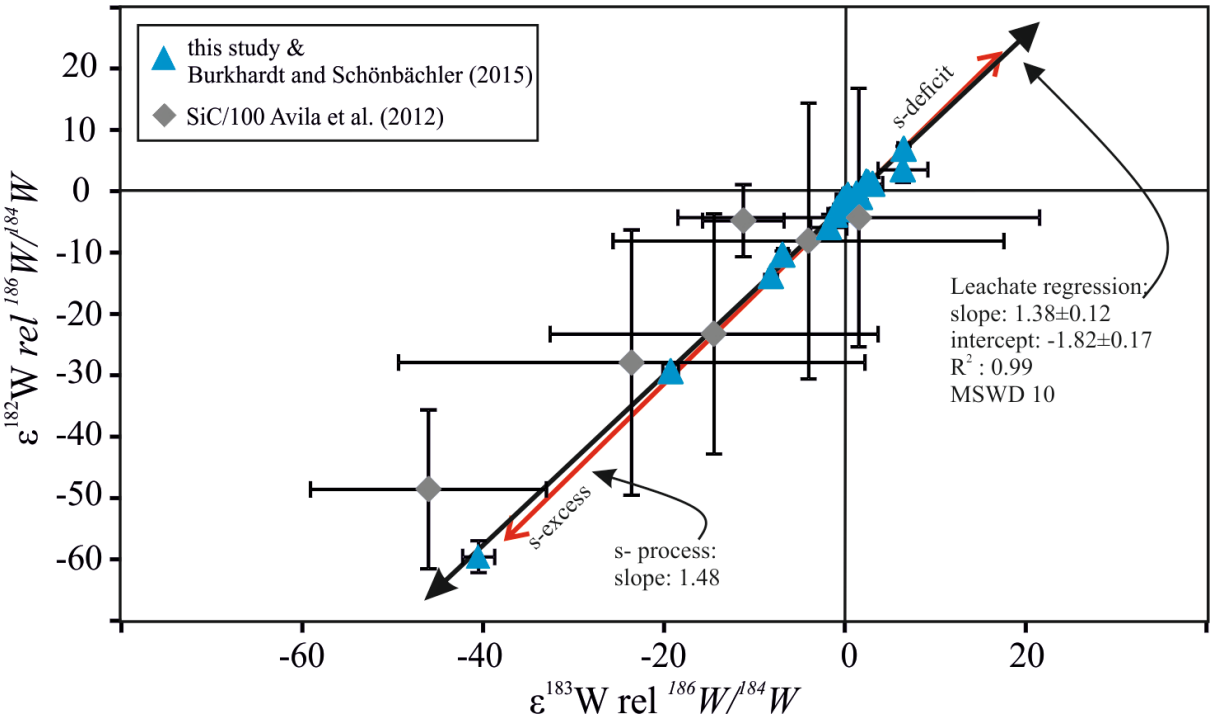

Figure 8: $\varepsilon^{182}W$ vs. $\varepsilon^{183}W$ data normalized to $^{186}W/^{184}W$ for the sequentially leached meteorite samples of this study and Burkhardt and Schönbächler (2015) and in-situ data, divided by 100, for SiC by Avila et al. (2012). The W isotope data are consistent with the presence or absence of s-process SiC grains. The red line represents the s-process variation line (Bisterzo et al. (2014). Inferred data of MET 01070 residue, Kainsaz residue, Indarch residue and Tafassasset residue are not included. The regression line is calculated by using IsoPlot 4.13.

Different carrier phases for s-process Hf and W are evident by the data from leachates 1 of Murchison, Kainsaz and MET 01070. These leachates all contain comparable amounts of total Hf released (40 - 55%) and all show significant Hf isotope variations ($\varepsilon^{180}Hf \sim -3$ to -1.3) with Kainsaz leachate 1 showing the most significant Hf isotope variation ($\varepsilon^{180}Hf \sim -3$). All these leachates also contain comparable amounts of total released W (44 – 48%), however leachate 1 from Kainsaz shows $\varepsilon^{183}W$ of 0.33, which is ~8 times smaller than that of Murchison leachate 1 (~2.6). This discrepancy constrains that the s-process W phase(s) equilibrated isotopically more efficiently with the surrounding material in the Kainsaz parent body than the s-process Hf phase(s). Moreover, the selective enrichment of s-process Hf in leachates 2 of MET 01070 and Kainsaz gives further evidence for different carrier phases for s-process Hf and W. The use of stronger HF obviously led to the selective release of s-process Hf in CM chondrite MET 01070 and CO chondrite Kainsaz, whereas no simultaneously increased s-process W release was observed. In addition, by combining mass balance calculations for Hf and W using Hf/W ratios of ~0.22 for SiC (Avila et al., 2012), we can also clearly rule out that mainstream SiC is the main s-process Hf bearing phase since the total amount of s-

process Hf nuclides carried by mainstream SiC is too low to simultaneously cause the observed s-process Hf and W enrichments within any meteorite analyzed in this study. Notably, this also applies for Murchison, where mainstream SiC seems to be the dominant s-process W bearing phase.

Moreover, the enrichment of the s-process Hf carrier phase(s) in leachates 2 from the more aggressively attacked MET 01070 and Kainsaz also implies that the s-process Hf carrier phase(s) are probably more susceptible to HF. This might argue for a presolar silicate or oxide Hf carrier. Hydrofluoric acid is often used to attack the silica bonding of silicates and to complex the metals of oxides (e.g., Potts, 1992). Presolar silicates and oxides can be quite abundant in carbonaceous chondrites. They can reach concentrations up to ~200 ppm (Vollmer et al., 2009; Davidson et al. 2010; Floss and Stadermann, 2012; Nittler et al 2013; Davidson et al. 2015; Leitner et al. 2013; Leitner et al. 2016). However, since most presolar grains occur in the inter-chondrule matrices of meteorites (Leitner et al., 2016), the overall abundance of presolar grains decreases rapidly with increasing degree of aqueous or thermal parent body processing. Aqueous alteration induces the formation of crystalline phyllosilicates whereas thermal alteration on the parent body causes matrix recrystallization. Especially silicates are very susceptible to this parent body processing (Nagashima et al. 2005; Leitner et al., 2016). Within the chondrites analyzed in this study, Kainsaz is the most primitive meteorite (petrologic type 3.2; Grossman and Brearley, 2005). However, Kainsaz is also reported to show the lowest matrix abundance (30%; McSween, 1977b). In contrast, MET 01070 and Murchison show the highest matrix abundance (~60%), but experienced aqueous alteration (McSween, 1979; Rubin et al., 2007). Allende probably experienced the highest thermal alteration (Bonal et al., 2006) among the carbonaceous chondrites in this study and shows a matrix abundance of 38% (McSween, 1977a). It is also noteworthy that the CV chondrite Leoville is slightly less thermally altered than Allende (Bonal et al., 2006), but shows a significantly smaller magnitude of Hf isotope variation, while having comparable abundances of matrices (35% vs. 38%, McSween, 1977a). This is most probably the result of dilution effects, since the residue of Allende contained only 5% of total Hf whereas the residue of Leoville contained 19% of the total Hf released. Thus, based on the matrix abundances, the degree of parent body alteration and the assumption that presolar silicates and/or oxides carry significant abundances of s-process Hf, the observation that CV

chondrites display the smallest, and CM and CO similarly magnitudes of s-process Hf variations appears well plausible.

In summary, the isotope anomalies in our leachates and residues result from diverse s-process carrier phases. S-process W seems to be dominated by mainstream SiC at least in Murchison whereas other refractory s-process W carrier phases must dominate the much smaller amount of W in the acid resistant fractions of Kainsaz and Allende. Hafnium isotope anomalies are due to carrier phases different to those responsible for the W isotopes anomalies, and are most likely dominated by silicates and/or oxides.

II.4.5 Implications for the early solar system: Parent body versus nebular processing

It is commonly accepted that aqueous alteration and thermal metamorphism took place on meteorite parent bodies (e.g., DuFresne and Anders, 1962; Van Schmus and Wood, 1967). Both processes can selectively diminish the abundances of presolar phases as carriers of isotope anomalies, due to their selective breakdown or equilibration. Equilibration of isotope anomalies may be the consequence of different temperature resistivity, grain sizes of presolar phases, different water solubility or changes in oxygen fugacity. Among the chondrites analyzed in this study, MET 01070 and Murchison show the strongest overprint by aqueous alteration, whereas the CV chondrite Allende is the most thermally altered carbonaceous chondrite in our suite. In contrast to the CM chondrites and the CV chondrites analyzed, Kainsaz is of petrologic type 3.2 and thus appears to contain the least altered matrix compared to Allende MET 01070 and Murchison. The matrix abundance of Kainsaz is ~30%, in CM chondrites it is around ~60% and the matrix abundance of Allende is ~38%. Therefore, it appears possible that the CO chondrite Kainsaz with its comparatively pristine matrix and the aqueously altered CM chondrites show similarly magnitude of isotope variations whereas the slightly metamorphosed CV chondrite Allende displays smaller variations as indeed observed for Hf isotopes. However, the magnitudes of W isotope anomalies are different from those for Hf isotopes, decreasing in the order CM>>Kainsaz> Allende. Thus, it seems that only a small fraction of the initially dominant s-process W carrier phase(s) survived thermal parent body processing in Kainsaz and Allende, while such phases were only little affected by aqueous alteration. Huss et al. (2003) suggested, that besides parent body processes, also intra-nebula processes can alter the inventory of presolar phases. Later studies such as Trinquier et al.

(2009), Burkhardt et al. (2012a), or Akram et al. (2015) ascribed significant bulk rock isotope anomalies for Ti, Mo, and Zr to nebular thermal processing. Moreover, Ebel and Grossman (2000) have shown that the evaporation of chondritic dust can also significantly raise fO_2, and Mendybaev et al. (2002), in turn, demonstrated that the absolute mass loss rate of SiC strongly depends on the fO_2. An oxidation event would probably not have affected presolar oxides/silicates abundances as significant as those of SiC, thus leading to decreasing ratios of SiC-to-silicates/oxides. Thus, by taking into account that CV and CO chondrites are interpreted to have experienced more pronounced intra-nebular processing (e.g., Huss et al. 2003; and Huss, 2004), a scenario including evaporation of solar nebula material accompanied by rising fO_2 can potentially explain why the Hf and W anomalies seem to be decoupled in some chondrite samples. This pre-accretionary processing of Kainsaz and Allende material possibly also involved elemental redistribution from mainstream SiC into other and/or new phases and, thus, may also provide an explanation why mainstream SiC seems to be the dominant s-process W bearing phase in Murchison but not in Kainsaz and Allende. Alternatively, the decoupling of Hf and W anomalies and SiC breakdown in Kainsaz and Allende may have been established during parent body processing. Davidson et al (2014) speculated, that parent body processing even at only slightly elevated temperatures accompanied by prolonged oxidation may lead to the formation of thermodynamically unstable SiO_2 on the outer layers of SiC grains, which then may lead to the progressive destruction of SiC. Taking into account that Allende and Kainsaz have experienced higher degrees of thermal alteration than Murchison and also show evidences oxidation (e.g., Krot et al. 1995; Choi et al. 1997; Keller and Buseck, 1990; Imae and Kojima, 2000), SiC may have indeed to a higher fraction been destroyed in Allende and Kainsaz than in Murchison. This scenario may also have involved elemental redistribution from SiC into other phases as well.

Selective intra-nebular processing of solar nebula material can also in principle explain the homogeneity of r- and p-process Hf and W in our chondrite leachates and residues that is independent of petrologic type or matrix abundance. Such models need to assume that the majority of Hf and W r- and p-process carrier phases are thermally and/or thermodynamically less resistant than their s-process counterparts. By taking into account that the carriers of r and p-process nuclides originated in the ejecta of highly energetic i.e., neutron star mergers or a massive star goes supernovae, they have been most probably also in highly amorphous state (Kemper et al. 2004), thus recrystallizing easier during thermal processing within the early

solar system than their crystalline counterparts (e.g., Gail, 2004; Harker and Desch, 2002). Therefore, selective intra-nebular processing can potentially account for the observed homogeneity of r- and p-process phases. However, by assuming that r- and p-process phases are highly amorphous and less refractory than their s-process counterparts, r- and p-process phases are also very likely be highly susceptible to parent body processing. Thus, it remains unclear to which extents intra-nebular processing or parent body processing homogenized r- and p-process carrier phases. Additionally, r- and p-process carriers may have equilibrated isotopically within the parental molecular cloud core, but this scenario is not compatible with the p-process isotope anomalies that have been found in CAIs (Peters et al., 2016), implicating that p- and possibly r-process carrier phases were not equilibrated shortly after cloud collapse.

Thus, based on the observations described above we conclude that the isotope patterns of Hf and W in the analyzed chondrite samples may represent the fingerprint of parent body processing, intra-nebular processes or a combination of both.

II.5 Conclusions

Our study presents high precision Hf and W isotope data for leachates and residues of chondrite samples, including, for the first time, the rare p-process nuclides ^{174}Hf and ^{180}W. Whereas there is no evidence for isotope anomalies at the bulk rock scale, nucleosynthetic isotope anomalies of, e.g., a few ε^{179}Hf (if normalized to ^{180}Hf/^{177}Hf) are identified in the carbonaceous chondrites MET 01070 (CM1), Murchison (CM2), Allende (CV3) and Kainsaz (CO3). In contrast, ε^{183}W (normalized to ^{186}W/^{184}W) displays such large anomalies only in the CM chondrites. The additional information provided by the p-process isotopes ^{174}Hf and ^{180}W unambiguously reveals variable contributions of acid resistant presolar s-process carrier phases to be responsible for the observed isotope anomalies, whereas contributions from r- and p-process Hf and W isotopes appear to be uniform in all leachates and residues within analytical resolution. Hence, no distinct r- or p-process carriers can be constrained.

Notably, correlated Hf and W isotope anomalies have been found in CM chondrites whereas in CO and CV chondrites only significant Hf anomalies have been found. This pattern requires distinct s-process W and Hf carrier phases. Whereas s-process enriched W in CM chondrites residues mainly resides in mainstream SiC, residues of Kainsaz and Allende must be dominated by other refractory carrier phases. S-process enriched Hf is carried by

dominantly different presolar phases than mainstream SiC, possibly by silicates or oxide phases. In contrast, the bulk of r- and p-process Hf and W nuclides were likely initially carried by less stable, possibly highly amorphous phases that recrystallized during thermal nebular and/or parent body processing. The different magnitudes of isotope variations in leachates and residues results from the partial survival of the different s-process carrier phases, that were affected to different degrees by thermal and aqueous alteration on the parent bodies and possibly by additional nebular processing. Parent body processing is furthermore evident from the lack of nucleosynthetic isotope variation amongst leachates and residues of meteorites of higher petrologic type (Indarch EH4, EET 96026 C4/5; primitive achondrite Tafassasset).

The observation that the non-radiogenic Hf and W isotope abundances of bulk meteorite samples do not deviate from the terrestrial ratios (this study, Burkhardt & Schönbächler, 2015; Sprung et al., 2010; Peters et al., 2014; Peters et al., 2016) attests that carriers of nucleosynthetic anomalies for both Hf and W were uniformly distributed in the solar system when planetesimals formed, with IVB meteorites possibly being rare exceptions (Qin et al. 2008). Thus, ^{182}Hf-^{182}W chronology can be safely applied to most samples in the inner solar system, but acid resistant presolar phases in type 1 to 3 chondrite samples require careful digestion.

Chapter III

Control of different carrier phases on the nucleosynthetic Hf and W inventory of carbonaceous chondrites

III.1 Introduction

A variety of nucleosynthetic isotope anomalies have been discovered particularly within primitive, mostly unaltered chondrites. Such anomalies denote deviations form the isotope composition of terrestrial standards that are not accounted for by radioactive decay, cosmic rays or mass-dependent fractionation. Meteorites where such anomalies have been found, i.e., type 1 to 3 chondrites, have not completely been homogenized by thermal metamorphism or aqueous alteration (e.g., Huss et al., 2003; Davidson et al. 2014; Leitner et al., 2016) and thus kept much of their initial presolar grain inventory. Some of the anomalies detected can deviate from the terrestrial isotope abundances by several orders magnitudes. At least some of these variations have been directly measured in presolar phases (Boato, 1954; Clayton et al., 1973; Lewis et al., 1987; Anders and Zinner, 1993; Nittler et al., 2005; Ávila et al., 2012; Hoppe and Zinner, 2012) and could be attributed to certain nucleosynthetic environments because of their characteristic isotope fingerprints (e.g., Hoppe and Ott, 1997; Zinner, 1998; Nittler, 2003). However, presolar carrier are usually quite rare (<1%, e.g., Huss and Lewis 1995, Huss et al. 2003, Ott 1993, Zinner et al. 2003) and very small (~2nm – ~3um, e.g., Lewis et al. 1987; Choi et al. 1999), so that direct isotope analyses especially for trace elements are very challenging. A simple alternative to direct analyses presolar grains is the progressive acid dissolution of the different meteorite components. Using this approach, resolvable nucleosynthetic isotope anomalies relative to terrestrial compositions have been identified, i.e, for Cr (Rotaru et al., 1992; Trinquier et al. 2007) Mo (Dauphas et al., 2002) or Zr (Schönbächler et al. 2005). Also for heavier elements like Hf (Qin et al. 2011; chapter II), W (Burkhardt et al. 2012b; chapter II) and Os (Reisberg et al. 2009; Yokoyama et al. (2010) significant isotope variations among the components of chondrites have been resolved, and they could be linked to distinct stellar environments. Isotope measurements on chemically separated phases (leachates and residues) from type 1 to 3 chondrites can therefore (i) help to identify the nucleosynthetic processes and the stellar environments from which the pre-solar inventory in chondrites is derived and (ii) provide information about the variable conditions and processes within the solar nebula and possibly about the preceding molecular cloud stage.

Hafnium and W isotopes are well suited to study the nucleosynthetic inventory of the solar system, since the different isotopes of both elements are produced by the r-, s-, and as well the p-process. The s-process nuclides between Sr and Bi have been synthesized in asymptotic giant branch (AGB) stars. Several astrophysical settings have been suggested for the production of r-process nuclides, most of which are related to type II core collapse

supernova and neutron star mergers (Burbidge et al., 1957; Lattimer et al., 1977; Wallerstein et al., 1997; Rosswog et al., 1999). Heavy p-process isotopes such as ^{174}Hf and ^{180}W are thought to be formed by a complex chain of photodisintegration reactions of seed s- and r-process nuclides and β-decay reactions are thought to occur exclusively during type II core collapse supernovae (e.g., Arnould & Goriely, 2003; Rauscher et al., 2013). The Hf and W isotope contributions are as follows: ^{174}Hf (100% p-process), ^{176}Hf (97% s; 3% p), ^{177}Hf (17% s; 83% r), ^{178}Hf (59% s, 41% r), ^{179}Hf (41% s; 59% r), ^{180}Hf (89% s; 11% r), ^{180}W (96% s; 4% p), ^{182}W (64% s, 36% r), ^{183}W (62% s; 38% r), ^{184}W (79% s; 21% r) and ^{186}W (42%s, 58% r) (Bisterzo et al. (2011); Bisterzo et al. (2014). Of particularly interest are ^{174}Hf and ^{180}W, because they cannot only help discriminating between s- or r-process variations but also provide additional means to help identifying the sources of nucleosynthetic material that fed the solar system

First sequential leaching experiments for W and Hf revealed significant non-radiogenic variations in Hf and W isotopes (Burkhardt et al, 2012b; Qin et al. (2011). However, these studies did not include ^{174}Hf and ^{180}W, thus it remained unclear if the observed isotope variations were caused by s- or by r-process variations. First sequential leaching experiments for Hf and W including ^{174}Hf and ^{180}W described in chapter II revealed that the observed Hf and W isotope variations can solely be addressed to the variation of an s-process carrier phase. In contrast to this observation, r- and p-process carrier phases were found to be homogenized: neither any leachate nor any residue of the meteorites analyzed exhibits resolvable r- or p-process isotope variations. However, hence these first leaching experiments included only three leaching steps. As a consequence, the discrimination between different minerals in the chondrites was poor, so that (ii) potential r- and p-process variations may have been masked and (ii) identification of s-process Hf and W carrier phases is difficult. Thus, in this chapter, sequential leaching experiments included five leaching steps (i) to try resolve potential masked r- and or p-process variations and (ii) to try to better resolve what the s-process bearing Hf and W phases are. In this context focus lied on Murchison, Kainsaz and Allende which showed the biggest magnitude of Hf and W isotope variations in chapter II. Similar, to in chapter II, effects from cosmic ray exposure were also evaluated.

III.2 Analytical techniques

Approximately 5 g of CM 2 chondrite Murchison, CV 3 chondrite Allende and CO3 chondrite Kainsaz, were powdered and sequentially leached in reagents of increasing acid strength. Samples were powdered in an agate-mill for 1.5 minutes. The leaching protocol was chosen based on comparability to Burkhardt et al. (2015) and Qin et al. (2011) and leaching steps were as follows: Sample powders were first treated with 0.1 M HCl-0.001 M HF and left at 20°C. After 24 h samples were split into leachate (leachate 1) and residues. These residues were further treated with 4 M HNO_3- 0.001 M HF. After 5 days digesting at 20°C the samples were again separated into leachates (leachate 2) and residues. This step was followed by 6 M HCl-0.001 M HF for 24 h at 80°C and 3 days at 120°C in 14M HF- 3 M HCl. The most refractory minerals were then digested in 1:1 HNO_3-HF using pressure digestion vessels at 180°C for 3 days. It is of note that, in the case of Kainsaz an additional digestion step (3:1 HF-HNO_3 using pressure digestion vessels at 180°C for 4 days) was performed after the final residue digestion step. This step was included to ensure that all minerals were digested, since digestion step 4 (3 days at 120°C in 14M HF- 3 M HCl) was not performed for Kainsaz.

After leaching 1 ml perchloric acid was added to leachate and residue fractions to oxidize residual organic materials and to remove insoluble fluorides. Subsequently, all sample cuts were re-dissolved and dried down in cHNO_3 three times to further oxidize organic material and remove fluorides. After re-dissolution and dry down in 6M HCl for conversion to chloride form, all sample fractions were equilibrated in 6M HCl-0.06M HF. From these solutions, 1% aliquots were taken for element concentration measurements (Mg, Ca, Ti, Cr, Fe, Co, Ni, Zr, Hf and W) by sector-field ICP-MS (Thermo Fisher Element 2) using calibration and measurement procedures similar to those described in Funk et al. (2016, in revision). After evaporation, all sample splits were taken up in 1 M HCl and refluxed at 120°C overnight. Prior to ion exchange chemistry, 2 vol% H_2O_2 were added to every sample cut to prepare samples ready for ion exchange chemistry. In addition, two terrestrial bulk rock samples (La Palma Basalt 8 (LP8) and ancient gneiss complex sample 351 (AGC 351)), were also digested like the leachate and residue samples and put through ion exchange chemistry, to (i) demonstrate that the ion exchange chemistry is not introducing any bias and (ii) to use the terrestrial samples as a reliable external standard.

Hafnium and W were separated from the sample matrices using Biorad cation exchange resin AG50W ×8, Biorad anion resin AG1 ×8, Eichrom TEVA resin, and Eichrom Ln-Spec

resin (Tusch et al. in preparation; Münker et al., 2001; Peters et al., 2014; Münker et al., 2001 modified after Bast et al., 2015). This combination of ion-exchange resins granted very low Yb/Hf, W/Hf, Ta/Hf, Hf/W, Ta/W, and Os/W of $<1\times10^{-4}$ with chemical yields usually > 60%. Ultrapure analyte cuts were essential, especially for ^{174}Hf and ^{180}W because of their low abundance and the high abundance of their interfering isotopes (^{174}Yb; ^{180}Hf). Ytterbium /Hafnium and Hf/W of higher than 1×10^{-4} automatically lead to inaccurate ^{174}Hf and ^{180}W measurements (Peters et al. 2015; Schulz et al. 2013). Moreover, between the different ion exchange chromatography steps, all samples were re-dissolved and dried down in cHNO_3-H_2O_2 multiple times to remove possible organic residues. Oxidizing organic material is a critical step for W measurements because organic material can cause significant interferences on W isotopes (e.g., Kleine et al., 2004; Holst et al., 2015). After the last ion-exchange chromatography step, samples were first dissolved in 1:1 HNO_3-HCl, dried down, taken up again in 9:1 HNO_3-H_2O_2 and dried down again to finally destroy potential left-over organics from the ion exchange resin used. Interestingly, some kind of gel especially for Allende leachate 2, 3, Murchison leachate 2, 3 and Kainsaz leachate 3 and residue has formed when samples were loaded. For these samples chemical yields were below 10% and ion exchange chemistry had to be repeated. After removal of the gel, chemical yields were also > 60%, except for Hf yields of Kainsaz residue, Allende leachate 3 (<10%) and for W yields of Murchison leachate 3 and Allende leachate 3 (<10%).

Isotope measurements were performed in the joint Köln/Bonn clean lab facility using a Thermo Fisher Neptune Multicollector-ICPMS, equipped with two $10^{12}\Omega$ amplifiers. This instrument has nine Faraday collectors. Thus, all Hf and W isotopes can be measured statically. For Hf isotope measurement, ^{172}Yb, ^{175}Lu and ^{182}W were monitored and used to correct for isobaric interferences on ^{174}Hf (^{174}Yb), ^{176}Hf (^{176}Yb; ^{176}Lu), ^{180}Hf (^{180}W). All Faraday cups except those for ^{172}Yb and ^{174}Hf were connected to 10^{11} Ω resistors. Faraday cups ^{172}Yb and ^{174}Hf were connected to 10^{12} Ω resistors. For W isotope measurements, also ^{177}Hf, ^{178}Hf, ^{181}Ta and ^{188}Os were monitored and used to correct for isobaric interferences on ^{180}W (^{180}Hf; ^{180}Ta), ^{184}W (^{184}Os) and ^{186}W (^{186}Os). All Faraday cups except those for ^{177}Hf and ^{180}W were connected to 10^{11} Ω resistors. Faraday cups ^{177}Hf and ^{180}W were connected to 10^{12} Ω resistors. For Both Hf and W isotope measurements, sample solutions were introduced into the MC-ICPMS using a Cetac Aridus II desolvating system operated with Ar and N_2 and a PFA nebulizer with an uptake rate of ~100 µl/min. Instrumental mass bias for Hf isotope

ratios was corrected relative to a $^{179}Hf/^{177}Hf$ of 0.7325 and, in an alternative normalization procedure, relative to $^{180}Hf/^{177}Hf$ using a ratio of 1.8868. For W instrumental mass bias was corrected relative to $^{186}W/^{184}W$ of 0.9277 and alternatively to $^{186}W/^{183}W$ of 1.9859. In all cases, samples were bracketed by standard measurements and are reported as epsilon deviations, which is the deviation of the measured ratios from the terrestrial standard value (Münster AMES Hf and NIST 3613 W) in parts per 10000. Sample and standard solutions were ideally analyzed at matching concentrations providing beam intensities of ~100 mV for the minor isotopes ^{174}Hf and ^{180}W to ensure sufficient analytical precisions. Reported external uncertainties for samples were determined via repeated measurements of the AGC 351 sample. AGC 351 sample splits were analyzed at the same concentration levels as the meteorite samples. External reproducibility is reported in 2 standard deviations and was typically better than ±12.37 ε for $^{174}Hf/^{177}Hf$ and ±1.03 ε for $^{180}Hf/^{177}Hf$, respectively. For W isotope analyses external reproducibilities were typically better than 24.00 ε for $^{180}W/^{183}W$ and 0.79 ε for $^{183}W/^{184}W$, respectively. For both W and Hf analyses, sample and standard solution intensities were matched to within 10% to avoid possible intensity-related analytical bias. Total blanks were <50pg for all leachates and <1ng Hf and W for all autoclave-digested residues.

III.3 Results

III.3.1 Element concentrations

Leachate concentration data for Hf, W, Mg, Al, Ca, Ti, Cr, Fe, Co, Ni, and Zr from Murchison and Allende are given in Tables 1, 2 and 3 and shown in Figures 1 a and b.

Leachates 1 to 3 of Murchison contain most of the major elements including Mg, Al, Ca, Fe and Ni (>80%), indicating that most of the silicates and metal of Murchison has been dissolved within the first three leaching steps. Leachates 1 to 3 of Allende generally show the same trends except that Ca and Al seem to be depleted, being complementary enriched within the residue. Leachates 4 of Allende and Murchison generally show only minor abundances of major elements compared to leachates 1 to 3. Most abundant elements in leachate 4 are Mg, Fe, Ti, Co and Ni. The residues of Murchison usually do not contribute much to the major element budget anymore. Elements with highest fractions in Allende and Murchison residue are Ca, Al, Mg and to lesser extents Cr. At least in the case of Allende residue, the presence

of Ca and Al might argue for the presence of Calcium-aluminum rich inclusions that can make up 3 wt% of the Allende meteorite (Hezel et al. 2008).

As for Hf and W, leachate 1 did not contain any Hf for Murchison and Allende but 6 % of the total W released in Murchison and 4 % of the total W released in Allende. Leachates 2, 3 and 4 of Murchison contained 19%, 19%, and 27% Hf and 25%, 19% and 30% of the total W released in Murchison. The corresponding leachates of Allende contained 8%, 29%, and 32% Hf and 16%, 19%, and 31% of the total W. The residue of Murchison contains 35% and the residue of Allende 31% of the total Hf. For W, the residues contained 20% in the case of Murchison and 30% in the case of Allende.

It should be note, that the elemental concentration data for Kainsaz leachates and residues have not been determined.

Table 3: Major element release data for Murchison and Allende leachates and residues in %

Element	Mur l1	Mur l2	Mur l3	Mur l4	Mur res	All l1	All l2	All l3	All l4	All res
Mg	4	59	19	4	13	3	46	33	4	13
Al	0	62	19	1	19	13	17	27	2	41
Ca	44	17	14	6	18	12	9	26	8	45
Ti	0	30	23	39	9	0	20	28	47	5
Cr	2	43	16	20	18	0	3	10	64	23
Fe	6	69	20	4	1	4	44	32	16	4
Co	7	69	19	4	1	9	43	30	16	2
Ni	9	68	19	4	1	15	41	29	14	1
Zr	0	21	21	23	35	0	10	25	27	38

Mur l1 etc. refers to Murchison leachate 1 etc.

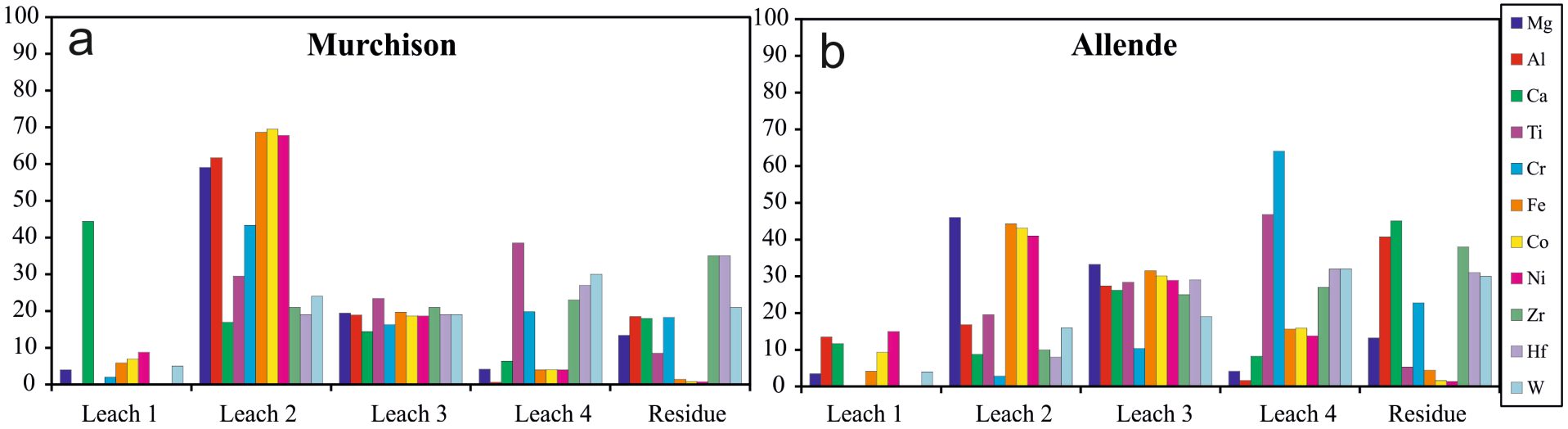

Fig. 1: Element distribution data for Murchison (a) and Allende (b) during sequential leaching. The overall release pattern is broadly similar for all chondrites. Slight differences are due the variable mineralogical inventory of different meteorites. The data for the different elements are given in color as illustrated in the legend.

III.3.2 Isotope compositions

Isotope results for Hf and W are all expressed in ε-units relative to the AMES Hf or NIST 3613 W standards, respectively. Measured Hf and W isotope results are listed in Tables 1 and 2

If normalized to $^{179}Hf/^{177}Hf$, leachates 2 to 3 of Murchison, Kainsaz and Allende generally show negative $\varepsilon^{1ii}Hf$ (i.e., $\varepsilon^{174,176,178,180}Hf$) for all analyzed chondrites, with Murchison and Kainsaz generally showing more pronounced Hf isotope variations than Allende (Fig. 2a, 3a, 4a). For instance, Murchison leachate 2 shows an $\varepsilon^{180}Hf$ of -4.73±0.12 whereas Kainsaz and Allende leachates 2 show $\varepsilon^{180}Hf$ of -3.35±0.10 and -2.05±0.28, respectively. Complementary to these patterns, the residues of Murchison, Kainsaz and Allende show positive $\varepsilon^{180}Hf$ isotope signatures, of 2.28±0.10, 4.07±0.68 and 0.54±0.13, respectively. For W isotopes, an inverse trend compared to stable Hf isotopes is observed (excluding radiogenic ^{182}W): leachates 1 to 3 usually show positive $\varepsilon^{180}W$ and $\varepsilon^{183}W$ values if normalized to $^{186}W/^{184}W$ whereas leachates 4 and the residues show negative $\varepsilon^{180}W$ and $\varepsilon^{183}W$. For instance, leachates 1 of Murchison, Kainsaz and Allende show $\varepsilon^{183}W$ of 1.11±0.15, 0.79±0.53 and 1.00±0.15, whereas the complementary residues show $\varepsilon^{183}W$ of -2.53±0.19, -0.98±0.15 and -0.56±0.33, respectively. Radiogenic ^{182}W seems to be usually slightly enriched in leachates 1 and significantly depleted in the following leachates and the residue.

Note that leachate 1 of, Murchison and Allende, as well as Kainsaz residue 2 contained Hf only at blank levels and are thus not considered any further. Kainsaz residue 2 also contained W at blank levels only and is thus also not considered any further.

Importantly, both terrestrial samples (LP 8 and AGC 351) show terrestrial Hf and W isotope signatures that agree with the bracketing standards within analytical uncertainty. This result emphasizes the reliability of the ion exchange procedures and renders analytical artefacts during ion exchange chemistry unlikely.

Table 1: Hf isotope and concentration data

sample	fraction Hf released (%)	$\varepsilon^{174}Hf$[d]	$\varepsilon^{176}Hf$[a, d]	$\varepsilon^{178}Hf$[d]	$\varepsilon^{180}Hf$[d]	$\varepsilon^{174}Hf$[d]	$\varepsilon^{176}Hf$[b, d]	$\varepsilon^{177}Hf$[d]	$\varepsilon^{179}Hf$[d]
		mass bias correction relative to $^{179}Hf/^{177}Hf$				mass bias correction relative to $^{180}Hf/^{177}Hf$			
Murchison		-0.26 ± 0.45	-0.09 ± 0.85	-0.05 ± 0.19	0.07 ± 0.21	-0.44 ± 0.54	22.25 ± 0.85	0.09 ± 0.12	0.03 ± 0.25
Leachate 1	0	blank	Blank	Blank	Blank	blank	Blank	blank	blank
Leachate 2	19	-3.14 ± 1.08	-20.84 ± 0.15	-4.48 ± 0.07	-4.73 ± 0.12	-5.02 ± 1.20	1.40 ± 0.22	2.93 ± 0.07	6.08 ± 0.11
Leachate 3	19	-2.26 ± 0.78	-11.59 ± 0.15	-2.58 ± 0.07	-2.70 ± 0.10	-3.57 ± 0.92	11.34 ± 0.22	1.67 ± 0.07	3.51 ± 0.11
Leachate 4	27	1.24 ± 0.80	9.41 ± 0.15	2.17 ± 0.07	2.49 ± 0.11	2.06 ± 0.92	31.63 ± 0.22	-1.31 ± 0.07	-3.02 ± 0.11
Residue	35	1.21 ± 0.78	9.88 ± 0.15	1.98 ± 0.07	2.28 ± 0.10	1.78 ± 0.92	32.04 ± 0.22	-1.21 ± 0.07	-2.74 ± 0.11
Kainsaz									
Leachate 1	tbd[c]	-1.78 ± 6.52	-19.43 ± 1.26	-3.28 ± 0.37	-3.49 ± 0.73	-3.37 ± 6.39	3.75 ± 1.28	1.79 ± 0.40	3.80 ± 0.53
Leachate 2	tbd[c]	-1.96 ± 0.78	-17.53 ± 0.15	-2.79 ± 0.07	-3.35 ± 0.10	-3.64 ± 0.92	5.63 ± 0.22	1.70 ± 0.07	3.89 ± 0.11
Leachate 3	tbd[c]	1.21 ± 1.78	4.34 ± 0.25	0.77 ± 0.09	0.64 ± 0.14	2.68 ± 1.84	26.64 ± 0.22	-0.52 ± 0.09	-0.97 ± 0.11
Residue	tbd[c]	3.31 ± 5.01	17.95 ± 1.45	3.48 ± 0.30	4.07 ± 0.68	3.31 ± 5.20	43.51 ± 1.65	-1.92 ± 0.26	-3.91 ± 0.47
Residue2	blank	blank	Blank	Blank	Blank	Blank	Blank	Blank	Blank
Allende		0.28 ± 3.67		-0.09 ± 0.15	0.01 ± 0.31	0.18± 3.93		0.11 ± 0.15	0.12 ± 0.20
Leachate 1	0	blank	Blank	Blank	Blank	Blank	Blank	Blank	Blank
Leachate 2	8	-1.27 ± 5.42	*Spike*	-1.89 ± 0.16	*-2.05 ± 0.28*	-2.23 ± 5.54	*Spike*	1.24 ± 0.14	2.66 ± 0.21
Leachate 3	29	-0.18 ± 12.37	*Spike*	-0.27 ± 0.49	*-0.29 ± 1.03*	-0.32 ±13.26	*Spike*	0.18 ± 0.49	0.38 ± 0.65
Leachate 4	32	1.43 ± 0.85	3.93 ± 0.15	0.08 ± 0.07	0.26 ± 0.10	1.36 ± 0.92	26.42 ± 0.22	0.01 ± 0.07	-0.15 ± 0.11
Residue	31	-0.09 ± 1.11	6.16 ± 0.15	0.34 ± 0.07	0.54 ± 0.13	0.03 ± 1.10	28.81 ± 0.22	-0.14 ± 0.08	-0.47 ± 0.11
terrestrial									
AGC 351		-0.25 ± 0.78	-47.86 ± 0.15	-0.01 ± 0.07	-0.01 ± 0.10	-0.31 ± 0.92	-25.77 ± 0.22	0.01 ± 0.07	0.01 ± 0.11
LP8		-0.22 ± 0.78	5.73 ± 0.15	0.03 ± 0.07	-0.09 ± 0.10	-0.25 ± 0.92	27.98 ± 0.22	-0.05 ± 0.07	-0.01 ± 0.11

[a]. $\varepsilon^{176}Hf$ reported to Bouvier et al. (2008) (0.282785).
[b]. $\varepsilon^{176}Hf$ reported to Ames Hf standard.
[c] tbd refers to "to be determined" [d] reported uncertainties for samples are the external reproducibility (2 S.D.) of the repeated measurements of the AGC 351 sample at similar concentration levels, measured the same day. Uncertainties on calculated bulk rocks are given by the error propagated 2SD of the individual variables (concentration, isotope signature) using Monte Carlo Simulation (Sprung et al. 2013).

Table 2: W isotope and concentration data

Sample	fraction W released (%)	$\varepsilon^{180}W^b$	$\varepsilon^{182}W^b$	$\varepsilon^{183}W^b$	$\varepsilon^{180}W^b$	$\varepsilon^{182}W^b$	$\varepsilon^{184}W^b$
		mass bias correction relative $^{186}W/^{184}W$			mass bias correction relative $^{186}W/^{183}W$		
Murchison		-0.29 ± 6.94	-2.08 ± 0.24	-0.21 ± 0.23	-0.09 ± 6.95	-1.76 ± 0.21	0.11± 0.21
Leachate 1	6	4.43 ± 4.75	0.03 ± 0.20	1.11 ± 0.20	1.93 ± 4.85	-1.79 ± 0.19	-0.73 ± 0.17
Leachate 2	25	5.88 ± 4.41	0.23 ± 0.20	1.42 ± 0.20	2.87 ± 4.06	-1.54 ± 0.19	-0.95 ± 0.17
Leachate 3	19	4.53 ± 35.19	-1.98 ± 1.02	0.29 ± 1.01	3.10 ± 35.02	-1.54 ± 1.06	-0.16 ± 1.01
Leachate 4	30	-3.59 ± 2.75	-2.42 ± 0.08	-0.64 ± 0.15	-1.98 ± 2.85	-1.91 ± 0.09	0.36 ± 0.12
Residue	20	-9.24 ± 3.10	-5.25 ± 0.20	-2.53 ± 0.19	-3.78 ± 3.03	-2.01 ± 0.15	1.59 ± 0.13
Kainsaz							
Leachate 1	tbd[a]	6.40 ± 6.34	-1.05 ± 1.00	0.79 ± 0.53	2.68 ± 5.92	-1.71 ± 0.46	-0.52 ± 0.35
Leachate 2	tbd[a]	1.12 ± 2.75	-1.18 ± 0.08	0.29 ± 0.15	0.60 ± 2.85	-1.64 ± 0.09	-0.19 ± 0.12
Leachate 3	tbd[a]	-0.05 ± 2.75	-1.66 ± 0.08	0.01 ± 0.15	-0.38 ± 2.85	-1.70 ± 0.09	-0.01 ± 0.12
Residue	tbd[a]	-3.94 ± 2.75	-3.28 ± 0.08	-0.98 ± 0.15	-2.22 ± 2.85	-1.98 ± 0.09	0.65 ± 0.12
Residue2	blank	Blank	Blank	blank	blank	blank	Blank
Allende		3.88 ± 5.15	-1.82 ± 0.21	0.01 ± 0.18	2.34 ± 5.04	-1.78 ± 0.18	-0.01 ± 0.13
Leachate 1	4	3.90 ± 4.75	0.03 ± 0.20	1.00 ± 0.20	2.07 ± 4.85	-1.54 ± 0.19	-0.69 ± 0.17
Leachate 2	16	5.18 ± 2.75	-2.15 ± 0.08	0.32 ± 0.15	2.18 ± 2.85	-2.35 ± 0.09	-0.21 ± 0.12
Leachate 3	19	18.52 ± 24.00	-1.09 ± 1.01	0.34 ± 0.79	10.46 ± 23.93	-1.68 ± 0.78	-0.22 ± 0.52
Leachate 4	31	0.26 ± 2.75	-1.68 ± 0.08	0.06 ± 0.15	0.13 ± 2.85	-1.50 ± 0.09	-0.04 ± 0.12
Residue	30	-2.36 ± 6.77	-2.51 ± 0.24	-0.56 ± 0.23	-0.33 ± 6.72	-1.85 ± 0.28	0.36 ± 0.22
terrestrial							
AGC 351		-0.27 ± 2.75	0.04 ± 0.08	-0.09 ± 0.15	-0.05 ± 2.85	-0.04 ± 0.09	0.06 ± 0.12
LP8		0.39 ± 2.75	-0.08 ± 0.08	-0.07 ± 0.15	0.18 ± 2.85	0.07 ± 0.09	0.05 ± 0.12

[a] tbd refers to "to be determined" [b] reported uncertainties for samples are the external reproducibility (2 S.D.) of the repeated measurements of the AGC 351 sample at similar concentration levels, measured the same day. Uncertainties on calculated bulk rocks are given by the error propagated 2SD of the individual variables (concentration, isotope signature) using Monte Carlo Simulation (Sprung et al. 2013)..

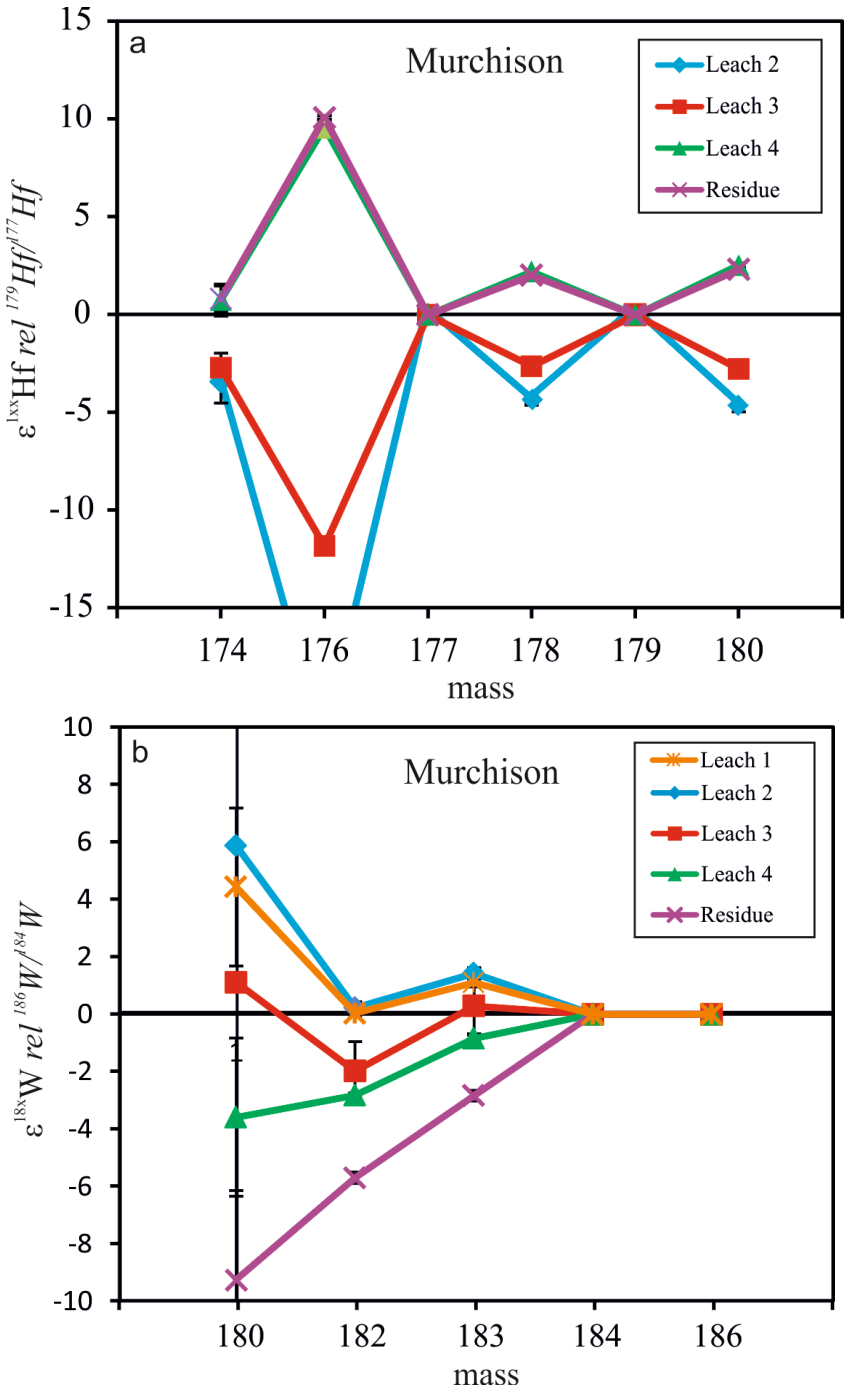

Fig. 2 a,b: Hf (a) and W (b) isotope data for Murchison. All isotope ratios are reported relative to the Hf AMES standard (a) or W NIST 3163 standard (b). Hf data are normalized to $^{179}Hf/^{177}Hf$; W data are normalized to $^{186}W/^{184}W$. Reported uncertainties for samples are the external reproducibility (2 S.D.) of the repeated measurements of the AGC 351 sample, measured the same day. Different colors refer to the different leaching steps. $\varepsilon^{176}Hf$ reported to Bouvier et al. (2008) (0.282785). Murch l1 etc. refers to Murchison leachate 1 etc.

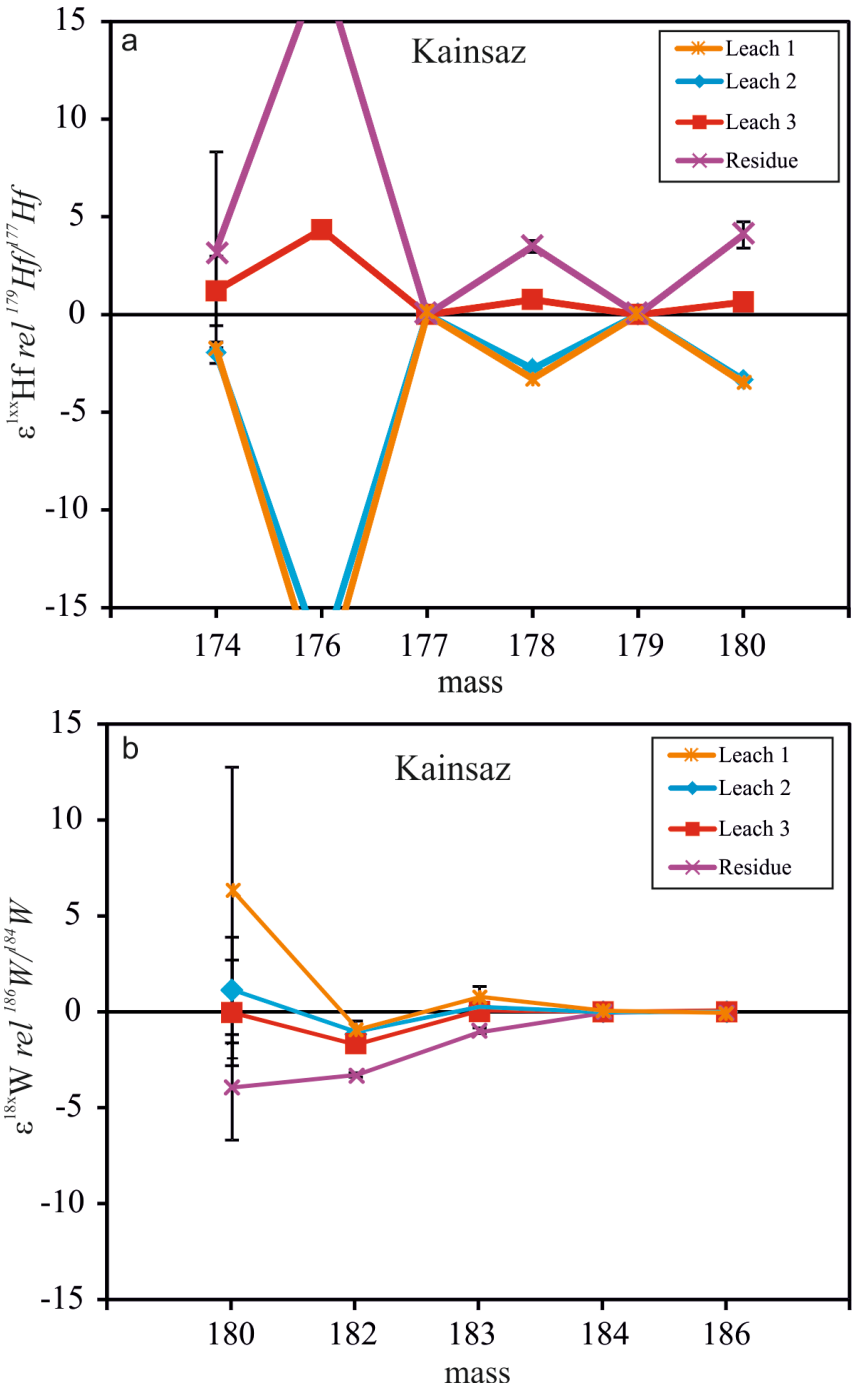

Fig. 3 a,b: Hf (a) and W (b) isotope data for Kainsaz. All isotope ratios are reported relative to the Hf AMES standard (a) or W NIST 3163 standard (b). Hf data normalized to $^{179}Hf/^{177}Hf$; W data normalized to normalized to $^{186}W/^{184}W$. Reported uncertainties for samples are the external reproducibility (2 S.D.) of the repeated measurements of the AGC 351 sample, measured the same day. Different colors refer to the different leaching steps. $\varepsilon^{176}Hf$ reported to Bouvier et al. (2008) (0.282785). Kain l1 etc. refers to Kainsaz leachate 1 etc.

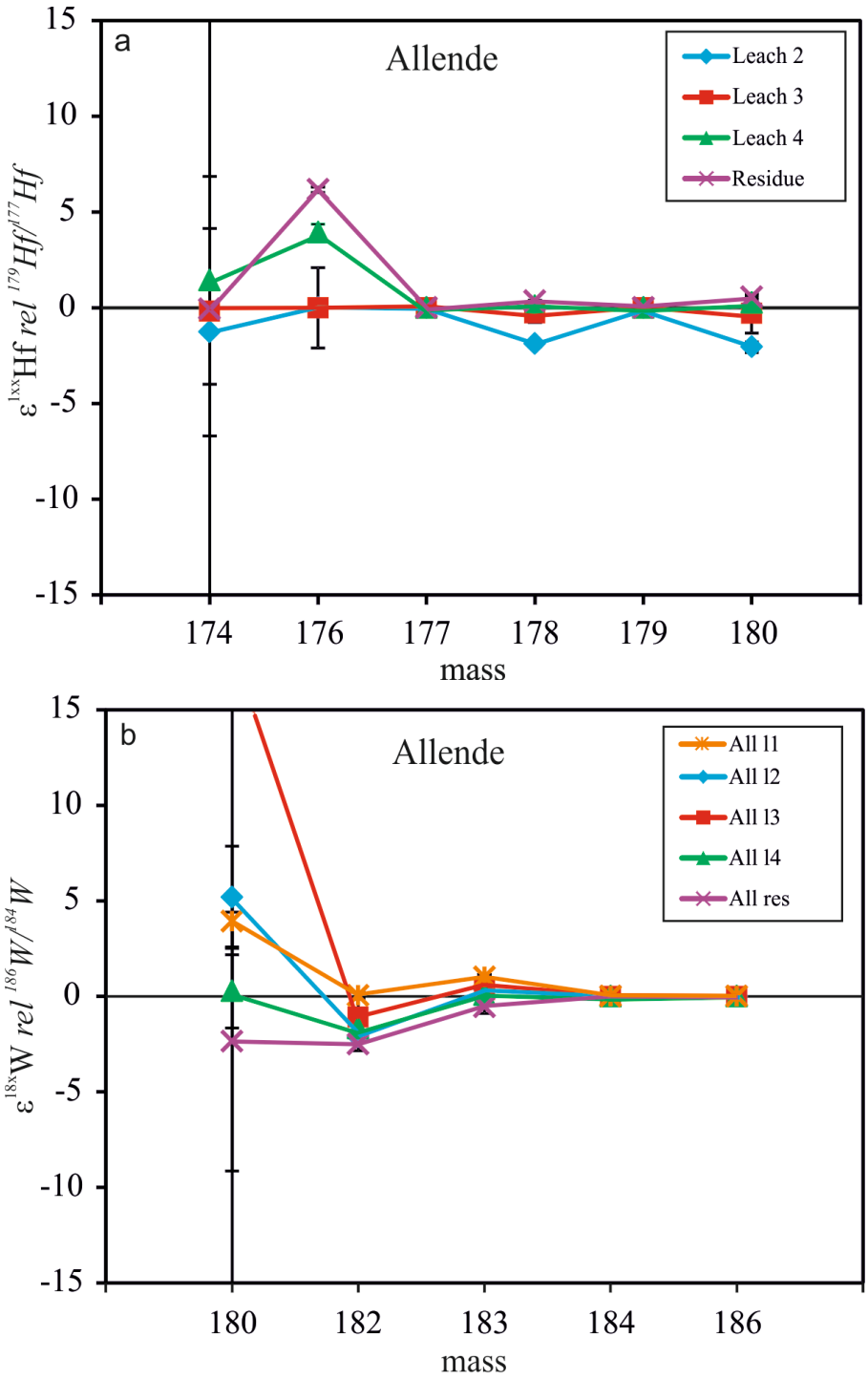

Fig. 4 a,b: Hf (a) and W (b) isotope data for Allende. All isotope ratios are reported relative to the Hf AMES standard (a) or W NIST 3163 standard (b). Hf data normalized to $^{179}Hf/^{177}Hf$; W data normalized to normalized to $^{186}W/^{184}W$. Reported uncertainties for samples are the external reproducibility (2 S.D.) of the repeated measurements of the AGC 351 sample, measured the same day. Different colors refer to the different leaching steps. $\varepsilon^{176}Hf$ reported to Bouvier et al. (2008) (0.282785). All l1 etc. refers to Allende leachate 1 etc.

III.4 Discussion

III.4.1 Comparison with previous Hf and W isotope data for leaching experiments on chondrites

Leachate and residue data of this study generally display negative ε^{1ii}Hf isotope deviations in the first leaching steps, with complementary positive Hf isotope variations in subsequent leachates and residues. The same trend is observed for leachate and residue data by Qin et al. (2011) and by sequential leaching data in chapter II, obtained for CM, CV, CO and ordinary chondrites. In addition to this qualitative agreement, also the relative magnitude of coupled anomalies in ε^{178}Hf and ε^{180}Hf found by Qin et al. (2011) and within the sequential leaching data in chapter II, corresponds to those reported in this study with the data of Qin et al. (2011) and the leaching data of chapter II defining a slope of 0.91±0.17 and 0.87±0.05 and our data defining a slope of 0.90±0.05 in ε^{178}Hf vs. ε^{180}Hf space (Fig.5). It should be also of note that, at least some data points of Qin et al. (2011) are significantly offset from the regression line of this study and that of chapter II (see chapter II section 4.3.1) within the ε^{178}Hf vs. ε^{180}Hf space. What actually caused some of those data to be offset is unclear. Neutron capture effects cannot account for the offset towards too low ε^{178}Hf (Fig.5; see discussion below) and further cannot affect individual fractions of monogenetic meteorite specimen at that scale. Previously, analytical artefacts on mass ^{178}Hf associated with Zr contents in the Hf-analyte have been reported (Sprung et al., 2010; Peters et al., 2015). It appears possible that the data of Qin et al. (2011) have been affected by similar effects because no special care has been taken to remove Zr from the analyte substantially (Carlson et al. 2006; Qin et al., 2011).

In our W isotope dataset, first leachates tend to show positive ε^{18i}W isotope deviations (in the case of ε^{182}W generally less negative ε^{182}W). Complementary to these patterns, residues exhibit negative W isotope deviations. This pattern is generally consistent with results of previous studies (e.g., Burkhardt and Schönbächler, 2015; chapter II). A regression through the data of Burkhardt and Schönbächler (2015) and the leaching data of chapter II give slopes in ε^{182}W vs ε^{183}W spaces of 1.41±0.05 with an ^{182}W intercept of -2.29±0.47 and of 1.37±0.24 and an ε^{182}W intercept of -1.81±0.23, respectively. These results agree with the results of this study that define a slope of 1.50±0.25 with an intercept of -1.76±0.22 (Fig.6).

The generally consistency of the Hf and W isotope data between the different studies imply that the different leaching protocols applied lead to dissolution of broadly similar

carrier phases. Moreover, calculated whole rock Hf and W isotope signatures of the different analyzed meteorites analyzed in this study are in good agreement with previous results for bulk rocks (e.g., Kleine et al. 2004; Bouvier et al. 2008; Sprung et al. 2010, Akram et al. 2013; Peters et al. 2014; 2016). This is indicating that all anomalous carrier phases have been sampled and that full sample dissolution has broadly been achieved in our leaching experiments.

III.4.2 Cosmogenic effects

Especially meteorites with high exposure ages can be significantly affected by secondary neutron capture. These effects can significantly alter the isotope compositions of meteorites. Significant neutron capture has been reported for several elements, e.g., Sm and Gd (Eugster et al., 1970; Lugmair and Marti, 1971; Russ III et al., 1971; Hidaka et al., 2000), also including Hf and W, especially for meteorites with high exposure ages (e.g., Sprung et al. 2010; Kruijer et al. 2013). Thus, it is necessary to carefully evaluate these effects before start interpreting the data in terms of nucleosynthetic heterogeneities. Although chondrites are reported to have low exposure ages of < 120 Ma (Eugster, 2003; Herzog, 2003) and can thus be assumed to show only insignificant cosmic ray effects we applied the neutron capture model of Sprung et al. (2010) for Hf isotopes to completely evaluate neutron capture effects for the samples analyzed in this study. Neutron capture causes particularly significant burn-out of ^{177}Hf and ^{178}Hf leading to a distinct negative slope in ε^{178}Hf vs. ε^{180}Hf space that is approximately perpendicular to the coupled offset in both isotope signatures that would relate to s- or r-process Hf isotope anomalies. The samples analyzed in this study span a regression with a slope of 0.90±0.05 (MSWD 5.9) whereas the slope predicted by neutron capture is -0.60 (Fig.5). Thus, the data are indicating that the samples have not been significantly affected by neutron capture effects. Since Hf isotopes can also be used to evaluate neutron capture effects on W isotopes (e.g. https://www-nds.iaea.org/exfor/endf.htm; Kruijer et al., 2015), neutron capture effects can also be regarded as insignificant for all involved W isotope ratios as well. Hf isotopes and the relevant Ta (^{181}Ta (n,γ) ^{182}Ta (β^-, e^- + ν_e) ^{182}W) and W isotopes are most sensitive to neutron capture at the same, epithermal neutron energy.

III.4.3 Cause of the observed Hf and W isotope variations

The Hf and W isotope compositions obtained in this study are highly correlated. The slope in ε^{178}Hf vs. ε^{180}Hf space (relative to ^{179}Hf/^{177}Hf) is 0.90±0.05 with a MSWD of 5.9. This is consistent with the predicted slopes for s or r-process variations by i.e., Bisterzo et al (2011) (Fig. 5). However, to distinguish whether the variations result from acid resistant s-process carrier phases or from the preferential dissolution of r-process carrier phases, it is pivotal to consider the p-process isotope ^{174}Hf. The slope within ε^{174}Hf vs. ε^{180}Hf space is 0.63±0.12 (MSWD 1.8) (Fig.7). This correlation line is most consistent with an s-process variation, which yields a theoretical slope of +0.53 (Bisterzo et al. 2011). The slope predicted for r-process variation is +3.30. Thus, similar to results of chapter II and although more leaching steps are preformed, no signs of an r- and/or p-process Hf variation were found.

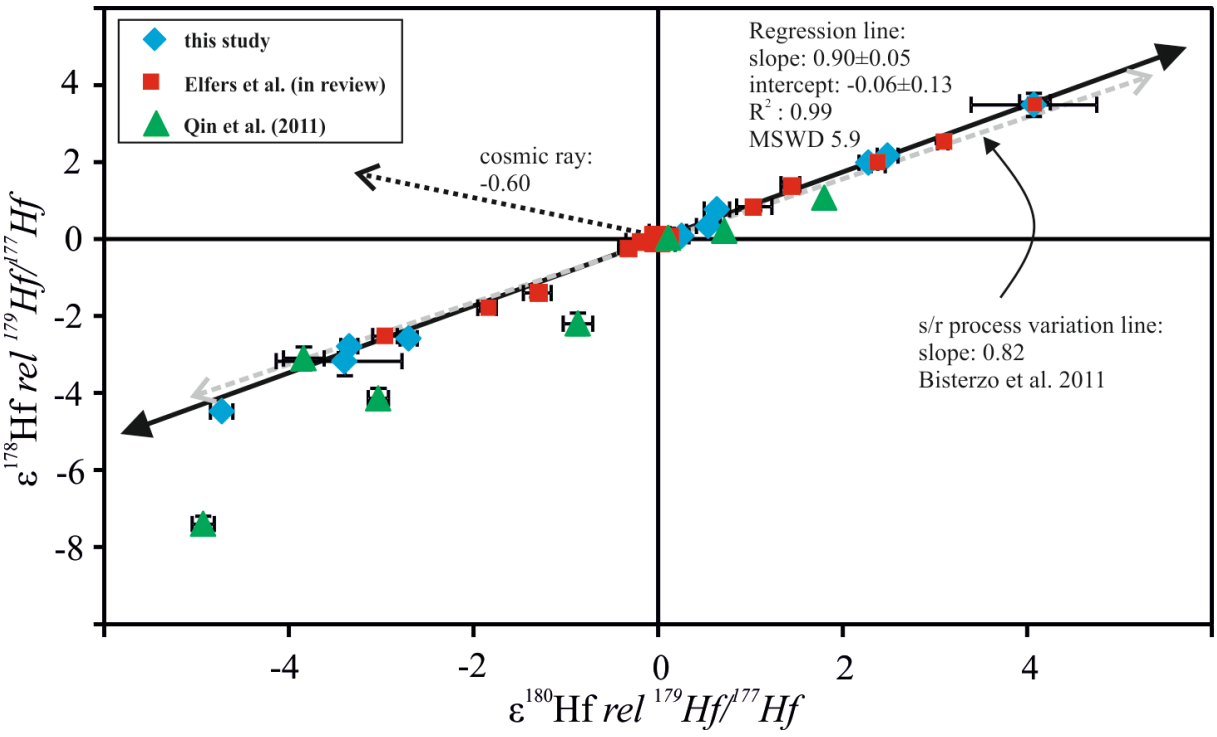

Fig.5: ε^{178}Hf vs. ε^{180}Hf data normalized to ^{179}Hf/^{177}Hf for the sequentially leached meteorite samples of this study, Elfers et al. (in review) and Qin et al. (2011). The sequential leaching data are well correlated following the s/r-process variation line predicted by Bisterzo et al. (2011). Cosmogenic neutron capture effects (Sprung et al. 2010) are negligible. Different colors refer to the different studies. Some data points of Qin et al. (2011) plot offset because of most likely molecular interferences. The regression line is calculated by using IsoPlot 4.13.

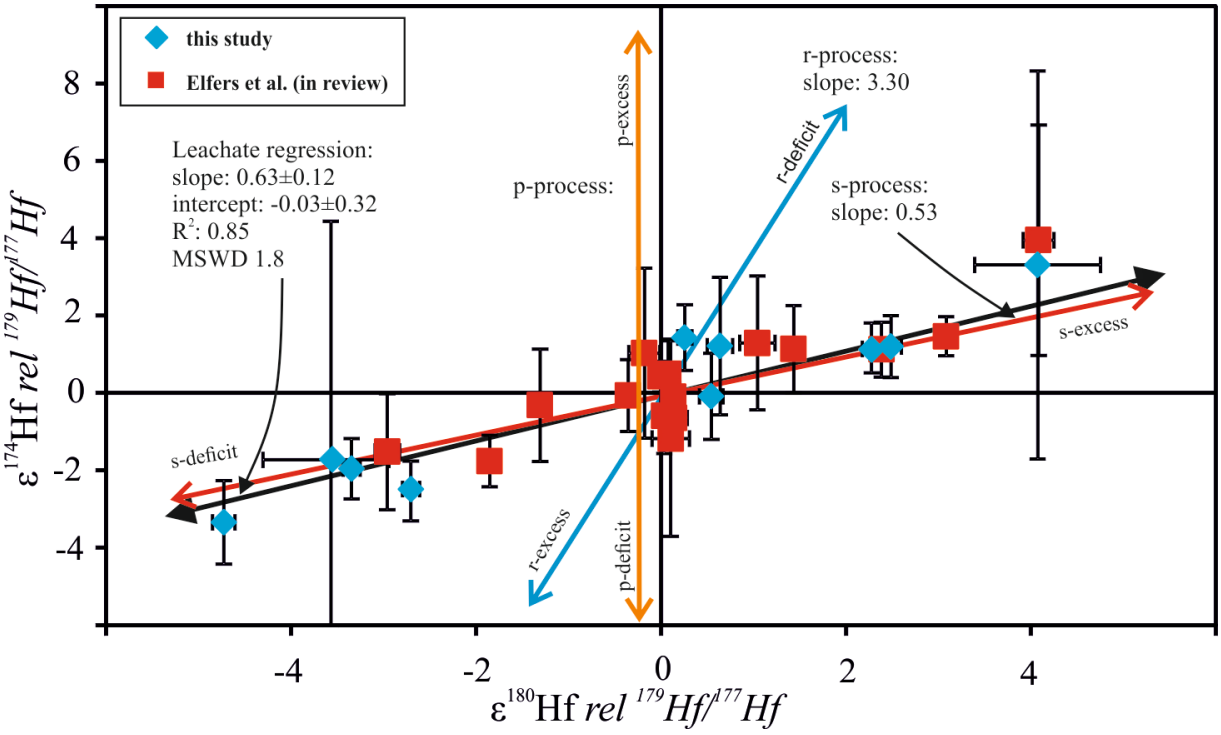

Fig. 6: ε^{174}Hf vs. ε^{180}Hf normalized to $^{179}Hf/^{177}Hf$ data for the sequentially leached meteorite samples of this study and Elfers et al. (in review) compared with the stellar model of Bisterzo et al. (2011). All data are well correlated and variations can be best explained by variability of s-process components. Different colors refer to the different studies. The regression line is calculated by using IsoPlot 4.13.

For W isotope compositions, the data points towards the same direction as the Hf isotope data. Isotope compositions in ε^{182}W vs. ε^{183}W space yield a slope of 1.50±0.25, which is consistent with s- or r-process variations (Fig.7). Further, if p-process ^{180}W is taken into account, an ε^{180}W vs. ε^{183}W space yield a slope of 4.22±0.98 (MSWD 0.85). This is very similar to an s-process variation slope of +4.25 predicted by Bisterzo et al. (2014) (Fig.8). The slope predicted for r-process variation is +1.51. Thus, similar to the Hf data, the W data also points towards an s-process variation only. Therefore similar to the Hf data and although more leaching steps were performed, no signs of an r- and/or p-process variation were found.

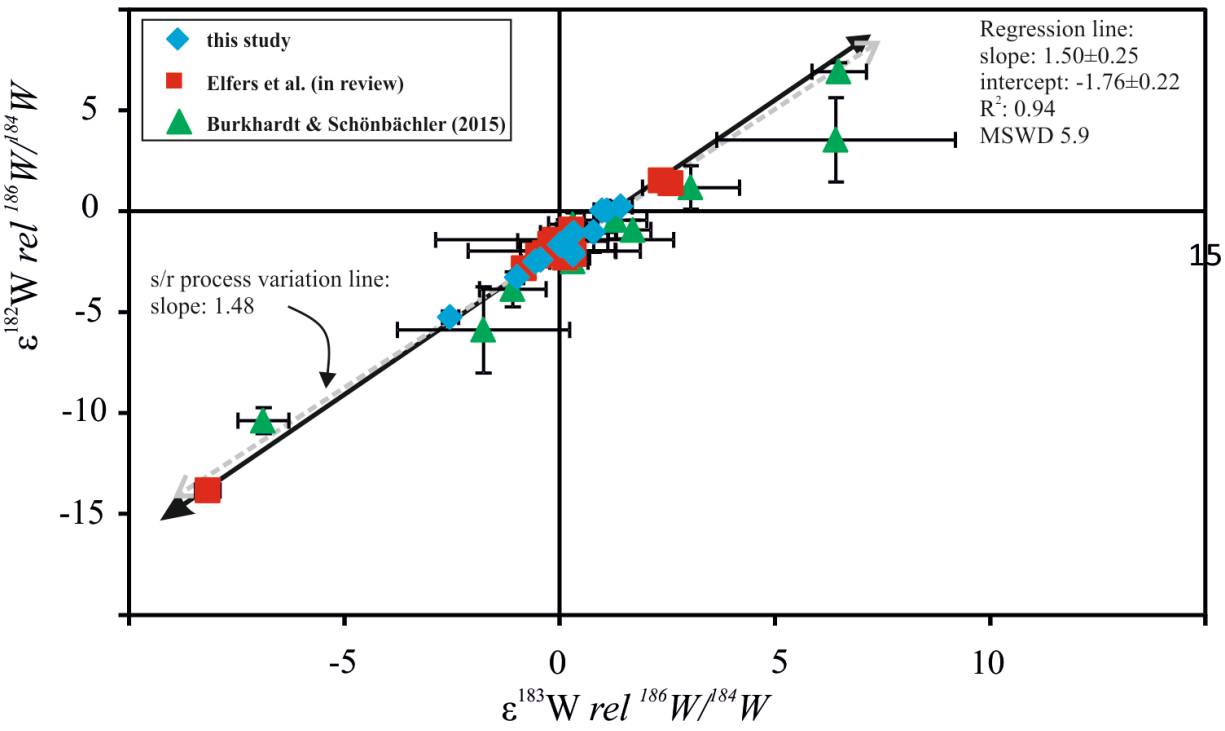

Fig.7: $\varepsilon^{182}W$ vs. $\varepsilon^{183}W$ normalized to $^{186}W/^{184}W$ data for the sequentially leached meteorite samples of this study, the data of chapter II and Burkhardt and Schönbächler, (2015) compared with the stellar model of Bisterzo et al. (2014). The data of the different studies are coherent and well correlated and follow the s/r-process variation line predicted by Bisterzo et al. (2011). Different colors refer to the different studies. The regression line is calculated by using IsoPlot 4.13.

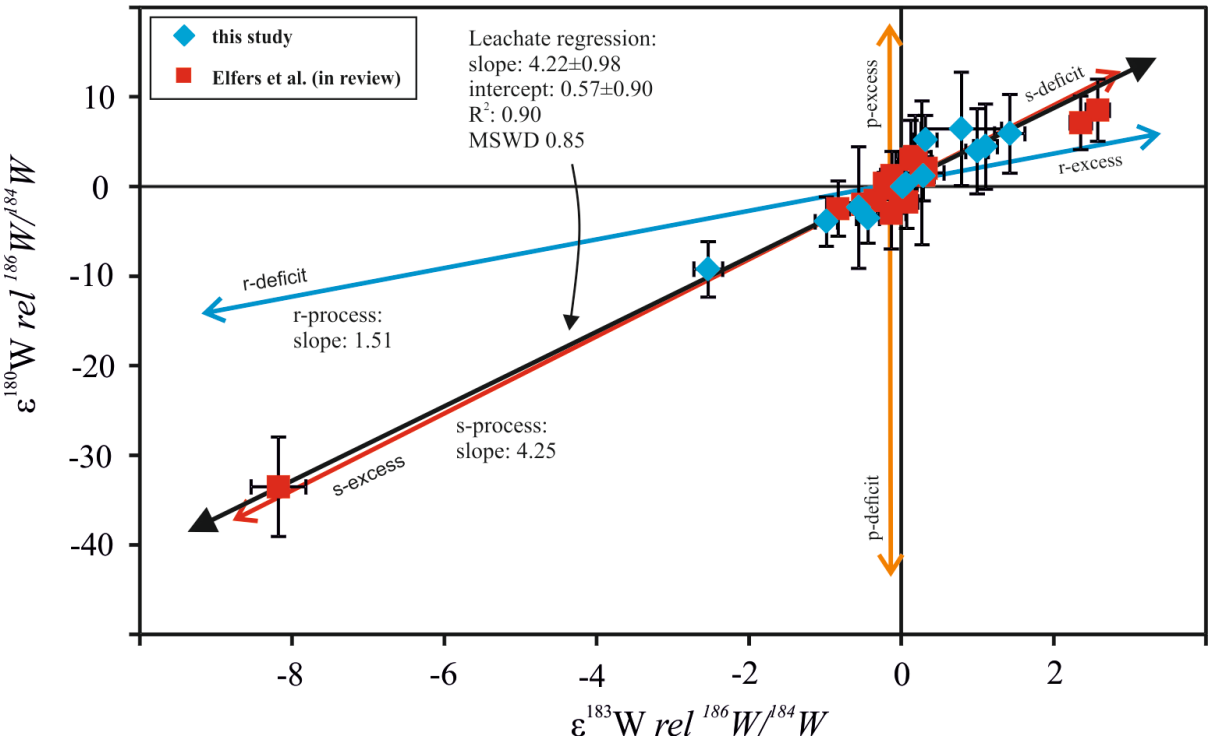

Fig. 8: $\varepsilon^{180}W$ vs. $\varepsilon^{183}W$ normalized to $^{186}W/^{184}W$ data for the sequentially leached meteorite samples of this study and the data of chapter II compared with the stellar model of Bisterzo et al. (2014). All data are well correlated and variations can be best explained by variability of s-process components. Different colors refer to the different studies. The regression line is calculated by using IsoPlot 4.13.

III.4.4 Identification of s- process carrier phases

As described in section 4.3, the observed Hf and W isotope variations amongst leachates and residues are caused by variations in the abundance of s-process Hf and W only. On the basis of mass balance considerations and chemical resistance of SiC, Burkhardt and Schönbächler (2015) identified mainstream SiC as one potential carrier phase that causes s-process W isotope variations among leachates and residues of different types of chondrites. Our own results of first leaching experiments supported this view (chapter II). For the following mass balance considerations, it nevertheless is crucial to explore the various input parameters for mass balancing in detail: Throughout, SiC grain abundances of Huss et al (2003; Murchison = 13.5ppm, Allende = 0.01ppm) with 90% mainstream SiC fraction (e.g., Hynes and Gyngard, 2009) of the total SiC are used. Considerable uncertainty exists with respect to W concentrations in mainstream SiC. For instance, Avila et al. (2012) in their presolar mainstream SiC study reported W concentrations in mainstream SiC to vary between ~1.8 (single grains) and 6.0 ppm (mainstream SiC-enriched fractions). Because of the possibility of contamination by solar W in the SiC-enriched fractions, we here adopt the low end of this range for all mass balance calculations, i.e., we assume that SiC contain 2.1 ppm W. Note that using this value of 2.4 ppm W produces internally consistent results for Murchison by assuming that 40% of total mainstream SiC is dissolved in leaching step 4 and 60% within the residue (Table 4). Leaching step 3 might be somewhat special: Within analytical uncertainty, a slight, yet not resolved, s-process enrichment could be hidden ($\varepsilon^{183}W$ = 0.29±1.01) when compared to the leachates 1 and 2 ($\varepsilon^{183}W$ = 1.11±0.15; $\varepsilon^{183}W$ = 1.42±0.26). Thus, possibly an additional s-process bearing phase may be present in leachate 3 of Murchison. The presence of such a phase would be consistent with observations in chapter II. There, using a less elaborate leaching procedure, an s-process enrichment ($\varepsilon^{183}W$ = -0.50±0.08) within leaching step 2 of Murchison was interpreted to either result from smaller SiC grains being dissolved or to result from the dissolution of chemical less resistant phase(s). Note that attributing this latter s-process (chapter II) to mainstream SiC would require a W concentration in SiC of at least 4.6 ppm, which would not provide a reasonable solution for the isotope results in this chapter. Thus, the combined information from chapter II and this chapter most likely implies the presence of one or more additional less chemical resistant s-process W bearing phase(s).

That additional s-process bearing phases to mainstream SiC must be present is also indicated by mass balance calculations for Allende (Table 4). In contrast to Murchison, no resolvable s-process variation are expected between Allende leachates and residue if mainstream SiC is the dominant s-process carrying phase because the total amount of s-process carried by mainstream SiC is too low to cause any resolvable isotope anomalies that would indicate s-process W enrichment, even if all mainstream SiC is restricted to the residue and if it is assumed that all SiC grains are s-process enriched instead of mainstream grains only (Table 4). In contrast, the residue of Allende shows significant s-process enrichments ($\varepsilon^{183}W$ = -0.56 ±0.33). Although CAIs may be present in the residue as indicated by its high Ca and Al content, their presence cannot explain the s-process W enrichment because CAIs are marked by positive $\varepsilon^{183}W$ instead (Kruijer et al. 2014).

Moreover, our Hf isotope data also point towards the presence of more than one specific s-process bearing phase: mass balancing using the same parameters as above and a Hf/W of ca. 0.22 (Avila et al., 2012) implies that the total amount of s-process Hf carried by SiC is insufficient to explain the observed Hf isotope variation in Murchison and Allende solely by mainstream SiC (Table 4). Interestingly, excess s-process Hf seems to be correlated with increasing HF molarity employed during leaching. Similar observations were made in chapter II and were taken to indicate the dissolution of oxides and/or silicates. However, taking into account that most (>80%) of the Mg, Fe and Ni were dissolved during the first three leachates of Allende and Murchison, i.e., most of the silicates and metal, the s-process Hf enrichments are most likely related to non-silicate phases.

Notably, leachates 4 are dominated by the release of Ti, Cr, HFSE, and to lesser extent also Fe, Ni, and Co (table 3; figure 1 a, b). Nielsen et al. (1994) and Wijbrans et al. (2016) have shown that spinel-like minerals in particular can contain significant amounts of Ti, Cr, and HFSE. Furthermore, Ni and Co are typical minor elements in spinels (Deer et al. 1992). Spinel-like minerals are known to occur in CM (Fuchs et al., 1973; Simon et al. 1994) and are abundant in CV chondrites (Brearley and Jones, 1998; Riebe, 2009), in which they are mostly associated to oxidation and exsolution processes as secondary chromite (Cr_2O_3) and magnetite (Fe_3O_4; Choi et al., 1997; Grossman and Brearley, 2005). Thus, the observed element release pattern in leachate 4 of Allende and Murchison is most likely accompanied by the extensive dissolution of oxide minerals. Note that at C/O < 1 around AGB stars, Hf is thought to condense as HfO_2 prior to the condensation of other oxides like corundum (Al_2O_3), spinel sensu stricto ($Mg_2Al_2O_2$) or hibonite ($CaAl_2O_{19}$; Lodders and Fegley, 1999) that have

previously been identified as important presolar mineral phases (e.g., Choi et al. 1999; Zega et al. 2014). We hypothesize that oxides are an important carrier of s-process Hf in our investigated meteorites. The magnitude of s-process Hf enrichment within the residues of Murchison and Allende thus likely relates to the specific chemical nature and thus chemical resistivity of the major oxide minerals, presolar HfO_2 is now imbedded in or, alternatively, to the grain size of the s-process Hf carrier, with smaller oxide grains being dissolved preferentially in leachate 4, and larger grains being digested predominantly in the high-pressure dissolution step of the residues.

In summary, the presolar phase inventory of s-process nuclides in our studied meteorites most likely comprises several carrier phases, including mainstream SiC, silicates, and oxides, which not only differ in their composition but most likely also by their grain size.

Table 4: Measured and estimated Hf and W isotope signatures of leachates and residues, assuming that all observed Hf and W anomalies are caused by s-process enriched mainstream SiC. For further details of the mass balance considerations see main text.

	measured $\varepsilon^{183}W$	predicted $\varepsilon^{183}W$	Measured $\varepsilon^{180}Hf$	predicted $\varepsilon^{180}Hf$
Murchison[a]				
leach 1	1.11 ± 0.15	1.27	-	
leach 2	1.42 ± 0.20	1.27	-4.73 ± 0.12	-0.25
leach 3	0.29 ± 1.51	1.27	-2.70 ± 0.10	-0.25
leach 4	-0.64 ± 0.15	-0.42	2.49 ± 0.11	0.12
Residue	-2.53 ± 0.19	-2.59	2.28 ± 0.10	0.17
Allende[b]				
leach 1	1.00 ± 0.15	0.00	-	0.00
leach 2	0.32 ± 0.15	0.00	-2.05 ± 0.28	0.00
leach 3	0.34 ± 0.79	0.00	-0.29 ± 1.03	0.00
leach 4	0.06 ± 0.15	0.00	0.26 ± 0.10	0.00
Residue	-0.56 ± 0.33	0.00	0.54 ± 0.13	0.00

[a] 2.4 ppm W concentration in SiC ; 40% SiC dissolved within leachate 4 and 60% SiC in the residue.

[b] 2.4 ppm W concentration in SiC; 100% SiC dissolved in the residue.

III.4.5 Solar nebula processes vs. parent body alteration

As highlighted in section 4.4, several s-process Hf and W carrier phases seem to exist whereas r- and p-process Hf and W appear to have been isotopically equilibrated among solar system materials. Likewise, there is also evidence that in Allende and Kainsaz (chapter II), SiC has been destroyed selectively unlike oxides and unlike SiC in Murchison. Where and when these destructive processes acted thus becomes a pressing issue: on the respective parent body or within the solar nebula.

The lack of any r-or p-process Hf or W isotope heterogeneity in our data set of sequential dissolution steps, independent of petrologic grade (CM2.5 Murchison (Rubin et al., 2007); CO3.2 Kainsaz (Grossman and Brearley, 2005); CV>3.6 Allende (Bonal et al. 2006)) or matrix abundance (Murchison: ~ 60%; Kainsaz ~30%; Allende ~40%) may be in favor of a scenario of nebular processing. Possible host phases of r-and p-process Hf and W that condense after i.e., a massive star goes supernova or two neutron stars merge, likely are highly amorphous (Kemper et al. 2004). Consistent with a thermal nebular processing scenario, such amorphous material is more prone to recrystallize than crystalline s-process carriers (e.g., Gail, 2004; Harker and Desch, 2002). Admittedly though, also parent body alteration affects amorphous material more strongly than crystalline material and hence the abundance of amorphous silicates decreases significantly in chondrites that underwent aqueous or thermal alteration (e.g., Nagashima et al., 2005; Floss and Stadermann, 2012). In a solar nebula setting, r- and p-process carriers may have equilibrated isotopically within the parental molecular cloud before condensation of the first solid matter. A complete isotopic homogenization of r- and p-process Hf and W, however, is ruled out by the findings of p-process Hf and W isotope anomalies in CAIs (Peters et al., 2016). Thus, it remains ambiguous to what extent r- and p-process equilibration happened within the solar nebula or during parent body processing.

No clear-cut distinction between nebular and parent body processes arises from the information gained about presolar s-process carriers in the studied meteorites either. As shown in this study and chapter II, there is a discrepancy between Murchison, Allende, and Kainsaz: Whereas the overall range of $^{180}Hf/^{177}Hf$ in leachates and residues of Murchison, Kainsaz, and Allende spreads over ~7, ~7 and ~3 ε-units, respectively, those observed for $^{183}W/^{184}W$ are ~4.0, ~1.8 and ~1.6 ε-units, respectively. In particular for Kainsaz, a selective

destruction of the s-process carrier of W thus appears likely. Considering that s-process bearing mainstream SiC can dominantly reconcile the observed s-process W isotope variations in Murchison but is far from providing sufficient s-process material to explain the observed signatures in Allende, and Kainsaz (see chapter II), the observed discrepancy between Murchison, Allende, and Kainsaz with respect to s-process Hf and W most likely results from selective destruction of presolar s-process enriched SiC. The lack of W isotope heterogeneity on the bulk rock scale argues against a spatial inhomogeneity of s-process in the solar nebula. Hence, selective SiC destruction must have occurred either on parent bodies or, if it was a nebular process, no subsequent separation of secondary s-process W carriers from the local environment must have happened. Again, deciding between a nebular or parent body process is hard. For instance, Davidson et al. (2014) speculated that even during prolonged oxidation at low temperatures, SiC can form outer layers of unstable SiO_2, which can easily react with meteorite matrices. Given that both Allende and Kainsaz besides thermal alteration (see above) also show evidences for oxidation (e.g., Krot et al. 1995; Choi et al. 1997; Keller and Buseck, 1990; Imae and Kojima, 2000), it appears conceivable that SiC in these meteorites was predominantly destroyed relative to oxides but also that the thermally unaltered CM2 chondrite Murchison (see above) contains more SiC. This oxidation and thermal processing may also have redistributed W into secondary carriers and may provide an explanation why the s-process W isotope variation in leachates and residues of Allende and Kainsaz (see chapter II), in contrast to Murchison, is not dominantly controlled by SiC. Unfortunately, also nebular processes can result in physico-chemical effects such as oxidation and thermal processing: Evaporation of chondritic dust increases the fO_2 significantly Ebel and Grossman (2000) and Mendybaev et al. (2002) demonstrated that the absolute mass loss rate of SiC critically depends on the fO_2. Considering that the observed volatile depletion in CO and CV compared to CM chondrites (e.g., Anders, 1964; Huss et al., 2003; Bland et al. 2005) may reflect evaporation within the solar nebula, the selective SiC destruction in Kainsaz and Allende could also be attributed to nebular processes. It thus remains ambiguous to what extent the s-process Hf and W decoupling between Murchison, Kainsaz, and Allende occurred within the solar nebula or during parent body processes.

In summary, leachates and residues of Murchison, Kainsaz, and Allende are all characterized by isotopically homogeneous r-and p-process signatures. The smaller range of observed W isotope variation in Kainsaz and Allende relative to Murchison points to

pronounced selective destruction of SiC in the former meteorites. Both observations can be explained by both parent body processing and an intra-solar nebula processing scenario.

III.5 Conclusion

We here present high precision Hf and W isotope data including analyses of the rare p-process nuclides ^{174}Hf and ^{180}W for leachates, residues, and bulk samples of carbonaceous chondrites. No bulk rock Hf or W anomalies were found, but significant variations of s-process Hf and W was documented. In contrast, also the refined leaching procedures presented here, did not result in the selective enrichment or depletion of r- and/or p-process carrier phases.

New concentration data for Hf, W, Mg, Al, Ca, Ti, Cr, Fe, Co, Ni, and Zr in conjunction with mass balance calculations reveal that in contrast to s-process W, which primarily seems to be hosted in presolar mainstream SiC in the most primitive meteorite analyzed here (Murchison CM2), s-process Hf seems to be carried mainly by oxides, with mainstream SiC being of minor importance. For Allende and Kainsaz, secondary carriers of presolar W after redistribution from mainstream SiC appear of major importance.

The origin of the observed homogeneity of r- and p-process Hf and W nuclides and the whereabouts of the selective destruction of SiC in Kainsaz and Allende remain ambiguous and are either the result of parent body processing, solar nebular processing or a combination of both.

Chapter IV

Nucleosynthetic Zr isotope patterns of bulk rock and sequentially leached chondrite samples

IV.I Introduction

The history of the solar system started with the gravitational collapse of an interstellar molecular cloud with gas and dust supplied from extinct stars. Most of this material accreted to the sun with a small fraction (~1%) remaining to form the planets, their satellites, and other small objects. Many of these objects underwent significant parent body processing so that any nucleosynthetic heterogeneity was lost. However, primitive, i.e, type 1 to 3, chondrites do preserve nucleosynthetic within parent-body heterogeneity because they only experienced low degrees of thermal metamorphism or aqueous alteration. Thus, they retained at least parts of their presolar phase inventory (e.g., Huss et al., 2003; Davidson et al. 2014; Leitner et al., 2016). Direct measurements of presolar carrier phases are very challenging because they are usually quite rare (e.g., Huss and Lewis 1995, Ott 1993, Huss et al. 2003; Zinner et al. 2003) and very small < 3µm (e.g., Lewis et al. 1987; Choi et al. 1999). However, the presence of such phases can also be revealed by selective acid dissolution because of their differing resistivity to different acids and their markedly different isotopic signatures relative to those observed in terrestrial materials (e.g., Boato, 1954; Clayton et al., 1973; Lewis et al., 1987; Anders and Zinner, 1993; Nittler et al. 2005; Hoppe and Zinner, 2012). Sequential leaching of primitive meteorites is an established method to study the presence of variable amounts of isotopically anomalous carrier phases (e.g., Rotaru et al., 1992; Dauphas et al., 2002; Hidaka et al., 2003; Reisberg et al., 2009; Qin et al. 2011). The compositions deduced from these phases can then be used to characterize distinct nucleosynthetic contributions to the early solar system (e.g., McCulloch and Wasserburg, 1978; Rotaru et al., 1992; Podosek et al., 1997; Dauphas and Schauble, 2016).

In addition to isotope heterogeneity on the component scale, there is also evidence for isotope heterogeneity on bulk rock scale for several elements. For instance, mass-independent isotope heterogeneity was found on the bulk rock scale for O (e.g. Clayton, 1993), Ca (e.g. Simon et al., 2009), Ti (e.g., Trinquier et al., 2009), Cr (e.g., Rotaru et al., 1992), Ni (e.g., Regelous et al., 2008), Mo (e.g., Dauphas et al., 2002), Ru (e.g., Chen et al., 2010), and Ba (e.g., Ranen and Jacobsen, 2006). In contrast there seems to exist isotope homogeneity for other elements like Te on the bulk rock scale (e.g., Fehr et al., 2006), Hf (e.g., Sprung et al., 2010) and Os (e.g., Yokoyama et al., 2007, 2010). So far, there is no in depth understanding, why some elements are isotopically heterogeneous while others are not. At least two scenarios are favored: First, the uneven distribution of presolar material within the protosolar nebula, as for instance indicated by ^{50}Ti variations in carbonaceous chondrites, that scale with the

abundance of CAI's (Leya et al., 2008, 2009), or second, the selective processing of thermally unstable carrier phases (e.g., Trinquier et al., 2009).

Zirconium isotopes are excellent tools to address the issue described above because Zr is very refractory element (50% condensation temperature of 1750°C (Lodders et al. 2003) and, thus, is very insensitive to thermal processes that may have occurred within the early solar system. Moreover, Zr comprises isotopes that stem from different nucleosynthetic sources. All five stable Zr isotopes are mainly produced by the s- and r-process. The majority of the solar system abundance of ^{90}Zr (60%), ^{91}Zr (71%), ^{92}Zr (68%), and ^{94}Zr (84%) is thought to have formed by the s-process. In contrast, neutron-rich ^{96}Zr is to be produced mainly by the r-process (61%) (Bisterzo et al. 2014).

First sequential leaching experiments for Hf and W on the samples analyzed in this study revealed that isotope variations are carried by s-process material only (chapter III). Within chapters II and III it was also revealed that s-process Hf and W were carried by different carrier phases. For s-process W, several carrier phases including SiC were identified whereas oxide minerals were identified to be the dominant s-process Hf carrier phase. A pioneering leaching study for Zr by Schönbächler et al. (2005) was not able to determine what exactly the carrier phases of anomalous Zr are, and if the observed Zr isotope variation among leachates is due to the variation of s-process only or if additional r-process phases were also present. Moreover, the first comprehensive study on bulk rock samples by Akram et al. (2015) also revealed significant bulk rock anomalies, particularly for ^{96}Zr: These were suggested to be caused by an uneven distribution of material from at least three different nucleosynthetic sources. However, such correlations were previously not observed for Hf and W isotopes.

By comparing new Zr isotope data for leachates with our previous Hf and W data that was obtained from the exact same leachates (chapter III) and with previous bulk rock analyses of Zr (Akram et al. 2015), we address here the nature of possible carrier phases closer, potential implications for early solar nebula processes are discussed, and the possible stellar production sites of Zr, Hf and W isotopes are evaluated that can still be distinguished in primitive meteorites. To do so, we sequentially leached three different primitive carbonaceous chondrites (CM2 Murchison, CO3 Kainsaz and CV3 Allende) and analyzed the bulk rock isotope signatures of Kainsaz, Allende, NWA 3118 (CV3), NWA 2458 (L3) and El Hammami (H5).

IV.2 Methodology

The Zr isotope measurements were performed on Zr fractions obtained from the Murchison, Kainsaz and Allende leachates reported in chapter III. In brief, powdered rock samples (~5g) of Murchison (CM2), Kainsaz (CO3) and Allende (CV3) were sequentially digested using the following protocol:

1. 0.1 M HCl-0.001 M HF	1 day 20°C	"Leachate 1"
2. 4 M HNO3-0.001 M HF	5 days 20°C	"Leachate 2"
3. 6 M HCl-0.001 M HF	1 day 80°C	"Leachate 3"
4. 14 M HF-3 M HCl	3 days 120°C	"Leachate 4"
5. 1:1 HNO3-HF	3 days 180°C, teflon bombs	"Residue"
6. 3:1 HNO3- HF	4 days 180°C, teflon bombs	"Residue 2"

The samples were put through a combination of ion-exchange resins, a procedure that was developed to separate Hf and W from the remaining sample constituents (see chapter III). High field strength elements were separated from the rock matrices by using a combination of Cation resin Biorad AG50W×8 and anion resin Biorad AG1×8. Tungsten was then separated from Hf and Zr via Eichrom TEVA resin. Zirconium was finally purified and separated from Hf via Eichrom Ln-Spec resin using the protocol of Bast et al. (2015). All Zr cuts were purified on Eichrom Ln-Spec again to remove remaining Ti, Mo, and V repeating the protocol of Bast et al. (2015). Chemical yields for Zr were >70% and sufficiently low Mo/Zr and Ru/Zr below 0.001 and 0.01, respectively, were achieved, minimizing isobaric interferences on ^{92,92,96}Zr (Münker et al. 2001). We further checked all Zr analytes for impurities of Ti, Cr, V, and Fe, because of the tendency of these elements to form argides that can interfere on Zr masses (Schönbächler et al. 2004). Only samples with Ti/Zr <1, V/Zr < 0.3, Cr/Zr < 0.3, Fe/Zr < 0.9 were chosen for analysis. To oxidize residual organic compounds, every Zr fraction was digested repeatedly evaporated in aqua-regia and 9:1 HNO_3-H_2O_2. To demonstrate the viability of our ion-exchange procedure, two terrestrial rock samples (a La Palma Basalt (LP8), and an Ancient Gneiss Complex sample (AGC 351)), were processed alongside the leachate and residue samples and analyzed as well. Bulk rock samples of ~1g

were pulverized using an agate-mill and then digested following the digestion protocol in step 5 described above (from chapter III).

Zirconium isotope analyses were carried out on a Thermo Fisher Neptune Multicollector-ICPMS in the joint Köln/Bonn clean lab facilities using standard Ni sampler cones and H-type skimmer cones. Samples were introduced via a Cetac Aridus II nebulizer sample introduction system. Zirconium isotope measurements were performed in static mode, simultaneously collecting ion beams of masses 90 (90Zr), 91 (^{91}Zr), 92 (^{92}Zr, ^{92}Mo), 94 (^{94}Zr, ^{94}Mo), 95(^{95}Mo), 96 (^{96}Zr, ^{96}Mo, ^{96}Ru), 97 (^{97}Ru), 99 (^{99}Ru) and 100 (^{100}Ru) in Faraday cups. All Faraday cups, except those set on ^{90}Zr, ^{95}Mo, and ^{99}Ru were connected to $10^{11}\Omega$ amplifiers. For ^{90}Zr, a 10^{10} Ω amplifier, for ^{95}Mo and ^{99}Ru $10^{12}\Omega$ amplifiers were used. The ion beam intensities were normalized to the ^{90}Zr signal and corrected for instrumental mass bias relative to $^{94}Zr/^{90}Zr = 0.3381$ after an initial correction of the ^{94}Zr intensity for the isobaric interference from ^{94}Mo, normalizing $^{95}Mo/^{94}Mo$ to interference free $^{91}Zr/^{90}Zr = 0.21815$. In all cases, samples were bracketed by standard measurements and are reported as ε-unit deviations from the composition of the Zr Alfa Aesar standard solution (in parts per 10000). Sample and standard intensities were matched to within 10% to avoid possible intensity-related analytical bias. All analyses provided signal intensities of >3V for the minor isotope ^{96}Zr. External reproducibilities (2 S.D.) are given by repeated measurements of the bracketing standard and were typically better than ±120 ppm for ε^{96}Zr, ±35 ppm for ε^{92}Zr, and ca. ±40 ppm for ε^{91}Zr. Total blanks were below 1 ng Zr in all cases and are thus insignificant compared to the amount of Zr within each sample.

Zr concentrations of the different leachates and residues of Murchison and Allende were determined on the same aliquots as in chapter III using the same techniques describe therein. Kainsaz leachate and residue Zr concentration data has not been determined.

IV.3 Results

IV.3.1 Concentration results

Zirconium concentration data are displayed in Fig. 1 and given in Table 1. In summary, Leachates 1 do not contain any Zr, neither for Murchison, nor for Allende. Leachates 2, 3, 4 of Murchison contain 21%, 21 %; and 23 % of the total Zr released. In the case of Allende

leachate 2, 3 and 4 contain 10%, 25 %, and 27% of the Zr. The residues of Murchison and Allende contain 35 % and 38 % of the total Zr released.

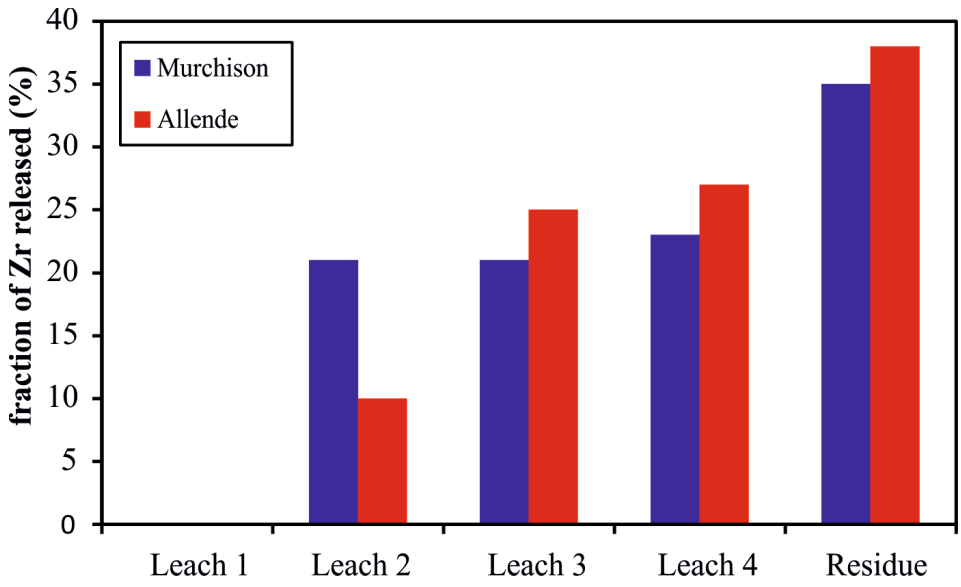

Figure 1: Relative Zr yields of the leachates and residues of Murchison and Allende. In blue: Murchison; in red: Allende.

IV.3.2 Isotope results

All Zr isotope results are expressed in ε-units are shown in table 1 and figures 2 a, b, c and 3 a, b, c. In general, first leachate steps tend to show positive ε^{9i}Zr (i.e., $\varepsilon^{91,92,96}$Zr), whereas later leachate steps or residues show negative ε^{9i}Zr. For instance, leachate 2 of Murchison shows an ε^{96}Zr of ca. +30 whereas the corresponding residue shows a ε^{96}Zr of ca. -13. The same general trends are observed for Kainsaz and Allende. However the general magnitude of the observed isotopic deviations from the Alpha Aesar Zr standard follow the order Murchison > Kainsaz > Allende. Note that leachates 1 of Murchison and Allende as well as Kainsaz residue 2 only contained Zr at blank levels and are thus not considered any further.

The bulk rock samples analyzed in this study usually do not show resolvable ε^{91}Zr and ε^{92}Zr isotope anomalies but instead significant, resolvable ^{96}Zr isotope anomalies. The largest ε^{96}Zr deviation from the terrestrial Zr isotope composition was detected for Allende (1.09±0.20), the smallest for EL Hammami (0.28±0.20). Given that (i) both terrestrial samples (LP 8 and AGC 351) show terrestrial Zr isotopic signatures within analytical uncertainty and

(ii) the Zr isotope signatures of extraterrestrial whole rock samples as calculated from mass balance and the measured Zr isotope signatures of leachate and residue steps agree with the measured bulk rock data, our data are considered robust.

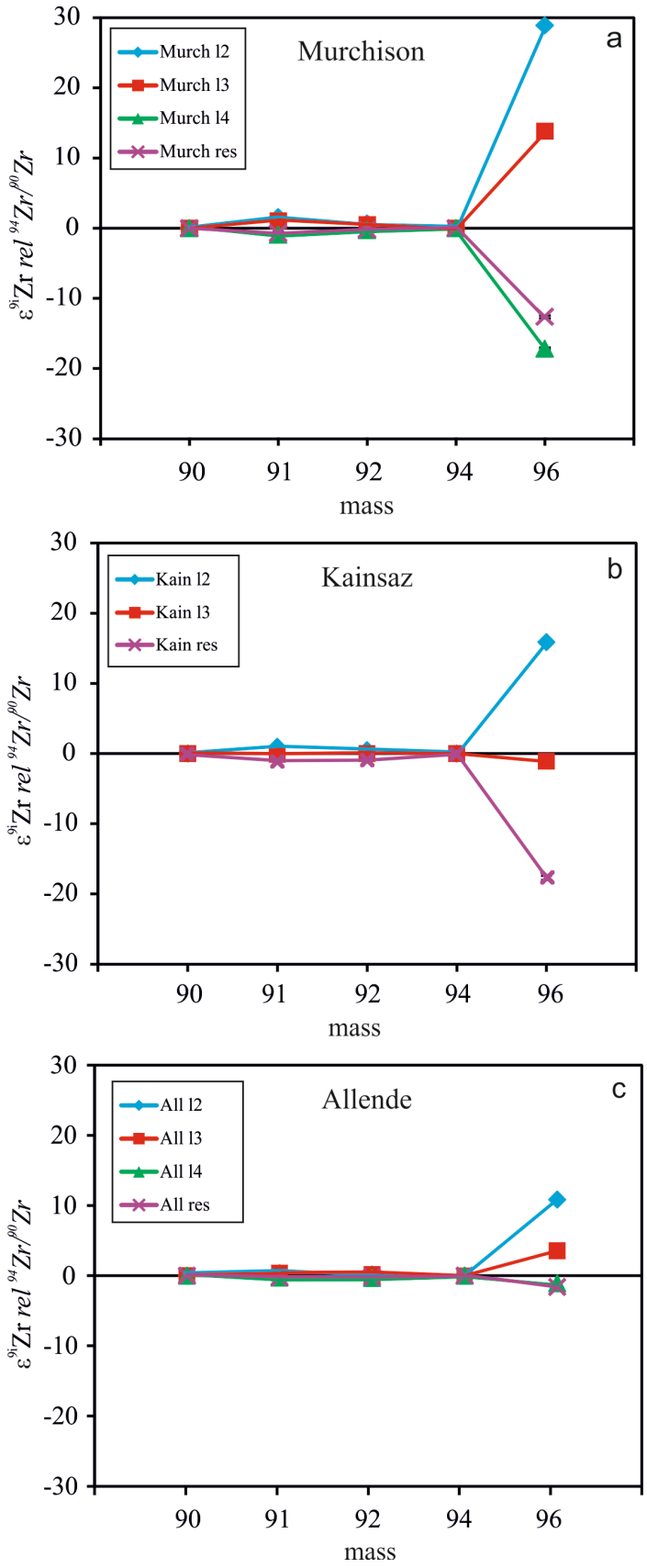

Figure 2: Zr isotope patterns of leachate and residue steps of Murchison (a), Kainsaz (b), and Allende (c). Blue: leachate 2; red: leachate 3; green: leachate 4; purple: residue. Uncertainties on the isotope ratios are given as the 2SD of repeated measurements of the bracketing standards matched to the individual samples.

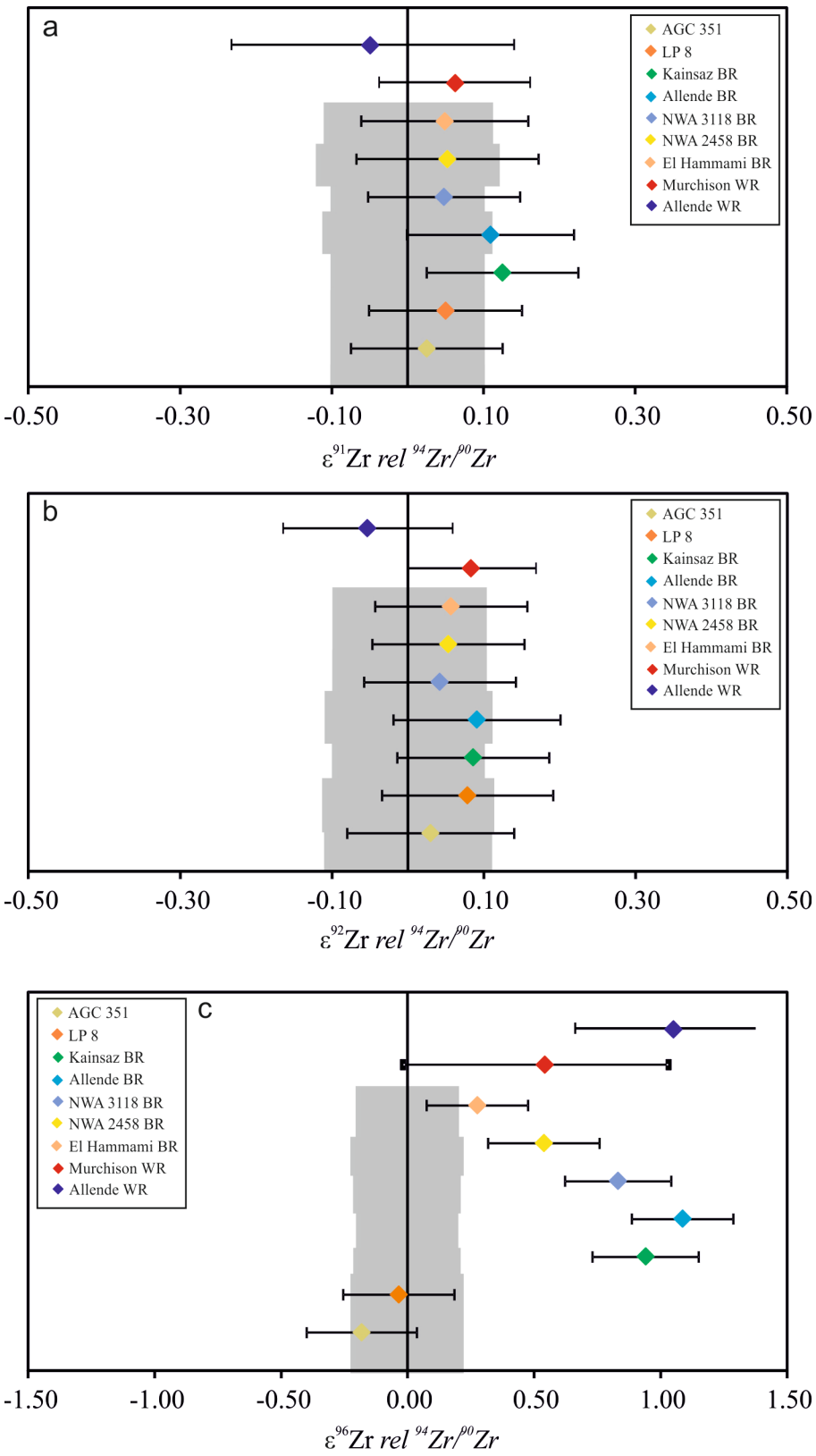

Figure 3: ε^{91}Zr (a), ε^{91}Zr (b) and ε^{96}Zr (c) signatures of the bulk rock samples normalized relative to ^{94}Zr/^{90}Zr. Different colors represent different meteorites. In grey, 2 S.D. external reproducibly of the Zr solution standard of the analytical session. For Murchison and Allende calculated whole rock of the different leachates and residues are included. Reported uncertainties for samples are given as the 2SD of repeated measurements of the bracketing standards matched to the individual samples.

Table 1: Zr data for the analyzed bulk rock and sequentially leached samples

sample	fraction Zr released (%)	$\varepsilon^{91}Zr^{b}$	$\varepsilon^{92}Zr^{b}$	$\varepsilon^{96}Zr^{b}$
		mass bias rel $^{94}Zr/^{90}Zr$		
Murchison		0.06 ± 0.09	0.08 ± 0.08	0.52 ± 0.55
Leachate 1	0	blank	blank	blank
Leachate 2	21	1.56 ± 0.17	0.65 ± 0.13	28.86 ± 0.19
Leachate 3	21	1.03 ± 0.14	0.52 ± 0.12	13.79 ± 0.15
Leachate 4	23	-0.93 ± 0.19	-0.41 ± 0.15	-17.20 ± 0.18
Residue	35	-0.73 ± 0.18	-0.21 ± 0.16	-12.65 ± 0.19
Kainsaz				
Leachate 1	tbd[a]	tbd	tbd	tbd
Leachate 2	tbd[a]	0.96 ± 0.22	0.48 ± 0.17	15.86 ± 0.21
Leachate 3	tbd[a]	-0.14 ± 0.19	-0.02 ± 0.14	-1.11 ± 0.19
Residue	tbd[a]	-0.81 ± 0.21	-0.43 ± 0.24	-17.7 ± 0.29
Residue 2	0	blank	blank	blank
Allende		-0.05 ± 0.15	-0.06 ± 0.11	1.05 ± 0.34
Leachate 1	0	blank	blank	blank
Leachate 2	10	0.36 ± 0.19	0.16 ± 0.20	10.84 ± 0.28
Leachate 3	25	0.35 ± 0.40	0.16 ± 0.35	3.54 ± 0.50
Leachate 4	27	-0.29 ± 0.21	-0.14 ± 0.17	-1.09 ± 0.24
Residue	38	-0.25 ± 0.15	-0.21 ± 0.11	-1.65 ± 0.15
<u>Bulk analyses</u>				
Kainsaz		0.13 ± 0.10	0.09 ± 0.10	0.94 ± 0.21
Allende		0.11 ± 0.11	0.09 ± 0.11	1.09 ± 0.20
NWA 3118		0.05 ± 0.10	0.04 ± 0.10	0.83 ± 0.21
NWA 2458		0.05 ± 0.12	0.05 ± 0.10	0.54 ± 0.22
El Hammami		0.05 ± 0.11	0.06 ± 0.10	0.28 ± 0.20
<u>terrestrial</u>				
AGC 351		0.03 ± 0.10	0.03 ± 0.11	-0.18 ± 0.20
LP 8		0.05 ± 0.10	0.08 ± 0.11	-0.04 ± 0.20

[a] tbd refers to "to be determined"

[b]. Uncertainties on the isotope ratios are given as the 2SD of repeated measurements of the bracketing standards matched to the individual samples. Uncertainties on calculated bulk rocks are given by the error propagated 2SD of the individual variables (concentration, isotope signature) using Monte Carlo Simulation (Sprung et al. 2013).

IV.4 Discussion

IV.4.1 Comparison with previous studies

Data for leachate and residue steps of this study generally display negative Zr isotope anomalies in first leaching steps, with complementary positive Zr isotope variations in later leachate steps and the residue step. The same trends have also been observed in a previous study of leachate and residue fractions of Orgueil, Murchison, and Allende (Schönbächler et al. 2005). In addition to this qualitative agreement, also the relative magnitude of coupled anomalies in ε^{91}Zr, ε^{92}Zr, and ε^{96}Zr reported here agree with those of previous reports (Schönbächler et al., 2005): In ε^{91}Zr vs. ε^{96}Zr and ε^{92}Zr vs. ε^{96}Zr space, the data of these authors define slopes of 0.058±0.003 and 0.023±0.001, respectively, that are identical to those defined by our study (0.057±0.009 and of 0.025±0.006, respectively, figures 4 and 5). This consistency of the Zr isotope data between the two studies implies that the different leaching protocols lead to the selective enrichment or depletion of similar carrier phases in leachate and residue steps. Moreover, the good match amongst calculated and actually measured bulk rock Zr isotope signatures insinuate that all anomalous carrier phases have been sampled, i.e., complete sample dissolution has been achieved during the course of our sequential dissolution experiments.

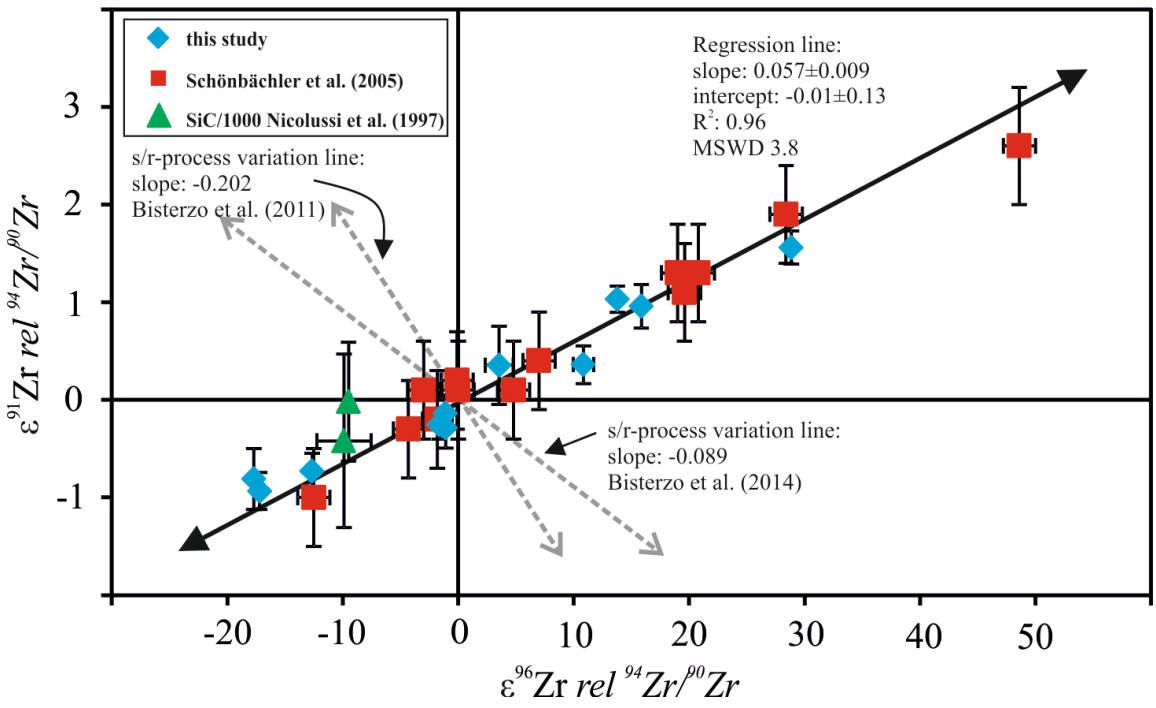

Figure 4: ε^{91}Zr vs ε^{96}Zr of leachate and residue steps from this study in blue and those of Schönbächler et al. (2005) in red. The data of the two studies are in very good agreement but different trajectories would be associated with excesses or deficits in an s-process Zr component according to the astrophysical models of Bisterzo et al. (2011; 2014) in grey. In green SiC data of Nicolussi et al. (1997). The regression line is calculated by using IsoPlot 4.13.

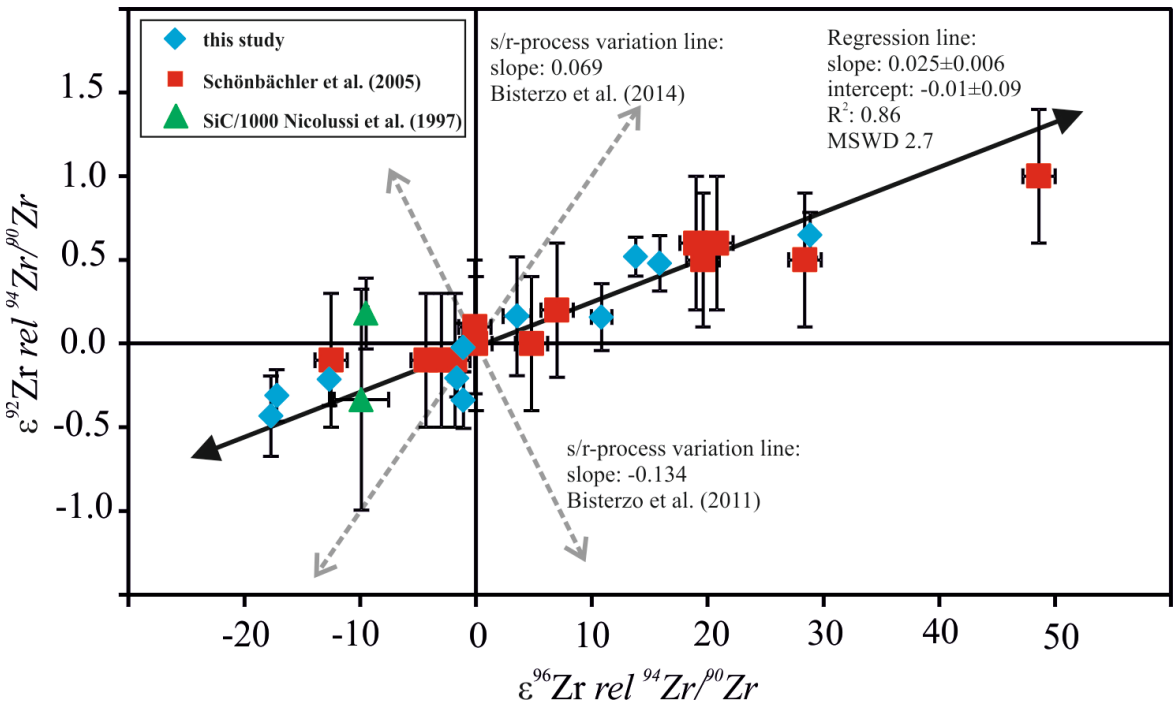

Figure 5: ε^{92}Zr vs ε^{96}Zr of leachate and residue steps from this study in blue and those of Schönbächler et al. (2005) in red. The data are in very good agreement but different trajectories would be associated with excesses or deficits in an s-process Zr component according to the astrophysical models of Bisterzo et al. (2011; 2014) in grey. In green SiC data of Nicolussi et al. (1997). The regression line is calculated by using IsoPlot 4.13.

However, it should be noted that our bulk rock data display coupled trends in $\varepsilon^{91}Zr$, $\varepsilon^{92}Zr$, and $\varepsilon^{96}Zr$ signatures that are different from those reported by Akram et al. (2015). These authors reported positive $\varepsilon^{96}Zr$ in their analyzed set of whole rock samples that are generally associated with negative $\varepsilon^{91}Zr$ and $\varepsilon^{92}Zr$. Our bulk rock data instead show a slightly positive correlation of $\varepsilon^{96}Zr$ and $\varepsilon^{91}Zr$, $\varepsilon^{92}Zr$ (Figures 6 and 7). In addition and in contrast to the data of Akram et al. (2015) the bulk rock data of the meteorites analyzed in this study, also seem to plot on the leachate regression line whereas the data of Akram et al. (2015) plots significantly below the leachate regression line within $\varepsilon^{91}Zr$ vs. $\varepsilon^{96}Zr$ and $\varepsilon^{92}Zr$ vs. $\varepsilon^{96}Zr$ spaces (Fig. 6 and 7). This discrepancy implies a slight bias in the $\varepsilon^{91}Zr$, $\varepsilon^{92}Zr$ values reported in one of the two studies. It should be of note here that for consistency, all bulk rock data were gained during the same rounds of ion-exchange chemistry and in the same measurement sessions as the leachate and residue data, which is consistent with previous studies (see above). Moreover, almost all of the analyzed terrestrial standards of Akram et al. (2015) tend to show slightly negative $\varepsilon^{91}Zr$ and $\varepsilon^{92}Zr$. As a result, the calculated Earths mean ε^{91} and $\varepsilon^{92}Zr$ analyzed by Akram et al (2015) are -0.07±0.02 and -0.06±0.02, respectively. Given that our data for terrestrial rocks (Table 1; Figure 6 and 7) exhibit no such bias, we conclude that the data set of Akram et al. (2015) is affected by slight analytical problems on ^{91}Zr and ^{92}Zr.

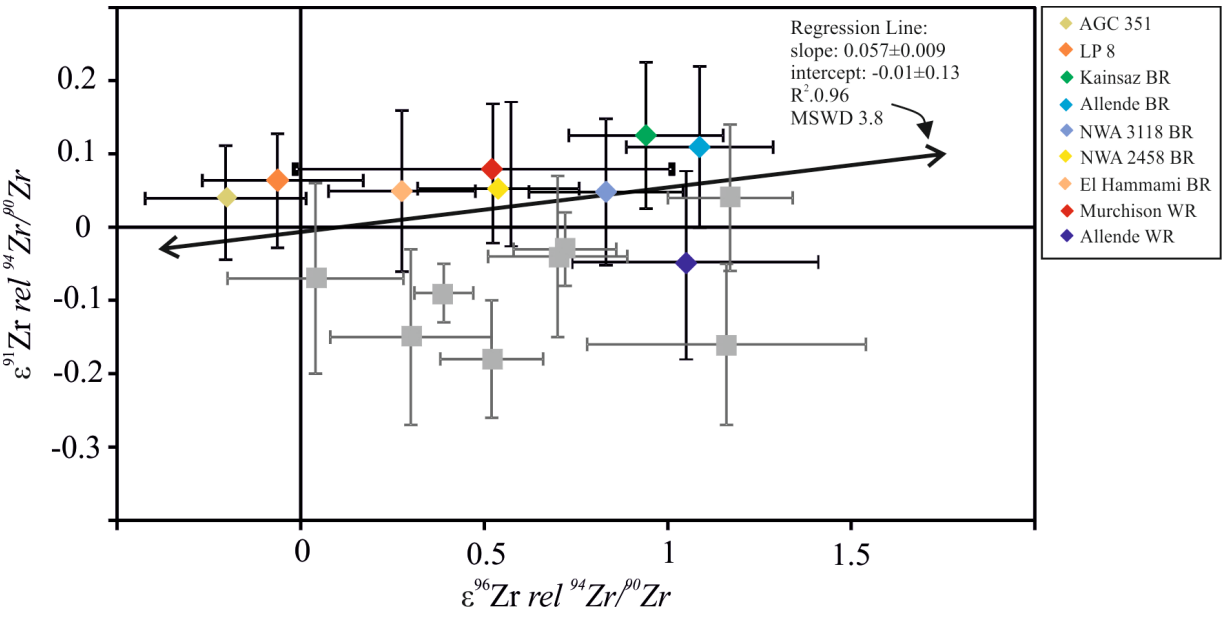

Figure 6: $\varepsilon^{91}Zr$ vs $\varepsilon^{96}Zr$ of the bulk rock samples. Our analyzed bulk rock samples are in good agreement with the leachate regression. The data of Akram et al. (2015) (in grey) appear to be biased in $\varepsilon^{91}Zr$ and plot below the regression line (black line).

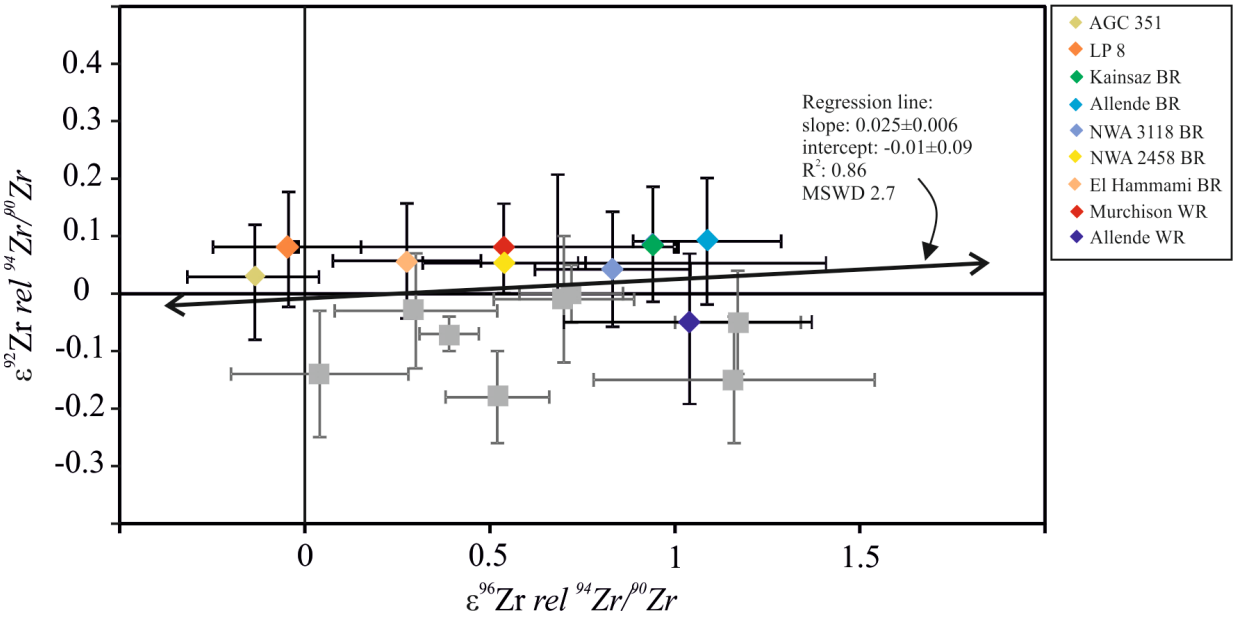

Figure 7: ε^{92}Zr vs ε^{96}Zr of the bulk rock samples. Our analyzed bulk rock samples are in good agreement with the leachate regression. The data of Akram et al. (2015) (in grey) appear to be biased in ε^{92}Zr and plot below the regression line (black line).

IV.4.2 Cause of the Zr isotope variation among leachates

As pointed out in the previous section, the Zr data obtained for the leachate and residue steps define slopes of 0.057±0.009 and 0.025±0.006 in ε^{91}Zr vs ε^{96}Zr and ε^{92}Zr vs ε^{96}Zr space, respectively. Moreover, the data are also well correlated showing MSWDs of 3.8 and 2.7, indicating that all samples follow the same distinct trends. This trend cannot be caused by cosmic ray effects as pointed out in chapter III because the leachate and residue steps of Murchison, Kainsaz and Allende do not follow characteristic, correlated ε^{178}Hf and ε^{180}Hf variations indicative of neutron capture effects (Sprung et al., 2010; 2013; Peters et al., 2016). Given that neutron capture cross sections and resonance integrals of Zr isotopes are significantly smaller than those of the relevant Hf isotopes (http://wwwnds.iaea.org/exfor/endf.htm) neutron capture effects can be excluded to cause the observed correlation amongst Zr isotope anomalies.

By comparing the Zr isotope leachate data with astrophysical models of Bisterzo et al. (2011) and Bisterzo et al. (2014), it is evident that the Zr leachate data are at odds with predicted s/r-process variations lines. The slopes predicted for s/r-process variation in ε^{91}Zr vs ε^{96}Zr and ε^{92}Zr vs ε^{96}Zr spaces are -0.202; -0.089 and -0.134; 0.069, respectively (Figure 6 and 7) whereas those observed from our regressions are 0.057±0.009 and of 0.025±0.006.

However, a comparison of the Zr isotope signatures of the sequential dissolution steps of Murchison, Kainsaz, and Allende with the Hf and W isotope signatures of the same fractions (chapter III) reveals a very close link between the Zr and Hf isotope anomalies and a somewhat looser link with W isotope anomalies (Figure 8 and 9). Thus, taking into account that Hf and W isotope variations are caused by s-process material only (chapter III), the correlations between Hf and Zr and the covariation between W and Zr provide evidences that the observed Zr isotope variations are also caused by the uneven distribution of an s-process carrier phase in the steps of our sequential dissolution scheme. Given that s-process Hf and W are dominated by low mass AGB star material (>98%; e.g., Bisterzo et al. 2014), the Zr isotope variation among the steps of our sequential dissolution scheme most likely reflects variations in contributions of low mass AGB star material as well. This is also consistent with more elaborate nucleosynthetic models for Zr isotopes that consider AGB stars of different initial mass in more detail (Akram et al. 2015). These models reveal that the leachate Zr isotope data actually require low-mass AGB ($\leq$ 3 solar masses) star material to be present in acid-resistant carrier phases within the analyzed meteorites. In AGB stars of higher mass, a neutron-dense neutron burst from the $^{22}Ne(\alpha,n)^{25}Mg$ reaction would overproduce ^{91}Zr in particular (Akram et al., 2015). Thus, Zr isotopes provide powerful support for the conclusion of Bisterzo et al. (2014) that low-mass AGB stars synthesized an important amount of the s-process budget in our solar system, some of which is still hosted in its primary acid-resistant carrier phases within the analyzed meteorites. Interestingly, Zr and Hf isotope anomalies fall on one linear trend which implies near-uniform and near-chondritic Zr/Hf of the presolar component and the presolar-component-depleted matrix, because otherwise, curved trajectories would be expected (DePaolo & Wasserburg, 1979).

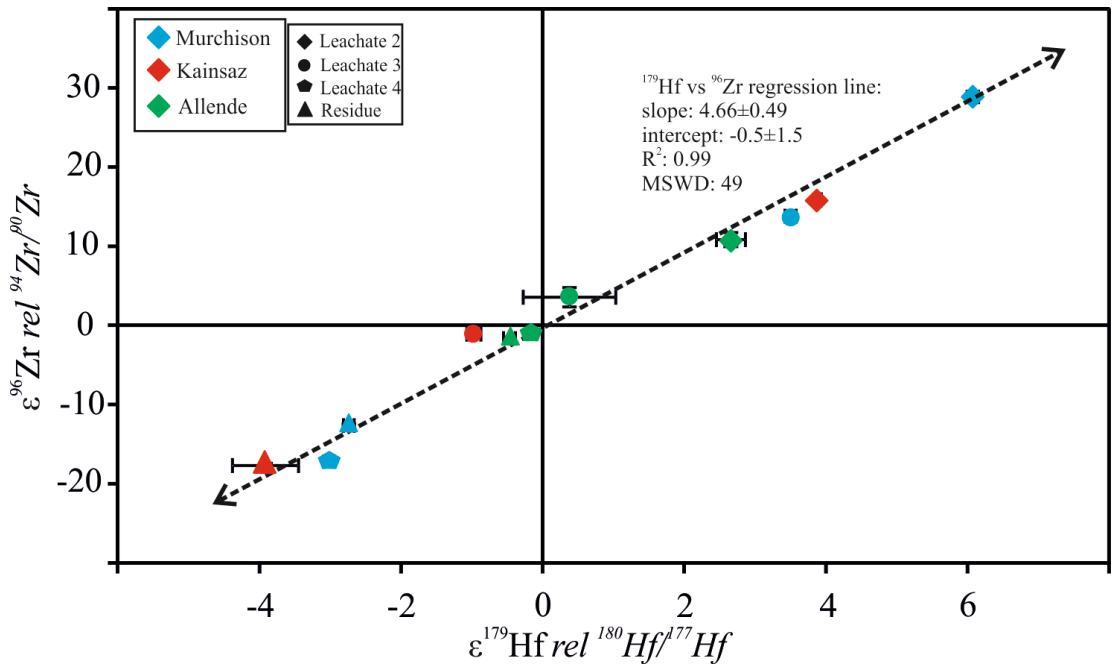

Figure 8: ε^{179}Hf vs ε^{96}Zr of the leachates of Murchison, Kainsaz and Allende. As discussed in detail in chapter III, 'rel ^{180}Hf/^{177}Hf" implies an internal correction for mass bias normalizing to an assumed terrestrial ^{180}Hf/^{177}Hf of 1.8868. The observed anomalies are correlated indicating that Zr isotope variations are similar to variations in Hf (chapter III) and must be caused by an uneven distribution of s-process carrier phases in the different steps of the sequential dissolution and that these Hf and Zr carrier phases most likely are identical. The regression line is calculated by using IsoPlot 4.13.

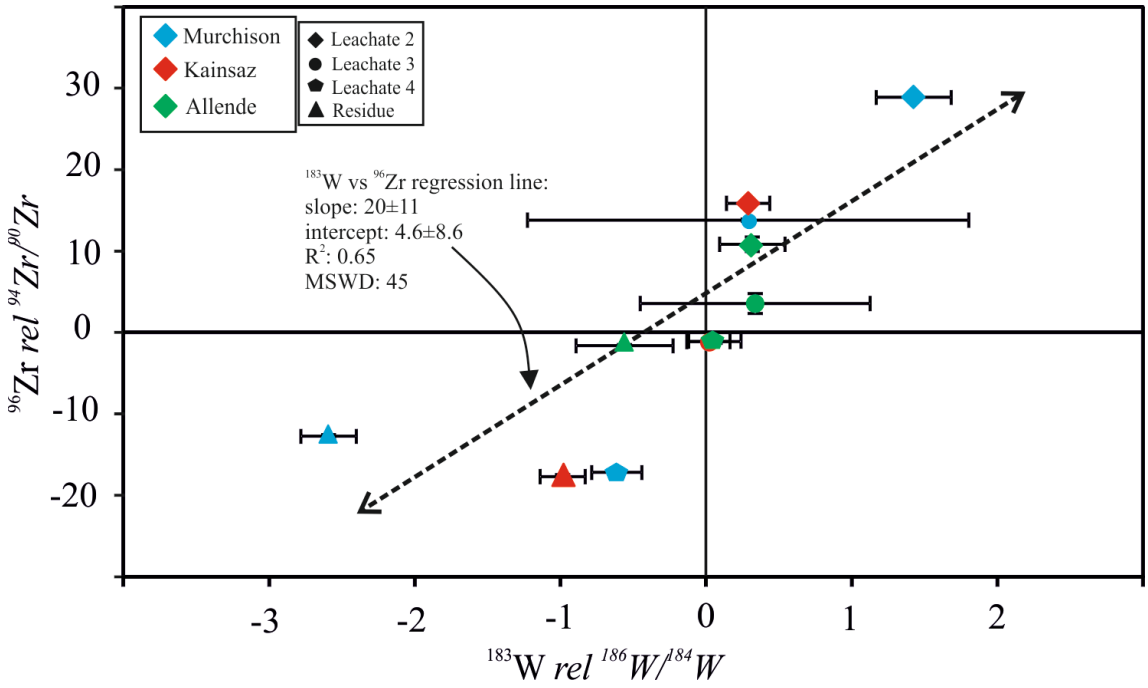

Figure 9: ε^{183}W vs ε^{96}Zr of the leachates of Murchison, Kainsaz and Allende. As discussed in detail in chapter III, 'rel ^{186}W/^{184}W' implies an internal correction for mass bias normalizing to an assumed terrestrial ^{186}W/^{184}W of 0.9277. The data are less correlated than Hf-Zr data but still indicate that Zr isotope variation is similar to variations of W isotopes (chapter III) that are caused by the uneven distribution of s-process carrier phases, although W and Zr carrier phases are different. The regression line is calculated by using IsoPlot 4.13.

Additional complexity might be caused by the presence of additonal s-process material from different-sized AGB stars. For instance, Akram et al. (2015) concluded based on astrophysical modelling that the in section 4.1 described offset between their bulk rock and leachate data is due to the presence of additional intermediate-mass AGB star material, which is not resolved during sequential leaching but present at bulk rock scale. However, as discussed in section 4.1, the ^{91}Zr and ^{92}Zr data that lead to this conclusion are likely more biased than recognized by the original authors themselves Akram et al. (2015). All our bulk rock data, in contrast, do plot on the leachate regression lines. Both, whole rock and leachate data thus comprehensively cover the entire isotopic budget of Zr and no further s-process material needs to be added to explain the composition of whole rocks and individual components.

Both this study and that of Akram et al. (2015) highlight the importance of considering the actual astrophysical parameters of possible stellar s-process nucleosynthesis rather than assuming that the "s-process" is a uniform entity. We hypothesize that the near-chondritic Zr/Hf value of the presolar component that is isolated by our leaching experiments should provide an important constraint for astrophysical models that seek identify and reproduce the latest additions of nucleosynthetic material to the solar system in addition to pure isotopic constraints.

In summary, the observed Zr isotope variations between the different leachates and residues are caused by variations of low mass AGB star material. Our data do not support additional overlapping s-process heterogeneities involving additional material intermediate-mass AGB stars on the bulk rock scale.

IV.4.3 Carrier phases of anomalous Zr

As discussed above, Zr isotope variations revealed by sequential leaching are most likely caused by variable proportions of s-process material. S-process-enriched mainstream SiC is dominantly characterized by ^{96}Zr deficits (e.g., Nicolussi et al. 1997). Due to their high chemical resistance, SiC grains accumulate in the later leaching steps and residues of sequential leaching experiments. As expected for mainstream SiC-enriched steps of the sequential dissolution, leachates 4 and residues analyzed in this study all show deficits in ^{96}Zr. However, similar to our conclusion for Hf (see chapter III) mainstream SiC alone cannot

account for the observed s-process enrichments at least in Murchison and Allende, because the total amount of s-process Zr provided by mainstream SiC simply is too low, even if it is assumed that all SiC grains are s-process enriched instead of mainstream grains only, judging from SiC abundances of Huss et al. (2003), i.e., Murchison = 13.5 ppm, Allende = 0.01 ppm, and a Zr concentration within mainstream SiC of 140ppm (Amari et al. 1995). Silicon carbide can only account for ~45% of total s-process causing the anomalies in Murchison and only ~0% for the total s-process causing the anomalies in Allende. For Kainsaz no Zr concentration data for the leachates and residues were obtained so far, thus no mass balance calculations were performed. Similar to Hf, Zr is predicted to condense either as carbide or oxide depending on the whether the parent star is characterized by C/O > 1 or C/O <1 (Lodders and Fegley, 1995; Lodders and Fegley, 1999). Thus, given that oxides have been proposed as the dominant s-process Hf carrier phase (chapter III), it is very likely that Zr in Murchison, Kainsaz and Allende is likely carried by the same carrier phases. CAI's are also known to be present within the samples analyzed in this study (e.g., Hezel et al. 2008) and have been demonstrated to show singinificant nucleosynthetic Zr isotope varaitions (Akram et al. 2013). However, CAIs are only of minor importance for Zr isotope anomalies, and their presence cannot have caused the correlated trends of Zr isotope anomalies that are formed by data for leachates and residues. This is because CAIs mainly comprise chemically resistant minerals, like spinel or perovskite (e.g., MacPherson et al. 1988) that are most likely enriched in residue fractions. However, the ε^{96}Zr of CAIs is markedly positive (Akram et al. 2013) which contrasts the ^{96}Zr depleted the composition of stronger leachates and residues (Table 1). Thus, the observed Zr isotope variation between the different steps of our sequential dissolution procedure is most likely caused by the uneven distribution of oxide grains and a minor SiC component. These phases carry both, s-process Hf and s-process Zr.

IV.4.4 Cause of the observed Zr bulk rock isotope variation

A major remaining issue is the ultimate cause of bulk rock Zr isotope anomalies, given the terrestrial Hf and W isotope compositions of the analyzed meteorites. Considering that Hf and Zr most likely share common presolar carrier phases, an inhomogeneous distribution of such phases is unlikely to have caused resolvable Zr isotope anomalies but not anomalies in Hf isotopes. For instance, considering the good correlation of ε^{96}Zr and ε^{179}Hf of leachates,

the observed ε^{96}Zr of +1.09 ± 0.20 of Allende should translate into an ε^{179}Hf of ca. +0.23 (ε^{179}Hf= ε^{96}Zr/4.66) for Allende, which is analytically resolvable but not observed (Chapter II). Even if a most conservative calculation is performed using the lower bound in ε^{96}Zr and the steepest slope permitted by the leachate regression (i.e., ε^{179}Hf= 0.89/5.15), the inferred ε^{179}Hf signature of Allende would still be +0.17, thus still being inconsistent with an observed ε^{179}Hf of -0.08 ± 0.09 of Allende (Chapter II). Thus, a heterogeneous distribution of s-process carrier phases can be excluded as cause for the bulk rock ε^{96}Zr anomalies. Thus, a heterogeneous distribution of r-process Zr but not Hf remains the only viable explanation. In agreement with Sprung et al. (2010) and Akram et al. (2013) an important implication hereof is that this anomalous Zr cannot have been hosted by the same carrier phase as r-process Hf. In CAIs, Akram et al. (2013) observed resolvable, positive ε^{96}Zr values that could in principle point to an excess of r-process Zr over s-process Zr in CAIs relative to Earth, whereas the negative ε^{179}Hf of the same CAIs – with only one exception – implied a deficit of r-process Hf. They interpreted this feature as a result of CAI's having sampled different carrier phases of "r-process" Hf and Zr. In fact, because of the almost identical geochemical and very similar cosmochemical properties of Hf and Zr, a separate synthesis of neutron-rich ("r-process") Hf and Zr was previously suggested (Sprung et al., 2010; Akram et al., 2013). This suggestion was further backed up by a model of charged particle reaction that dominantly occur in high entropy wind environments of Type II supernovae and which do synthesize ^{96}Zr but not Hf. The most plausible option, thus seems that the observed bulk rock Zr anomalies most likely are caused by a heterogeneous distribution of a phase that hosts charged-particle-synthesized "r-process" Zr but no Hf.

Most likely, CAIs make up at least a part of the phases that cause the observed apparent r-process or, rather, charged-particle-synthesized Zr heterogeneity on the bulk rock scale. Based on Zr concentration data in CAI's (Mason and Tyler, 1982) and CI chondrites (Lodders et al. 2003), Zr isotope signatures of CAI's (Akram et al. 2013) and the variable CAI abundance in different chondrite classes (Hezel et al., 2008), Akram et al. (2015) showed that the observed positive bulk rock anomalies of CV, CM, CO, and CK chondrites are fully reproduced by an addition of CAI material to CI chondritic material. Such a scenario is hard to evaluate for Hf or W, because Hf and W concentrations as well as observed Hf and W isotope variations in CAI's are too low to have substantial leverage (Sprung et al. 2010; Akram et al. 2013; Kruijer et al. 2014). For instance, applying the mass balance approach of

Akram for, i.e., W isotopes in Allende using CAI abundances of Hezel et al. (2008), mean W concentrations of ~0.6 ppm and a weighted mean $\varepsilon^{183}W$ of ~0.56 (both from Kruijer et al. 2014), CI chondrite W contents of 93 ppb (Lodders et al. 2003), and $\varepsilon^{183}W = 0$ for CI (e.g., Kleine et al., 2004), Allende would be expected to exhibit an $\varepsilon^{183}W$ of +0.10, which is barely resolvable given typical analytical uncertainties for $\varepsilon^{183}W$ (e.g., chapter II; Becker et al. 2015; Budde et al, 2015; Holst et al. 2015). Moreover, the observed bulk rock Zr isotope signature of Orgueil (Akram et al. 2015) and of ordinary chondrites (this study; Akram et al. 2015) cannot be explained by the presence of CAIs because neither Orgueil nor ordinary chondrites do contain significant amounts of CAIs (e.g., Hezel et al. 2008; Scott and Krot, 2006). Unless this low CAI abundance is a secondary effect, which seems unlikely given the primitive nature of Orgueil (e.g., DuFresne and Anders, 1962; Huss and Lewis, 1995) and some ordinary chondrites (e.g., L3 NWA 2458 (Conolly et al., 2006)), another carrier of apparent r-process Zr must exist. This carrier must either have been thermally processed to different degrees before parent body accretion took place, or this apparent r-process Zr heterogeneity was an inherited feature and, thus, a true effect of an inhomogeneous solar nebula.

Parent body processing under open system conditions, which could also potentially mimic indigenous nucleosynthetic anomalies, cannot explain the Zr isotope anomalies on the bulk rock scale because the magnitude of $\varepsilon^{96}Zr$ appears to be independent of petrologic grade. For instance, Allende (CV) has a $\varepsilon^{96}Zr$ of 1.09±0.20 and a thermal grade of >3.6. El Hammami (H) has petrologic grade of 5 and shows a smaller $\varepsilon^{96}Zr$ of 0.28±0.20. In contrast, CO3.2 Kainsaz and CM2 Murchison show $\varepsilon^{96}Zr$ of 0.94±0.21 and 0.73±0.16 (Akram et al., 2015). Thus, the observed bulk rock anomalies, most likely represent a combination of variable CAI abundances (Akram et al., 2015) and the heterogeneous distribution of an apparent r-process Zr-bearing phase.

In summary, the absence of nucleosynthetic Hf isotope anomalies on the bulk rock scale in meteorites and the presence of such anomalies for Zr strongly imply a heterogeneous distribution of apparent r-process or, rather, charged-particle-synthesized Zr. This heterogeneous distribution likely relates to variable CAI abundances in different chondrite groups and either the thermal processing of a labile “r-process” Zr phase or a truly spatial inhomogeneity of the solar nebula with respect to such a phase.

IV.5 Conclusion

Our study presents high precision Zr isotope data for bulk rock meteorite samples and sequentially dissolved chondrite samples. We document resolved and well-correlated ε^{91}Zr, ε^{92}Zr, and ε^{96}Zr values for different steps of the sequential dissolution procedure. For bulk rock meteorite samples, well-resolved and significant ε^{96}Zr anomalies are reported.

For leachate and residues, Zr isotope anomalies tend to be correlated with Hf and W isotope anomalies and, thus, are likely caused by an uneven distribution of s-process material in the different dissolution steps. The strong correlation particularly of Hf and Zr isotope anomalies in leachates and residues indicates that the s-process carriers of Hf and Zr are essentially the same, namely predominantly oxides and to a minor degree SiC.

Observed Zr isotope anomalies on the bulk rock scale are most likely caused by the heterogeneous abundance of CAIs in different meteorite groups as well as an inhomogeneous distribution of apparent r-process material that may be charged-particle synthesized and is hosted in yet another, so far unidentified phase.

The good agreement of bulk and leachate Zr isotope data and their disagreement with the classical astrophysical models of s-process nucleosynthesis (e.g., Bisterzo et al., 2011, 2014) clearly shows that such astrophysical models require revision, with Akram et al. (2015) model of initial mass-sensitive s-process yields of AGB stars seeting a promising example.

V. References

Akram W., Schönbächler M., Bisterzo S. and Galino R. (2015) Zirconium isotope evidence for the heterogeneous distribution of s-process materials in the solar system. Geochimica et Cosmochimica Acta 165, 484-500.

Akram W., Schönbächler M., Sprung P. and Vogel N. (2013) Zirconium-Hafnium Isotope evidence from meteorites for the decoupled synthesis of light and heavy nuetron rich Nuclei. Astrophysical Journal 777, 169-181.

Alpher R.A., Bethe H and Gamow G. (1948) The origin of chemical elements. Physical Review 73, 803-804.

Amari S., Anders E., Virag A. and Zinner E. (1990) Interstellar graphite in meteorites. Nature 345, 238-240.

Amari S., Hoppe P., Zinner E., and Lewis R. S. (1995) Trace-element concentrations in single circumstellar silicon carbide grains from the Murchison meteorite. Meteoritics 30, 679–693.

Amari S., Gao X., Nittler LR., Zinner E., José J., Hernanz M. and Lewis RS. (2001a) Presolar grains from novae. Astrophysical Journal 551, 1065

Amari S., Nittler LR., Zinner E., Lodders K. and Lewis RS. (2001b) Presolar SiC grains of type A and B: Their isotopic compositions and stellar origins. Astrophysical Journal 551, 463

Amari S., Zinner E. and Gallino R. (2014) Presolar graphite from the Murchison meteorite: An isotopic study. Geochimica et Cosmochimica Acta 133, 479–522.

Amelin Y., Kaltenbach A., Iizuka T., Stirling C. H., Ireland T. R., Petaev M. and Jacobsen S. B. (2010) U-Pb chronology of the Solar System's oldest solids with variable 238U/235U.
Earth and Planetary Science Letters 300, 343-350.

Anders E. (1964). Origin, age and composition of meteorites. Space Science Review 3, 583–714.

Anders E. and Zinner E. (1993) Interstellar grains in primitive meteorites: diamond, silicon carbide, and graphite. Meteoritics 28, 490–514.

Arnould M and Goriely S. (2003) The p-process of stellar nucleosynthesis: Astrophysics and nuclear physics status. Physics Reports 384, 1-84

Arlandini C., Käppeler F., Wisshak K., Gallino R., Lugaro M., Busso M. and Straniero O. (1999) Neutron capture in low-mass asymptotic giant branch stars: cross sections and abundance signatures. Astrophysical Journal .525, 886–900.

Ávila J.N., Lugaro M., Ireland T.R., Gyngard F., Zinner E., Cristallo S., Holden P., Buntain J., Amari S. and Karakas A. (2012) Tungsten isotopic compositions in Stardust SiC grains from the Murchison meteorite: Constraints on the s-process in the Hf-Ta-W-Re-Os region. Astrophysical Journal 744, 49.

Ávila, J.N., Ireland, T.R., Gyngard, F., Zinner, E., Mallmann, G., Lugaro, M., Holden, P., Amari, S., 2013. Ba isotopic compositions in stardust SiC grains from the Murchi-son meteorite: insights into the stellar origins of large SiC grains. Geochmica et Cosmochmica Acta120, 628–647.

Bast R., Scherer E. E., Sprung P., Fischer-Gödde M., Stracke A. and K. Mezger (2015) A rapid and efficient ion-exchange chromatography for Lu-Hf, Sm-Nd, and Rb-Sr geochronology and the routine isotope analysis of sub-ng amounts of Hf by MC-ICP-MS. Journal of Analytical Atomic Spectrometry 30, 2323-2333.

Becker M, Hezel D., Schulz T., Elfers B-M. and Münker C. (2015) Formation timescales of CV chondrites from component specific Hf–W systematics. Earth and Planetary Science Letters 432, 472-482.

Berg T., Maul J., Schönhense G., Marositis E., Hoppe P., Ott U. and Plame H. (2009) Direct evidence for Condensation in the early solar system and implications for the nebular cooling rates. Astrophysical Journal 702, L172-L176

Berglund M. and Wieser M.E. (2011) Isotopic compositions of the elements 2009. Pure and Applied Chemistry 83, 397-410.

Bisterzo, S., Gallino, R., Staniero, O., Cristallo, S. and Käppeler, F. (2011) The s-process in lowmetallicity stars – II. Interpretation of high-resolution spectroscopic observations with asymptotic giant branch models. Monthly Notices of the Royal Astronomical Society 418, 284-319.

Bisterzo S., Travaglio C., Gallino R., Wiescher M. and Käppeler F. (2014) Galactic chemical evolution evolution and solar s-process abundances: Dependence on the 13C-pocket structure. The Astrophysical Journal 787, 10.

Bland P.A., Alard O., Benedix G.K., Kearsly A.T., Menzles O., Watt L.E., and Rodgers N.W. (Volatile fractionation in the early solar system and chondrule matrix complementarity. Proceedings of the National Science Academy 102, 13755-13760.

Blichert-Toft J. (2001) On the Lu-Hf isotope geochemistry of silicate rocks. Geostandards Newsletter 25, 41–56.

Boato G. (1954) The isotopic composition of hydrogen and carbon in the carbonaceous chondrites. Geochimica et Cosmochimica Acta 6, 209–220.

Bouvier A., Vervoort J.D. and Patchett P.J. (2008) The Lu–Hf and Sm–Nd isotopic composition of CHUR: Constraints from unequilibrated chondrites and implications for the bulk composition of terrestrial planets. Earth and Planetary Science Letters 273, 48–57.

Bouvier A. and Wadhwa M. (2010) The age of the Solar System redefined by the oldest Pb-Pb age of a meteoritic inclusion. Nature Geoscience 3, 637-641.

Brearley A. J. and Jones R. H. (1998) Chondritic meteorites. In Planetary Materials, J. Reviews in Mineralogy, vol. 36. Washington, D.C.: The Mineralogical Society of America. pp. 3-1–3-398

Breton T, Quitte G, Toplis M.J., Monnereau M., Birck J-L., Göpel C. and Charles C. (2015) Tafassassset: Evidence of early incipient differentiation on a metal-rich chondritic parent body.Earth and Planetary Science Letters 425, 193-203.

Burbidge E., Burbidge G., Fowler W. and Hoyle F. (1957) Synthesis of the elements in stars. Reviews of Modern Physics 29, 547–650.

Burkhardt C., Kleine T., Dauphas N. and Wieler R. (2012a) Origin of isotopic heterogeneity in the solar nebula by thermal processing and mixing of nebular dust. Earth and Planetary Science Letters 357-358, 298-307.

Burkhardt C., Kleine T., Dauphas N. and Wieler R. (2012b) Nucleosynthetic tungsten isotope anomalies in acid leachates of the Murchison chondrite: Implications for Hf-W chronometry. The Astrophysical Journal Letters 753, L6.

Burkhardt C. and Schönbächler M. (2015) Intrinsic W nucleosynthetic isotope variations in carbonaceous chondrites: Implications for W nucleosynthesis and nebular vs. parent body processing of presolar materials. Geochimica et Cosmochmica Acta 165, 361-375.

Burkhardt C., Borg L.E., Brennecka G., Shollenberger Q., Dauphas N. and Kleine T. (2016) A nucleosynthetic origin for the Earth's anomalous 142Nd composition. Nature 537, 394-398.

Cameron AGW (1957) Nuclear reactions in stars and nucleogenesis. Publications of the Astronomical Society of the Pacific, 201–222

Carlson R. W., Czamanske G., Fedorenko V. and Ilupin I. (2006) A comparison of Siberian meimechites and kimberlites: implications for the source of high-Mg alkalic magmas and flood basalts. Geochemistry, Geophysics and Geosystems 7.

Chen J. H., Papanastassiou D. A. and Wasserburg G. J. (2010) Ruthenium endemic isotope effects in chondrites and differentiated meteorites. Geochimica et Cosmochimica 74, 3851–3862.

Choi B.-G., McKeegan K.D., Leshin L.A. and Wasson, J.T. (1997) Origin of magnetite in oxidized CV chondrites: in situ measurement of oxygen isotope composi-tions of Allende magnetite and olivine. Earth and Planetary Science Letters 146, 337–349.

Choi, B.G., Wasserburg, G.J. and Huss, G.R. (1999) Circumstellar hibonite and corundum and nucleosynthesis in asymptotic giant branch stars. Astrophysical Journal 522, L133-L136.

Cohen, B.A., Hewins, R.H., Yu, Y., 2000. Evaporation in the young solar nebula as the origin of 'just-right' melting of chondrules. Nature 406, 600–602.

Conolly et al. (2006) The Meteoritical Bulletin, No. 90, 2006 September. Meteoritics and Planetary Science 41, 1383–1418.

Clayton R.N., Grossman L, and Mayeda T.K. (1973) A component of primitive nuclear composition in carbonaceous meteorites. Science 182, 485–488.

Clayton R. N. (1993) Oxygen isotopes in meteorites. Annual Review of Earth and Planetary Science Letters 21, 115–149.

Cronin J. R., Pizzarello S. and Cruikshank D. P. (1988) Organic matter in carbonaceous chondrites, planetary satellites, asteroids and comets. In Meteorites and the early solar system, 819–857. Tucson, University of Arizona Press.

Dai ZR, Bradley JP, Joswiak DJ, Brownlee DE, Hill HGM, Genge MJ (2002) Possible in situ formation of meteoritic nanodiamonds in the early Solar System. Nature 418:157–159

Davidson J., Busemann H., Franchi J.A. and Grady M.M. (2010) presolar grain inventories of the ungrouped C3 Adelaide and the CV 3 RBT 04133. Lunar and Planetary Science Conference XLI, #2230

Davidson, J., Busemann, H., Nittler, L.R., Alexander, C.M.O'D., Orthous-Daunay, F.-R., Franchi, I.A. and Hoppe, P. (2014) Abundances of presolar silicon carbide grains in primitive meteorites determined by NanoSIMS. Geochimica et Cosmochimica Acta 139, 248-266.

Davidson, J., Schrader, D. L., Alexander, C. M. O'D., Lauretta, D. S., Busemann, H., Franchi, I. A., Greenwood, R. C., Connolly, H. C., Domanik, K. J. and Verchovsky, A. (2015) Petrography, stable isotope compositions, microRaman spectroscopy and presolar components of Roberts Massif 04133: a reduced CV3 carbonaceous chondrite. Meteoritics and Planetary Science 49, 2133–2151.

Dauphas N., Marty B. and Reisberg L. (2002) Molybdenum nucleosynthetic dichotomy revealed in primitive meteorites. Astrophysical Journal 569, 139-142.

Dauphas N. and Schauble E.A. (2016) Mass Fractionation Laws, Mass-Independent effects and Isotopic anomalies. Annual Review of Earth and Planetary Science 44, 709-783.

Davidson, J., Busemann, H., Nittler, L.R., Alexander, C.M.O'D., Orthous-Daunay, F.-R., Franchi, I.A. and Hoppe, P. (2014) Abundances of presolar silicon carbide grains in primitive meteorites determined by NanoSIMS. Geochimica et Cosmochimica Acta 139, 248-266.

Deer W.A., Howie R.A. and Zussman J. (1992) An introduction to the Rock-forming minerals. Pearson Prentice Hall, Harlow.

Demyk K., Carrez Ph., Leroux H., Cordier P., Jones A. P., Borg J., Quirico,E., Raynal P. I. and d'Hendecourt, L. (2001) Structural and chemical alteration of crystalline olivine under low energy He+ irradiation. Astronomy and Astrophysics 368, L38–L41

Depaolo D.J. and Wasserburg G.J. (1979) Petrogenic mixing models and Nd-Sr isotopic patterns. Geochmica et Cosmochimica Acta 43, 615-627.

Du Fresne E.R. and Anders E. (1962) On the chemical evolution of the carbonaceous chondrites. Geochimica et Cosmochimica Acta 26, 1085–1114.

Ebel D.S. and Grossman L. Condensation in dust-enriched systems (2000). Geochimica et Cosmochimica 64, 339– 366.

Eugster O., Tera F., Burnett D.S. and Wasserburg, G.J. (1970) The isotopic composition of Gd and the neutron capture effects in samples from Apollo 11. Earth and Planetary Science Letters 8, 20–30.

Eugster O. (2003) Cosmic-ray exposure ages of meteorites and lunar rocks and their significance. Chemie der Erde 63, 3-30.

Fehr M. A., Rehkämper M., Halliday A. N., Schönbächler M., Hattendorf B. and Günther D. (2006) Search for nucleosynthetic and radiogenic tellurium isotope anomalies in carbonaceous chondrites. Geochmica et Cosmochimica Acta 70, 3436–3448.

Floss C. and Stadermann F.J. (2012) Presolar silicate and oxide abundances and compositions in the ungrouped carbonaceous chondrite Adelaide and the K chondrite Kakangari: The effects of secondary processing. Meteoritics and Planetary Science 47, 992-1009.

Fuchs L.H., Olsen E. and Jensen K.J. (1973) Mineralogy, Mineral-Chemistry, and Composition of the Murchison (C2) Meteorite. Smithsonian Contribution to the Earth Sciences 10, 1-39.

Funk C., Wombacher F., Tabersky D., Frick D. A., Meisel T., Kronz A., Heuser A., Scheld J. and Günther D. (in revision) Composition and homogeneity of CANS - a chondrite analogue nanoparticle calibration standard for LA-ICP-MS. Geostandards and Geoanalytical Research.

Gail H-.P. (2004) Radial mixing in protoplanetary accretion disks. IV. Metamorphosis of the silicate dust complex. Astronomy and Astrophysics 413, 571-591.

Gail, H.-P., Zhukovska, S. V., Hoppe, P. and Trieloff, M. (2009) Stardust from asymptotic giant branch stars. Astrophysical Journal 698, 1136–1154.

Grossman J. N. and Brearley A. J. 2005. The onset of metamorphism in ordinary and carbonaceous chondrites. Meteoritics and Planetary Science 40, 87–122.

Harker D.E. and Desch S.J. (2002) Annealing of silicate dust by shocks at 10 AU. Astrophysical Journal Letters 565, L109—L112.

Hawking S.W. (1988) A brief history of time. New York, Bantam Books.

Herzog G. F. (2003) Cosmic-Ray Exposure Ages of Meteorites. Treatise on Geochemistry Volume 1, p.347-380.

Hezel D.C., Russell S.S., Ross A.J. and Kearsley A. T. (2008) Modal abundances of CAIs: implications for bulk chondritic element abundances and fractionations. Meteoritics and Planetary Science 43, 1879–1894.

Hidaka H., Ohta Y. and Yoneda, S. (2003) Nucleosynthetic components of the early solar system inferred from Ba isotopic compositions in carbonaceous chondrites. Earth and Planetary Science Letters 214, 455-466.

Hidaka H., Ebihara M. and Yoneda S. (2000) Isotopic study of neutron capture effects on Sm and Gd in chondrites. Earth and Planetary Science Letters 180, 29–37.

Holst J., Paton C, Wielandt D. and Bizzarro M (2015) Tungsten isotopes in bulk meteorites and their inclusions—Implications for processing of presolar components in the solar protoplanetary disk. Meteoritics and Planetary Science Volume 50 Issue 9, 1643-1660.

Hoppe P., Amari S., Zinner E., Ireland T. and Lewis RS (1994) Carbon, nitrogen, magnesium, silicon, and titanium isotopic compositions of single interstellar silicon carbide grains from the Murchison carbonaceous chondrite. Astrophysical Journal 430, 870–890.

Hoppe P. and Ott U. (1997) Mainstream silicon carbide grains from meteorites. In Astrophysical Implications of the Laboratory Study of Presolar Materials. New York, pp. 27–58.

Hoppe P., Strebel R., Eberhardt P., Amari S. and Lewis, R.S. (2000) Isotopic properties of silicon carbide X grains from the Murchison meteorite in the size range 0.5-1.5μm. Meteoritics and Planetary Science 35, 1157-1176.

Hoppe P. and Zinner E. (2012) Sulfur-isotopic signature of presolar SiC grains of type X. Lunar and Planetary Science 43: #1414.

Hoyle F. (1946) The synthesis of the elements from hydrogen. Monthly Notices of the Royal Astronomical Society 106, 343.

Hoyle F. (1954) On Nuclear Reactions Occuring in Very Hot STARS. I. the Synthesis of Elements from Carbon to Nickel. The Astrophysical Journal Supplement Series 1, 121.

Huss G. R., Fahey A. J., Gallino R. and Wasserburg G. J. (1994) Oxygen isotopes in circumstellar Al2O3 grains from meteorites and stellar nucleosynthesis. Astrophysical Journal 430, L81–L84.

Huss G. R. and Lewis R. S. (1995) Presolar diamond, SiC, and graphite in primitive chondrites: abundances as a function of meteorite class and petrologic type. Geochimica et Cosmochimica Acta 59, 115–160.

Huss G. R. (1997) The survival of presolar grains in solar system bodies. In Astrophysical Implications of the Laboratory Study of Presolar Materials AIP, New York.

Huss G.R., Meshik A.P., Smith J.B. and Hohenberg C.M. (2003) Presolar diamond, silicon carbide, and graphite in carbonaceous chondrites: implications for thermal processing in the solar nebula. Geochimica et Cosmochimica Acta 67, 4823-4848.

Huss G.R. (2004) Implications of isotopic anomalies and presolar grains for the formation of the solar system. Antarctic Meteorite Research 17, 132.

Huss G.R., Rubin A.E. and Grossman J.N. (2006) Thermal metamorphism in chondrites. In Meteorites and the solar system II. Tuscon, University of Arizona press.

Hynes K, Gyngard F*(*2009*)* The Presolar Grain Database: http://presolar.wustl.edu/~pgd. Lunar and Planetary Science Conference 40*,* 1198

Imae N. and Kojima H. (2000) On the relationship between troilite and/or magnetite rimmed FeNi metals and subtype in CO3 chondrites. Antarctic Meteorite Research 13, 65-77.

Keller L.P. and Buseck P.R. (1990) Matrix mineralogy of the Lancé CO3 carbonaceous chondrite: A transmission electron microscope study. Geochmica et Cosmochimica Acta 54, 155-1163.

Kemper F., Vriend W.J., Tielens A.G.G.M. (2004) The absence of crystalline silicates in the diffuse insterstellar Medium. Astrophysical Journal 609, 826-837.

Kleine T., Münker C., Mezger K. and Palme H. (2002) Rapid accretion and early core formation on asteroids and the terrestrial planets from Hf-W chronometry. Nature 418, 952–955.

Kleine T., Mezger K., Münker C., Palme H. and Bischoff A. (2004) 182Hf-182W isotope systematics of chondrites, eucrites, and martian meteorites: Chronology of core formation and early mantle differentiation in Vesta and Mars. Geochimica et Cosmochimica Acta 68, 2835-2946

Kleine T., Touboul M., Halliday A., Zipfel J. and Palme H. (2007) Cosmochemical fractionation of Hf and W in the solar nebula: evidence from W isotopes in chondrites. Lunar Planetary Science Conference XXXVIII.

Krot, A.N., Scott, E.R.D. and Zolensky, M.E. (1995) Mineralogical and chemical modi-fication of components in CV3 chondrites: nebular or asteroidal processingMeteoritics and Plantary Science 30, 748–775.

Krot A.N. and Hutcheon I. (2006) Timescales and settings for alteration of chondritic materials. In: Meteorites and the early solar system II, 525-553.

Krot A. N., Amelin Y., Bland P., Ciesla F. J., Connelly J. N., Davis A. M., Huss G. R., Hutcheon I. D., Makide K., Nagashima K., Nyquist L. E., Russell S. S., Scott E. R. D., Thrane K., Yurimoto H., and Yin Q.-Z. (2009) Origin and chronology of chondritic components: A review. Geochimica et Cosmochimica Acta 73, 4963–4997.

Krot A.N., Keil K., Goodrich C. A., Scott E. R. D., and Weisberg M.K. (2013) Classification of meteorites. In Meteorites, comets, and planets, Treatise on geochemistry, vol. 2, 83–128. Amsterdam, Elsevier

Kruijer T, Fischer-Gödde M., Kleine T., Sprung P., Leya I. and Wieler R. (2013) Neutron capture on Pt isotopes in iron meteorites and the Hf–W chronology of core formation in planetesimals. Earth and Planetary Science Letters 361, 162-172.

Kruijer T., Kleine T., Fischer-Gödde M., Burkhardt C. and Wieler R. (2014) Nucleosynthetic W isotope anomalies and the Hf–W chronometry of Ca–Al-rich inclusions. Earth and Planetary Science Letters 403, 317–327

Kruijer T., Kleine T., Fischer-Gödde M. and Sprung P. (2015) Lunar tungsten isotopic evidence for the late veneer. Nature 520, 534-537

Lattimer J.M., Mackie F., Ravenhall D.G. and Schramm D.N. (1977) The decompression of cold neutron star matter. The Astrophysical Journal 213, 225–233.

Lambert DL., Gustafsson B., Eriksson K., Hinkle KH. (1986) The chemical composition of carbon stars. I-Carbon, nitrogen, and oxygen in 30 cool carbon stars in the Galactic disk. Astrophysical Journal 62, 373–425

Leitner, J., Metzler, K., Vollmer, C. and Hoppe, P. (2013) Search for presolar grains in fine-grained rims: first results from CM chondrites and Acfer 094. Lunar Planetary Science Conference XLIV, 2273.

Leitner J., Vollmer C., Floss C., Zipfel J. and Hoppe P. (2016) Ancient Stardust in fine-grained chondrule dust rims from carbonaceous chondrite. Earth and Planetary Science Letters 436, 117-128.

Lewis R.S., Ming T., Wacker J.F., Anders E. and Steel E. (1987) Interstellar diamonds in meteorites. Nature 326, 160-162.

Leya I., Schönbächler M., Wiechart U., Krahenbuhl U. and Halliday A. N. (2008) Titanium isotopes and the radial heterogeneity of the solar system. Earth and Planetary Science Letters 266, 233–244.

Leya I., Schönbächler M., Krahenbuhl U. and Halliday A. N. (2009) New titanium isotope data for Allende and Efremovka CAIs. Astrophysical Journal 702, 1118–1126.

Lodders, K., Fegley, B., 1995. The origin of circumstellar silicon carbide grains found in meteorites. Meteoritics 30, 661-678

Lodders, K., Fegley, B., 1999. Condensation chemistry of circumstellar grains. In: Asymptotic Giant Branch Stars. Astronomical Society of the Pacific, 279-289.

Lodders K. (2003) Solar system abundances and condensation temperatures of the elements. Astrophysical Journal 591, 1220–1247.

Lugmair G.W. and Marti K. (1971) Neutron capture effects in lunar Gadolinium and the irradiation histories of some lunar rocks. Earth and Planetary Science Letters 13, 32–42.

MacPherson GJ, Wark DA, and Armstrong JT (1988) Primitive material surviving in chondrites: Refractory inclusions. Meteorites and the Early Solar System, pp. 746–807. Tucson: University of Arizona Press.

Mc Culloch M.T. and Wasserburg G.J. (1978) More Anomalies from the Allende meteorite: Samarium. Geophysical Research Letters Vol 5 No 7, 599-602.

McSween H. Y. (1977b) Carbonaceous chondrites of the Ornans type: A metamorphic sequence. Geochimica et Cosmochimica Acta 41**,** 477–491.

McSween H. Y., Jr. (1977a) Petrographic variations among carbonaceous chondrites of the Vigarano type. Geochimica et Cosmochimica Acta 41, 1777–1790.

McSween H. Y.. (1979) Alteration in CM carbonaceous chondrites inferred from modal and chemical variations in matrix. Geochimica et Cosmochimica Acta 43**,** 1761–1770.

Mendybaev R.A., Beckett J.R., Grossman L., Stolper E., Cooper R.F. and Bradley J.P. (2002) Volatilization kinetics of silicon carbide in reducing gases: An experimental study with applications to the survival of presolar grains in the solar nebula. Geochimica et Cosmochimica Acta, Vol. 66, 661–682.

Merrill P.W. (1952) Spectroscopic Observations of Stars of Class. Astrophysical Journal 116, 21.

Messenger S., Keller L. P., Stadermann F. J., Walker R. M. and Zinner E. (2003) Samples of stars beyond the solar system: silicate grains in interplanetary dust. Science 300, 105–108.

Messenger S., Keller L. P. and Lauretta D. S. (2005) Supernova olivine from cometary dust. Science 309, 737–741.

Mostefaoui S. and Hoppe P. (2004) Discovery of abundant in situ silicate and spinel grains from red giant stars in a primitive meteorite. Astrophysical Journal 613, L149–L152.

Münker C., Weyer S., Scherer E. and Mezger K. (2001) Separation of high field strength elements (Nb, Ta, Zr, Hf) and Lu from rock samples for MC-ICPMS measurements. Geochemistry, Geophysics, Geosystems 2, 2001GC000183.

Münker C, Weyer S., Mezger K., Rehkämper M., Wombacher F and Bischoff A. (2000). 92Nb-92Zr and the early differentiation history of planetary bodies. Science 289, 1538-1542.

Nagashima K., Krot A. N. and Yurimoto H. (2004) Stardust silicates from primitive meteorites. Nature 428 , 921–924

Nagashima, K., Sakamoto, N. and Yurimoto, H. (2005) Destruction of presolar silicates by aqueous alteration observed in Murchison CM2 chondrite. Lunar and Planetary Science Conference XXXVI, #1671.

Nguyen A., Zinner E., Lewis R.S. (2003) Identification of small presolar spinel and corundum grains by isotopic raster imaging. Publications of the Astronomical Society Australia 20, 382-389.

Nguyen, A. N. and Zinner, E. (2004) Discovery of ancient silicate stardust in a meteorite. Science 303, 1496–1499.

Nguyen AN. and Messenger S. (2011) Presolar history recorded in extraterrestrial materials. Elements 7, 17–22

Nguyen, A. N. and Messenger, S. (2014) Resolving the stellar sources of isotopically rare presolar silicate grains through Mg and Fe isotopic analyses. Astrophysical Journal 784, 149

Nicolussi G. K., Davis A. M., Pellin M. J., Lewis R. S., Clayton R.N. and Amari S. (1997) S-process Zirconium in presolar silicon carbide grains. Science 277, 1281–1283.

Nicolussi GK., Pellin MJ., Lewis RS., Davis AM., Clayton RN. and Amari S. (1998) Zirconium and molybdenum in individual circumstellar graphite grains: New isotopic data on the nucleosynthesis of heavy elements. Astrophysical journal 504, 492–498.

Nielsen R.L, Forsythe L.M, Gallahan W.E, Fisk M.R. (1994) Major-element and trace-element magnetite-melt equilibria. Chemical Geology 117, 167–191.

Nittler L.R. and Alexander, C.M.O'D. (1999) Automatic identification of presolar Al- and Ti-rich oxide grains from ordinary chondrites. Lunar and Planetary Science Conference 30, #2041

Nittler L. R. (2003) Presolar stardust in meteorites: recent advances and scientific frontiers. Earth and Planetary Science Letters 209, 259–273.

Nittler LR. and Alexander CMO'D (2003) Automated isotopic measurements of micron-sized dust: Application to meteoritic presolar silicon carbide. Geochimica et Cosmochimica Acta 67, 4961–4980.

Nittler L.R. (2005) Constraints on heterogeneous galactic chemical evolution from meteoritic stardust. The Astrophysical Journal 618, 281–296.

Nittler L. R., Alexander C. M. O'D., Gallino R., Hoppe P., Nguyen A. N., Stadermann F. J. and Zinner E. K. (2008) Aluminum-, calcium- and titanium-rich oxide stardust in ordinary chondrite meteorites. Astrophysical Journal 682, 1450– 1478.

Nittler L. R., Alexander C. M. O'D. and Stroud R. M. (2013) High abundance of presolar materials in CO3 chondrite Dominion Range 08006 Lunar and Planetary Science Conference. XLIV, #2367.

Norton O. R. 2002. The Cambridge encyclopedia of meteorites. Cambridge, Cambridge University Press.

Ott, U. 1993. Interstellar grains in meteorites. Nature 364, 25-33.

Onuma N., Nishida N., Okudera S and Ona Y. (1976) Chemical inhomogeneity in a single euhedral olivine from the Murchison C2 chondrite. Geochemical Journal 10, 209-210

Ott, U. 1993. Interstellar grains in meteorites. Nature 364, 25-33.

Patchett P. J. and Tatsumoto M. (1980) A routine high-precision method for Lu–Hf isotope geochemistry and chronology. Contributions to Mineralogy and Petrology 75, 263–267.

Pellin M., Savina M., Calaway W., Tripa C., Barzyk J., Davis A., Gyngard F., Amari S., Zinner E. and Lewis R. (2006) Heavy metal isotopic anomalies in supernovae presolar grains. Lunar and Planetary Science Conference 37, 2041

Peters S. T. M., Münker C., Becker H. and Schulz T. (2014) Alphadecay of 184Os revealed by radiogenic 180W in meteorites: Half-life determination and viability as geochronometer. Earth and Planetary Science Letters 391, 69–76.

Peters S.T.M., Münker C., Wombacher F. and Elfers, B-M. (2015) Precise determination of low abundance isotopes (174Hf, 180W and 190Pt) in terrestrial materials and meteorites using multiple collector ICP-MS equipped with 1012Ω Faraday amplifiers. Chemical Geology 413, 132-145.

Peters S:T.M. Münker C., Pfeifer M., Elfers B.M. and Sprung P. (2016) Distribution of p-process 174Hf in early solar system materials and the origin of nucleosynthetic Hf and W isotope anomalies in Ca-Al rich inclusions. Earth and Planetary Science Letters.

Pfalzner S., Davies M.B., Gounelle M., Johansen A., Münker C., Lacerda P., Portegies Zwart S., Testi L., Trieloff M., and Veras D. (2015) The formation oft he solar system. Royal Swedisch Academy of Sciences 90, 068001.

Potts P.J. (1992) A handbook of silicate rock analysis. Blackie & Son, London.

Podosek F. A., Ott U., Brannon J. C., Neal C. R., Bernatowicz T. J., Swan P. and Mahan S. E. (1997) Thoroughly anomalous chromium in Orgueil. Meteoritics and Planetary Science, 32, 617–627.

Qin L., Carlson R.W. and Alexander C.M.O.D. (2011) Correlated nucleosynthetic isotopic variability in Cr, Sr, Ba, Sm, Nd and Hf in Murchison and QUE 97008. Geochimica et Cosmochimica Acta 75, 7806-7828.

Qin, L., Dauphas, N., Wadhwa, M., Markowski, A., Gallino, R., Janney, P.E. and Bouman, C. (2008) Tungsten nuclear anomalies in planetesimal cores. Astrophysical Journal 674, 1234- 1241.

Ranen M. C. and Jacobsen S. B. (2006) Barium isotopes in chondritic meteorites: implications for planetary reservoir models. Science 314, 809–812.

Rauscher T., Dauphas N., Dillmann I., Fröhlich I., Fülöp Z. and Gyürky G. (2013) Constraining the astrophysical origin of the p-nuclei through nuclear physics and meteoritic data. Reports on Progress in Physics 76, 066201 (38pp).

Regelous M., Elliott T. and Coath C. D. (2008) Nickel isotope heterogeneity in the early solar system. Earth and Planetary Science Letters 272, 330–338.

Reisberg L., Dauphas N., Luguet A., Pearson D.G., Gallino R. and Zimmermann C. (2009) Nucleosynthetic osmium isotope anomalies in acid leachates of the Murchison meteorite. Earth and Planetary Science Letters 277, 334-344.

Riebe M. (2009) spinel group minerals in carbonaceous and ordinary chondrites. Unpublished Bachelor thesis. http://lup.lub.lu.se/luur/download?func=downloadFile&recordOId=2301994&fileOId=2301995

Rosswog S., Liebendörfer M., Thielemann F.-K., Davies M.B., Benz W. and Piran T. (1999) Mass ejection in neutron star mergers. Astronomy and Astrophysics 341, 499–526.

Rotaru M., Birck J. L. and Allegre C. J. (1992) Clues to early solar system history from chromium isotopes in carbonaceous chondrites. Nature 358, 465–470.

Rubin A.E., Trigo-Rodriguez J.M., Huber H. and Wasson J.T. (2007) Progressive aqueous alteration of CM carbonaceous chondrites. Geochimica et Cosmochmica Acta 71, 2361–2382.

Russ III, G.P., Burnett, D.S., Lingenfelter, R.E. and Wasserburg, G.J. (1971) Neutron capture on 149Sm in lunar samples. Earth and Planetary Science Letters 13, 53–60.

Russ III, G.P., Burnett, D.S., Lingenfelter, R.E. and Wasserburg, G.J. (1971) Neutron capture on 149Sm in lunar samples. Earth and Planetary Science Letters 13, 53–60.

Russell W. A., Papanastassiou D. A. and Tombrello T. A. (1978) Ca isotope fractionation on the Earth and other solar system materials. Geochimica et Cosmochimica Acta 42, 1075–1090.

Savina, M. R., Pellin, M. J., Tripa, C. E., Davis, A. M., Lewis, R. S. and Amari, S. (2004). Excess p-process molybdenum and ruthenium in a presolar Sic grain. Nuclei in the Cosmos VIII, Abstract 160.

Schönbächler M., Rehkämper M., Lee D.-C. and Halliday A. N. (2004) Ion exchange chromatography and high precision isotopic measurements of zirconium by MC–ICPMS. Analyst 129, 32–37.

Schönbächler M., Rehkämper M., Fehr M.A., Halliday A.N., Hattendorf B. and Günther D. (2005) Nucleosynthetic zirconium isotope anomalies in acid leachates of carbonaceous chondrites. Geochimica et Cosmochimica Acta 69, 5113-5122.

Scott R.R.D., Jones R.H. and Rubin A.E. (1994) Classicfication, metamorphic history, and pre-metamorphic composition of chondrules. Geochmica et Cosmochimica Acta 58, 1203-1209.

Scott E. R. D. and Krot A. N. (2006) Chondritic meteorites and the high-temperature nebular origins of their components. In: Chondrites and the Protoplanetary Disk. ASP Conference Series, Vol. 341, San Francisco: Astronomical Society of the Pacific.

Scott E.R.D. and Krot A.N. (2013) Chondrites and their components. In Meteorites, comets, and planets, ed. A. M. Davis, Treatise on geochemistry, vol. 2, 143–200. Amsterdam, Elsevier

Schulz T. Münker C., Peters S. T. M. (2013) P-process 180W anomalies in iron meteorites: nucleosynthetic versus non-nucleosynthetic origins. Earth and Planetary Science Letters 362, 246-257.

Sears D.W.G., Grossman J.N., Melcher C.L., Ross L.M., and Mills A.A. (1980) Measuring the metamorphic history of unequilibrated ordinary chondrites. Nature 287, 791-795.

Sears, D. W. G., and R. T. Dodd. (1988) Overview and classification of meteorites. In Meteorites and the early solar system, 3–31. Tucson, University of Arizona Press.

Seife C. (2003) Breakthrough of the Year: Illuminating the Dark Universe. Science 302, 2038–2039.

Simon S. B., Grossman L., Podosek F. A., Zinner E. and Prombo C. A. (1994) Petrography, composition, and origin of large, chromian spinels from the Murchison meteorite. Geochmica et Cosmochimica Acta 58, 1313–1334.

Simon J. I., DePaolo D. J. and Moynier F. (2009) Calcium isotope composition of meteorites, Earth and Mars. Astrophysical Journal. 702, 707–715.

Speck A., Barlow M., Skinner C. (1997) The nature of the silicon carbide in carbon star outflows. Monthly notices of the Royal Astronomical Society 288, 431–456.

Sprung P., Scherer E. E., Upadhyay D., Leya I. and Mezger K. (2010) Non-nucleosynthetic heterogeneity in non-radiogenic stable Hf isotopes: Implications for early solar system chronology. Earth and Planetary Science Letters 295, 1–11.

Stroud RM, Chisholm MF, Heck PR, Alexander CMO'D, Nittler LR (2011) Supernova shock-wave-induced co-formation of glassy carbon and nanodiamond. Astrophysical Journal 738, L27.

Trinquier A., Birck J.-L. and Allegre C. J. (2007) Widespread 54Cr heterogeneity in the inner solar system. Astrophysical Journal 655, 1179– 1185.

Trinquier A., Elliott T., Ulfbeck D., Coath C., Krot A.N. and Bizzarro M. (2009) Origin of nucleosynthetic isotope heterogeneity in the solar protoplanetary disk. Science 324, 374–376.

Van Schmus W.R. and Wood J.A. (1967) A chemical-petrologic classification for the chondritic meteorites. Geochimica et Cosmochimica Acta 31, 747–765.

Vervoort J.D. and Blichert-Toft J. (1999) Evolution of the depleted mantle: Hf isotope evidence from juvenile rocks through time. Geochimica et Cosmochimica Acta 63, 533-556.

Vollmer, C., Hoppe, P., Stadermann, F.J., Floss, C., Brenker, F., 2009a. NanoSIMS analysis and Auger electron spectroscopy of silicate and oxide stardust from the carbonaceous chondrite Acfer 094. Geochimica et Cosmochimica Acta 73, 7127–7149.

Völkening J., Köppe M. and Heumann K. (1991) Tungsten isotope ratio determination by negative thermal ionization mass spectrometry. International Journal of Mass Spectrometry and Ion processes 107, 361-368.

Walker R. (2012) Evidence for homogeneous distribution of osmium in the protosolar nebula. Earth and Planetary Science Letters 351–352, 36–44

Wallerstein G., Iben I.J., Parker P., Boesgaard AM., Hale G.M., Champagne A.E., Barnes C.A., Käppeler F., Smith V.V., Hoffman R.D., Timmes F.X., Sneden C., Boyd R.N., Meyer B.S. and Lambert D.L. (1997) Synthesis of the elements in stars: Forty years of progress. Reviews of Modern Physics 69, 995–1084.

Waters et al. (1996) Mineralogy of oxygen-rich dust shells. Astronomy and Astrophysics 315, L361–L364

Weinberg S. (1993) The first three minutes. New York, Basic Books.

Weisberg M.K., McCoy T.J. and Krot A.N. (2006) Systematics and evaluation of meteorite classification. In Meteorites and the early solar system II. Tuscon, University of Arizona press

Wijbrans C.H., Klemme S., Berndt J. and Vollmer C. (2016) Experimental determination of trace element partition coefficients between spinel and silicate melt: the influence of chemical composition and oxygen fugacity. Contributins to Mineralolgy and Petrololgy169: 45.

Willbold M.. Elliott T. and Moorbath S. (2011) The tungsten isotopic composition of the Earth's mantle before the terminal bombardment. Nature 477, 195-199.

Wisshak K. Voss F., Käppeler F., Kazakov L., Becvar F., Krticka M., Galino R. and Pignatari M. (2006) Fast neutron capture on the Hf isotopes: Cross sections, isomer production, and stellar aspects. Physical Review C, 73(4): 045807.

Yokoyama T., Makashima A. and Nakamure E. (1999) Evaluation of the coprecipitation of incompatible trace elements with fluoride during silicate rock dissolution by acid digestion. Chemical Geology 157, 175-187.

Yokoyama T., Rai V. K., Alexander C. M. O., Lewis R. S., Carlson R. W., Shirey S. B., Thiemens M. H. and Walker R. J. (2007) Osmium isotope evidence for uniform distribution of s- and r-process components in the early solar system. Earth and Planetary Science Letters 259, 567–580.

Yokoyama T., Alexander C.M.O. and Walker, R.J. (2010) Osmium isotope anomalies in chondrites: Results for acid residues and related leachates. Earth and Planetary Science Letters 291, 48–59.

Yokoyama T., Alexander C.M.O. and Walker, R.J. (2011) Assessment of nebular versus parent body processes on presolar components present in chondrites: Evidence from osmium isotopes. Earth and Planetary Science Letters 305, 115-123.

Zega T.J., Nittler L., Gyngard F., Alexander C.M.O.D., Stroud R.M. and Zinner E. (2014) A transmission electron microscopy study of presolar spinel. Geochimica et Cosmochimica Acta 124, 152-169.

Zinner E., Ming T. and Anders E. (1989) Interstellar SiC in the Murchison and Murray meteorites: isotopic composition of Ne, Xe, Si, C, and N. Geochimica et Cosmochimica Acta 53, 3273–3290

Zinner E. (1998) Stellar nucleosynthesis and the isotopic composition of presolar grains from primitive meteorites. Annual Review of Earth and Planetary Science 26, 147–188.

Zinner E., Amari S., Guinness R., Nguyen A., Stadermann F., Walker R.M. and Lewis, R.S. (2003) Presolar spinel grains from the Murray and Murchison carbonaceous chondrites. Geochimica and Cosmochmica Acta 67, 5083-5095.

Zinner E (2014) Presolar grains. In: Meteorites and Cosmochemical Processes. Vol 1. Amsterdam. Elsevier

VI. Acknowledgements

Where to begin with?
I think it is a good start to thank the people who made all this possible.
So first I give many thanks to my doctor father Carsten. Thanks for supporting me and giving me the chance to fulfill one of my biggest dreams, to become a scientist. It is and it was a great pleasure to be part of your workgroup and you showed me that it is indeed possible to be a good scientist and a nice person at once. I am looking forward to continue working together in the future.

Many thanks also to Dominik for taking the time and reviewing my thesis.

I also want to address special thanks to Peter for countless discussions and brainstorming sessions about the data and the big story behind everything. I think it's now more than six years that we know each other and I really want to say thank you for supporting me and becoming a friend. Danke Peter ☺.

Strong appreciation furthermore goes to out to those that have contributed scientifically to this thesis, particularly Frank Wombacher, Nils Messling, Markus Pfeifer and Stefan Peters. You all helped to make all this possible.

Special are also addressed to my earlier officemates Maria and Lisa. Thanks for scientific discussions and countless funny moments.

I also would like to thank Addi Bischoff (Unversity of Muenster), Jutta Zipfel (Senckenberg Museum Frankfurt) and Erik Srub (University of Cologne) for kindly providing us meteorite samples.

Zum Schluss auch noch ein paar Worte auf Deutsch:
Ich danke natürlich auch meiner Familie. Ich danke euch vor allem für die Unterstützung die ihr mir habt zukommen lassen. Ihr wart immer da wenn mal irgendwas war. Danke dafür.

Besonderen möchte natürlich auch an meine besten Freunde Aaron, Alex und Anna richten. Auch euch vielen Dank für die Unterstützung und die schönen Zeiten die wir erlebt haben und die auch manchmal nötig waren um den Kopf wieder freizubekommen.

Coming back to English:
I would like to end this thesis with leaving a final note to the many people which a have met in Cologne and Bonn: Thank you for making me feel home ☺.

VII. Erklärung

Ich versichere, dass ich die von mir vorgelegte Dissertation selbständig angefertigt, die benutzten Quellen und Hilfsmittel vollständig angegeben und die Stellen der Arbeit − einschließlich Tabellen, Karten und Abbildungen − , die anderen Werken im Wortlaut oder dem Sinn nach entnommen sind, in jedem Einzelfall als Entlehnung kenntlich gemacht habe; dass diese Dissertation noch keiner anderen Fakultät oder Universität zur Prüfung vorgelegen hat; dass sie − abgesehen von unten angegebenen Teilpublikationen − noch nicht veröffentlicht worden ist, sowie, dass ich eine solche Veröffentlichung vor Abschluss des Promotionsverfahrens nicht vornehmen werde. Die Bestimmungen der Promotionsordnung sind mir bekannt. Die von mir vorgelegte Dissertation ist von Prof. Dr. Carsten Münker betreut worden.

Nachfolgend genannte Teilpublikationen liegen vor:

Elfers B-M., Sprung P., Pfeifer M., Wombacher F., Peters S.T.M. and Münker C. S –process variability in early solar system materials – evidence from ^{174}Hf and ^{180}W in sequentially leached primitive chondrites. Geochimica et Cosmochimica Acta (in review)

Datum Unterschrift